# Buoyant point-source scalar plumes in a turbulent boundary layer

MIAOYAN PANG

Doctor of Philosophy (Eng)

Supervisor: Dr Kapil Chauhan
Associate Supervisor: Dr Talluru Murali Krishna

A thesis submitted in fulfilment of
the requirements for the degree of
Doctor of Philosophy

School of Civil Engineering
Faculty of Engineering
The University of Sydney
Australia

5 December 2023

## Statement of originality

This is to certify that, to the best of my knowledge, the content of this thesis is my own work. This thesis has not been submitted for any other degree or purpose.

I certify that the intellectual content of this thesis is the product of my work and that all the assistance received in preparing this thesis and sources have been acknowledged.

Miaoyan PANG

30 Jun 2023

# Abstract

This thesis investigates the dispersion of buoyant plumes in a turbulent boundary layer. While previous studies have primarily focused on heavy or light plumes individually, a systematic comparison of heavy, neutral, and light plumes has not been conducted to the author's knowledge. To address this research gap, a novel experimental setup is developed to release gases of varying densities in a boundary layer wind tunnel, utilising iso-butylene as a tracer. By changing the density of tracer gas systematically, it is possible to investigate the dispersion of neutral, light and heavy plumes. Further, the wind tunnel floor is altered to understand the effect of surface roughness on the development of plumes in a turbulent boundary layer. The roughnesses tested in this study are configured to emulate a flow in an urban setting. Downstream of the point source, the streamwise and vertical velocity components are measured using an $\times$-wire anemometer, while the concentration of the tracer gas is measured using a Photo-Ionisation Detector. The acquired high-fidelity data are analysed to investigate the differences in the mean development of plumes with different densities compared to the ambient. It is observed that the mean plumes of heavy and light gases can be described by a Gaussian model, akin to those observed in a neutral plume. The wall-normal spread of heavy plumes is smaller, whereas the light plumes are wider. The behaviour of higher-order central moments (up to the $6^{\text{th}}$ moment) is found to possess Gaussian characteristics. It is determined that a single parametric distribution cannot adequately describe the probability density functions of instantaneous concentration within the plume. However, the high-concentration tail follows an exponential distribution, and the exponent exhibits a power-law relationship with plume width. An engineering model for vertical scalar fluxes is proposed here that describes the scaling of these fluxes, offering an alternative to the common gradient-diffusion model. The spread of plumes in a rough wall boundary layer is also investigated. The impact on plume characteristics by density is also observed in the rough-wall case, although the differences are less pronounced compared to the smooth-wall case. In the outer region of the roughness, the plume profile can be described using a truncated-Gaussian model. In contrast, no universal equation describes the mean concentration profile within the roughness canopy.

# List of publications

**Journal articles and conference papers:**

(1) Pang, M., & Chauhan, K. (2022). Probabilities of high-concentration events in scalar point-source plume in a turbulent boundary layer. *12th International Symposium on Turbulence and Shear Flow Phenomena*.

(2) Pang, M., & Chauhan, K. (2022). Measurements of scalar in buoyant plumes in a turbulent boundary layer. *Australasian Fluid Mechanics Conference 2022*. (Best Student presentation award at AFMC 2022)

(3) Pang, M., & Chauhan, K., & Talluru, K. M. (2023). Measurements of buoyant plumes in a turbulent boundary Layer. *Experiments in Fluid Mechanics*. (*in preparation*)

(4) Pang, M., & Chauhan, K., & Talluru, K. M. (2023). Vertical scalar fluxes of buoyant plumes in a turbulent boundary layer. *Journal of Fluid Mechanics*. (*in preparation*)

**Conference presentation:**

(1) Pang, M., & Chauhan, K. (2022). Buoyant plumes in a turbulent boundary layer. *14th European Fluid Mechanics Conference*.

## Authorship statement

Chapter 3 and 4 are based on the following manuscripts:

(1) Pang, M., & Chauhan, K. (2022). Measurements of scalar in buoyant plumes in a turbulent boundary layer. *Australasian Fluid Mechanics Conference 2022*.

(2) Pang, M., & Chauhan, K., & Talluru, K. M. (2023). Measurements of buoyant plumes in a turbulent boundary Layer. *Experiments in Fluid Mechanics*. (*in preparation*)

Material preparation, data collection, and analysis were primarily conducted by Miaoyan Pang. Dr Kapil Chauhan guided the experimental design and data analysis. Dr Krishna Murali Talluru provided suggestions on the data analysis. The first draft of the manuscript was written by Miaoyan Pang, and Dr Kapil Chauhan provided feedback on previous versions.

Chapter 6 is based on the following submitted manuscript:

Pang, M., & Chauhan, K. (2022). Probabilities of high-concentration events in scalar point-source plume in a turbulent boundary layer. *12th International Symposium on Turbulence and Shear Flow Phenomena*.

Data analysis and the manuscript draft were primarily prepared by Miaoyan Pang. Dr Kapil Chauhan provided suggestions on analysis and provided feedback on the drafts. Both authors read and approved the final manuscript.

Chapter 7 is based on work to be submitted as:

Pang, M., & Chauhan, K., & Talluru, K. M. (2023). Vertical scalar fluxes of buoyant plumes in a turbulent boundary layer. *Journal of Fluid Mechanics*. (*in preparation*)

Manuscript preparation and data analysis were conducted by Miaoyan Pang. All authors contributed to the study's conception and design.

In addition to the statements above, in cases where I am not the corresponding author of a published item, permission to include the published material has been granted by the corresponding author.

Miaoyan Pang

30/6/2023

As the primary supervisor for the candidature upon which this thesis is based, I can confirm that the authorship attribution statements above are correct.

Dr Kapil Chauhan

30/6/2023

## Acknowledgements

I would like to express my sincere gratitude and appreciation to the following individuals who have played a significant role in the completion of my research and the writing of this thesis:

First and foremost, I am deeply grateful to my supervisors, Dr Kapil Chauhan and Dr Talluru Murali Krishna, for their unwavering support and guidance. My fluid mechanics journey began with Dr Krishna's guest lecture in my second-year environmental engineering subject back in 2017, which sparked my interest in fluid mechanics. The guest lecture focused on the first series of neutral plume measurements in our lab, which laid a solid foundation for this thesis. Subsequently, Dr Chauhan offered me my first research assistant position in the wind tunnel, marking the beginning of my enriching journey in the field of fluid mechanics.

I am incredibly grateful for Dr Kapil Chauhan's thoughtful guidance, patience, and mentorship throughout this entire research project. Despite his demanding schedule, he has provided detailed instructions and valuable insights to help me set up the experiments. His exceptional ability to break down complex concepts into clear and concise explanations has been invaluable to my understanding and progress.

I would like to express my appreciation to my secondary supervisor, Krishna, for his valuable feedback on my manuscripts and his guidance in data processing and analysis. His insights and suggestions have greatly contributed to the quality of my research and have enhanced the overall outcomes of this work.

I extend my gratitude to Mr. Theo Gresley-Daines, our lab technician, for his invaluable assistance in designing, fabricating and assembling the experimental setup. His expertise and experience in the workshop have saved me from pursuing experimental setups that would not have worked, ultimately saving a significant amount of time and effort. I would like to acknowledge Mr Zachary Benitez, who may no longer be working in our wind tunnel but played a crucial role as a technician at the beginning of my research journey in the wind tunnel. His suggestions and guidance were instrumental in getting me started and setting up the necessary equipment.

I am deeply grateful to my examiners, Professor Pietro Salizzoni and Associate Professor Christina Vanderwel, for their invaluable and insightful comments. Their expertise and constructive feedback significantly contributed to the refinement of this thesis.

To my family, I am forever grateful. Without the support and encouragement of my parents, I would not have been able to pursue this research journey. 谢谢父母。I am also grateful to my grandparents, uncle, and aunt for their care and support during my time overseas.

I would like to thank Joanne for introducing me to the diary metaphor and the "negative thoughts bin." Her guidance on how to concentrate and relax under pressure has been immensely helpful throughout this challenging research process.

Lastly, I deeply appreciate the companionship and moral support from my friends, Leo, Nicole, Tu, and Yuwei.

To all those mentioned above and to anyone else who has contributed to my academic and personal growth, I extend my deepest thanks from the bottom of my heart.

# Contents

# List of figures

# List of tables

CHAPTER 1

# Introduction

## 1.1 Motivation

Air pollution, consisting of particulate and toxic pollutants (collectively known as contaminants), contributes to approximately 7 million deaths annually from respiratory diseases (World Health Organization 2021). Figure 1.1 shows an illustration of a puff or parcel of pollution released from a chimney stack near an urban area. The downstream development of the release depends on several local factors. Here three such factors are emphasised. The first one is the variation of wind velocity in the vertical direction in the first few hundred metres from the surface. This is also called the atmospheric surface layer, which is a boundary layer and causes a shearing effect. Secondly, the roughness of the ground due to the presence of buildings and vegetation, as shown in figure 1.1, will influence the velocity profile by introducing three-dimensional flow and thereby entrap pollutants between them. The third one is the density or temperature (which directly influences the density) of the source gas relative to the ambient air. If the temperature of the plume is higher or the plume is less dense than air, it tends to float, termed *positively buoyant*, as shown by the red-lined plume in figure 1.1. On opposite occasions, when the temperature is lower, or the density is higher, the plume sinks and is *negatively buoyant*, as shown by the blue-shaded plume in figure 1.1. This thesis focuses on buoyancy effects in a plume released from a point source.

The Global Air Quality Guidelines advise policy-making on the major health-damaging air pollutants: particulate matter, ozone, nitrogen dioxide, and sulphur dioxide (World Health Organization 2021). Among them, sulphur dioxide and nitrogen oxides are heavier than air and are emitted from fossil fuel combustion. Other dense pollutants are liquefied natural gas (LNG), carbon dioxide ($CO_2$) and hydrogen fluoride (fluorane or HF) (Witlox 1994). The

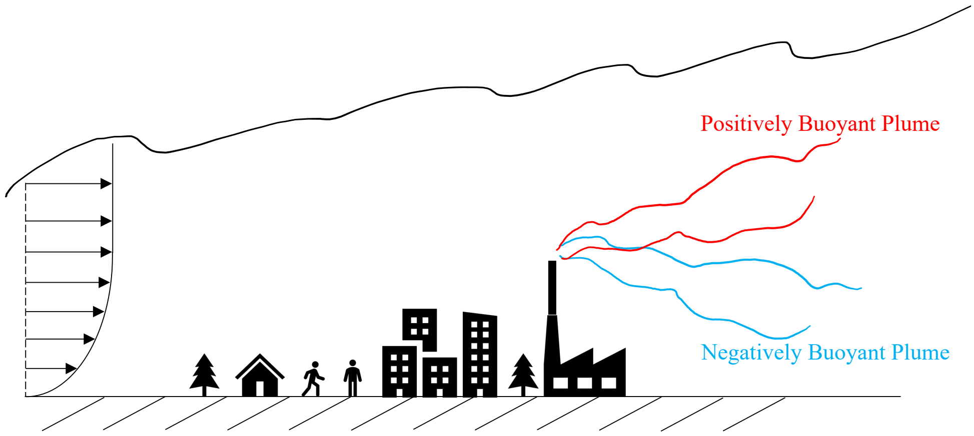


FIGURE 1.1: Heavy or light plume released in an atmospheric boundary layer in an urban environment with various roughness.

particulates being transported might deposit on plants and water bodies or be inhaled into respiratory systems, causing acute or chronic respiratory illnesses (Dennekamp and Abramson 2011). Smoke from bushfires or volcanoes has a high temperature and therefore rises due to lower density relative to the surrounding air. Eventually, the hot gases cool down and settle towards the ground after being transported over hundreds of kilometres by the wind. Reisen and Brown (2006) found that extended bushfires are linked with elevated respiratory-related symptoms in North America, Australia and South-East Asia.

Predicting severe events in these accidents is crucial to take precautions in the early stages of a fire or chemical leak. The air quality of the Greater Sydney region (and many big cities across the globe) is forecast daily. However, the accuracy and the ability to predict extreme high-concentration events of such models require improvements (NSW Department of Planning and Environment 2022). By studying the experimental data acquired in a controlled laboratory environment, the model can be refined to better predict plume evolution and extreme high-concentration events.

Dispersion models are necessary to advise air quality management policy and/or planning of human activity that releases contaminants or near contaminant releases (e.g. towns in the vicinity of open-pit mines). The spread of heavier or lighter gas in an atmospheric boundary layer is a complex phenomenon because of the number of parameters involved, including the properties of the gas, the background flow, the terrain, the geometry of release, etc. A reliable model should consider these factors and predict the mean concentration and the severity of possible high-concentration events with acceptable accuracy. To this end, high-fidelity experimental data on this phenomenon aids in developing empirical models and validating theories that also act as benchmark or calibration data.

Despite the significant interest and advances in understanding plume dispersion, a gap remains in the literature to compare three buoyancy cases: neutral, positively buoyant, and negatively buoyant plumes. To date, experiments have only focused on one or two of these cases, making it challenging to understand plume behaviour across all three conditions comprehensively. Moreover, the experimental setups and parameters in previous studies are often not similar, making it difficult to compare data collected quantitatively. As a result, there is a need for an experimental study that systematically compares plume dispersion across all three buoyancy conditions under the same experimental setup and parameters. Such an experiment would fill an essential gap in the research and provide a practical examination of plume dispersion under different buoyancy conditions.

## 1.2 Problem definition

A plume is formed when a substance, specifically the concentration of a scalar, is released into a flow. In this study, the dispersion of scalar concentration rather than heat is examined in a turbulent flow. The spread of the scalar within the turbulent flow is influenced by two mechanisms: molecular diffusion and turbulent mixing. Both the properties of the scalar and the characteristics of the ambient flow can impact the dispersion downstream. The critical parameters for plume dispersion are identified in Figure 1.2.

Several quantities are varied in this investigation, as indicated by the blue labels in the figure. The density ratio between the source and the ambient fluid, denoted as $\rho_s/\rho_\infty$, determines whether the plume exhibits positive ($\rho_s/\rho_\infty < 1$) or negative buoyancy ($\rho_s/\rho_\infty > 1$). Inside the boundary layer, the mean velocity profile, $U(z)$, is a function of the distance from the wall, which is varied by modifying the roughness of the wall. The source height, $S_z$, is also varied to account for variations in the mean and fluctuation of local velocity at different heights in the TBL. The plume's evolution in each scenario is examined by taking measurements at the various source distances, $S_x$.

The variables highlighted in red are the subject of detailed analysis. This includes investigating the time-averaged and fluctuating concentration fields and studying the probability density function of concentration and its associated parameters. The scalar fluxes, $u_i c$, which are the cross-correlation between the concentration field and the velocity field, are also explored.

To maintain focus and limit the scope of this research, certain aspects are excluded. The effect of source size, $d_s$, is not investigated, and the study is limited to chemically inactive scalars. Furthermore, this thesis specifically examines plumes that are released iso-kinetically in a dynamic flow field, where the source velocity, $U_s$, is set equal to the local mean velocity. This choice minimises the shearing effect between the plume and the background flow. Other real-life scenarios, such as the stability of turbulent boundary layers, cannot be experimentally studied here.

These specific research parameters and constraints shape the scope of this study, enabling a thorough examination of plume dispersion dynamics within a controlled experimental environment.

## 1.3 Thesis outline

A literature review is conducted in the next chapter (2) to explore the existing knowledge on turbulent boundary layer characteristics and plume dispersion. This chapter will summarise the key theories, models, and experimental findings related to the behaviour of buoyant plumes in turbulent flows. The experimental setup developed specifically for studying buoyant plumes will be described in detail in chapter 3. Chapter 4 will focus on the mean behaviour and root-mean-square (RMS) characteristics of buoyant plumes, including the three Gaussian parameters required to describe the profiles fully. The findings regarding the average plume

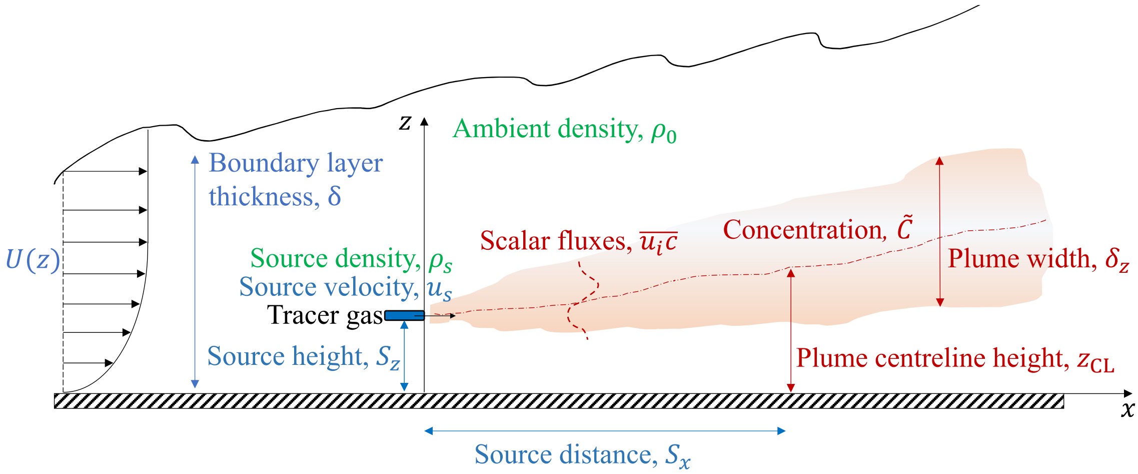


FIGURE 1.2: Critical experimental parameters (marked in blue) in this study. The scaling relations (marked in red) for rise height ($z_c$), plume width ($\delta_z$), and fluxes ($\overline{u\theta}$, $\overline{uc}$) are the unknown quantities, which are planned in this project.

behaviour, including the plume centreline location and half-width, will be presented and analysed. The higher central moments of concentration, ranging from the 2nd to the 6th moment, and their similarity will be examined in chapter 5. Chapter 6 will examine the shape and characteristics of the probability density function of full signal concentration and extreme concentration events of neutral plumes. The scalar fluxes and a newly proposed scalar-flux relationship for plumes will be investigated in chapter 7. Chapter 8 will explore the effect of roughness on the dispersion of buoyant plumes. The final chapter will provide a summary of the research findings and highlight the research gaps filled by this thesis, along with recommendations for future research directions.

CHAPTER 2

# Literature review

---

## 2.1 Introduction

The dispersion of a plume in turbulent flow is governed by two primary mechanisms: molecular diffusion and turbulent mixing. Turbulent mixing is particularly efficient in comparison to molecular diffusion when it comes to the mixing of scalars. In cases where the turbulent intensity is high, the contribution of molecular diffusion can be neglected. Therefore, a comprehensive understanding of plume behaviour in a turbulent boundary layer necessitates a thorough investigation of the characteristics of turbulent boundary layers.

Turbulent flow is characterised by chaotic and random fluid motion. The nonlinear nature of turbulence makes it challenging to predict its behaviour, as small disturbances upstream can result in significant differences downstream. While the motion of individual fluid particles can be described by the Navier-Stokes equations, which are a set of nonlinear partial differential equations, analytical solutions are only available for simplified laminar flows. The complexity of turbulence is further compounded by the wide range of motions involved, spanning from the dissipating Kolmogorov scales to the motion of fluid particles and coherent structures comparable to the size of the flow field. Modelling such a broad range of scales requires substantial computational resources, posing a significant challenge in the simulation of turbulent flows.

Consequently, statistical approaches are commonly employed in turbulence studies, focusing on the statistical behaviour or bulk properties of interest rather than instantaneous quantities (e.g. Taylor 1935; Heisenberg 1948). Prominent examples include energy spectra, which provide insights into energy distribution at different wavelengths (Kaimal et al. 1972).

Observations from numerous studies have revealed the existence of repetitive patterns in wall-bounded turbulent flows. These coherent structures, such as hairpin vortices, near-wall streaks, ejections and bursts, advect as coherent entities over downstream distances and play a crucial role in generating and dissipating turbulence (Robinson 1991). Smaller eddies are found near these coherent structures, and energy is transferred from larger eddies to smaller ones as part of the energy cascade process.

Several factors influence the dispersion of a plume in a turbulent boundary layer. When a scalar is released into the turbulent flow, the plume undergoes meandering motion due to turbulent events, while the surrounding fluid of lower density entrains the plume. The inherently chaotic nature of turbulence leads to random dispersion of the scalar in the flow field. As a result, statistical analysis is commonly employed to study plume dispersion, considering the random nature of instantaneous dispersion. Furthermore, the complexity of plume dispersion increases when there is a density difference between the plume and the ambient fluid.

This literature review aims to provide a comprehensive understanding of downstream plume development in a turbulent boundary layer. Section 2.3 investigates the characteristics of turbulent boundary layers and the background flow associated with this phenomenon. In section 2.4, the dispersion of neutrally buoyant and buoyant plumes is examined.

## 2.2 Governing equations

There are three main governing equations: the continuity equation, the Navier-Stokes equation and the transport equation. The latter two equations are discussed in detail here.

### 2.2.1 Navier-Stokes equation with buoyancy considerations

The notation used in this thesis is defined in figure 2.1, where $x$ is the streamwise distance, $y$ is the spanwise distance, and $z$ is the wall-normal distance. The motion at each point in a flow is a function of space and time, $\tilde{U}_i = f(x, y, z, t)$. From the law of Conservation of

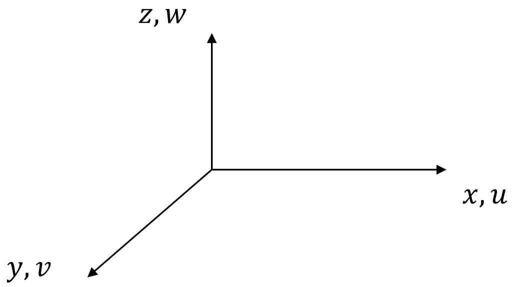


FIGURE 2.1: Coordinate system adopted in this thesis.

Momentum in three dimensions, any conserved flow field must satisfy the Navier-Stokes Equation:

$$\frac{\partial \tilde{U}_i}{\partial t} + U_j \frac{\partial \tilde{U}_i}{\partial x_i} = -\frac{\tilde{P}}{\rho} + \nu \frac{\partial^2 \tilde{U}_i}{\partial x_i^2} \tag{2.1}$$

where the subscript $i$ is the direction notation, $U_i$ is velocity, $t$ is time, $x_i$ is the location, $\tilde{P}$ is the pressure, and $\nu$ is the viscosity.

In turbulent flows, the fluctuation of dependent variables necessitates their decomposition into mean and fluctuating components. The streamwise instantaneous velocity, $\tilde{U}$, for example, can be expressed as the sum of the mean velocity, $U$, and the fluctuating component, $u$, in mathematical terms: $\tilde{U} = U + u$. By decomposing the dependent variables in Equation 2.1 and considering incompressible flow (constant density, $\rho$), the Reynolds-averaged Navier-Stokes equation can be obtained by averaging each term:

$$U_j \frac{\partial U_i}{\partial x_j} + \frac{\partial \overline{u_i u_j}}{\partial x_j} = -\frac{1}{\rho}\frac{\partial P}{\partial x_i} + \nu \frac{\partial^2 U_i}{\partial x_j^2} \tag{2.2}$$

Here, the over-line represents the mean value of a term, and $\overline{u_i u_j}$ is known as the Reynolds stress or momentum flux. The Reynolds-averaged Navier-Stokes equations in three dimensions, along with the Continuity Equation, comprise four equations. However, there are more than four unknowns: $U_i$, $p$, and $\overline{u_i u_j}$ (Pope 2000). Since the value of $\overline{u_i u_j}$ is not known in advance, the Reynolds-averaged Navier-Stokes equation remains open.

The turbulent-viscosity theory provides one way to close the Reynolds-averaged Navier-Stokes (RANS) equation, eliminating the Reynolds stress term from the equation. The turbulent viscosity is defined as:

$$-\overline{u_i u_j} = \nu_T \left( \frac{\partial U_i}{\partial x_j} + \frac{\partial U_j}{\partial x_i} \right) - \frac{2}{3} k_T \delta'_{ij} \tag{2.3}$$

In this equation, $k_T$ represents the turbulent kinetic energy, $\nu_T$ is the eddy viscosity, and $\delta_{ij}$ denotes the tensor. By expressing the unknown $\overline{u_i u_j}$ in terms of $U_i$, the Reynolds-averaged Navier-Stokes equation can be closed.

The density of positively or negatively buoyant plumes is distinguished from the ambient environment. This density difference affects the energy balance of turbulent motions, the velocity history of fluid particles, and the body force exerted on the plumes (Csanady 1973). Consequently, buoyant plumes are often referred to as active scalars, in contrast to neutral plumes, which act as passive scalars. In addition to density, the pressure and viscosity of the flow are also influenced by density. To simplify the analysis, the Boussinesq assumption is commonly employed. This approximation assumes that when the density difference between the ambient fluid and the plume is small, the density difference can be neglected, except in the body force term. For a flow field that satisfies the Boussinesq assumption, equation 2.1 is modified to include the body force generated by buoyancy.

$$\frac{\partial \tilde{U}_i}{\partial t} + \tilde{U}_j \frac{\partial \tilde{U}_i}{\partial x_i} = -\frac{P}{\rho_\infty} + \nu \frac{\partial^2 \tilde{U}_i}{\partial x_i^2} + (\rho - \rho_\infty) g \tag{2.4}$$

According to Schatzmann and Policastro (1984), when $\dfrac{\rho - \rho_\infty}{\rho_\infty} = 0.5$, the prediction of the height of maximum plume concentration differs by 20%. Therefore one should consult the criteria developed before applying the assumption to this problem, such as Gray and Giorcini 1976; Hamimid et al. 2021.

### 2.2.2 Transport equation

The transport equation can describe the instantaneous concentration field,

$$\frac{\partial \tilde{C}}{\partial t} + \tilde{U}_i \frac{\partial \tilde{C}}{\partial x_i} = \gamma \frac{\partial^2 \tilde{C}}{\partial x_i^2}, \tag{2.5}$$

where $\tilde{C}$ is the instantaneous concentration, and $\gamma$ is the molecular diffusivity of the scalar in the fluid. The instantaneous concentration equals the sum of its mean and fluctuations: $\tilde{C} = C + c$. Similar to the Navier-Stokes equation, the transport equation has a Reynolds-averaged form:

$$\frac{\partial C}{\partial t} + U_i \frac{\partial C}{\partial x_i} + \frac{\partial \overline{u_i c}}{\partial x_i} = \gamma \frac{\partial^2 C}{\partial x_i^2} \tag{2.6}$$

The Reynolds-averaged transport equation cannot be closed because $\overline{u_i c}$, the scalar flux, is unknown. One way to close this equation is by applying the gradient diffusion hypothesis, analogous to the turbulent-viscosity theory in equation 2.3, where a coefficient is introduced to relate the flux with the mean gradient,

$$-\overline{u_i c} = \kappa_{ij} \left( \frac{\partial C}{\partial x_j} \right) \tag{2.7}$$

Here $\kappa_{ij}$ is the turbulent diffusivity or eddy diffusivity tensor. This hypothesis was employed by Smith (1957) and Robins (1978) for the numerical solution of the concentration field. Csanady (1967), on the other hand, applies this to the conservation of scalar standard deviation equation

$$\overline{u_i c^2} = -K_s \frac{\partial \overline{c^2}}{\partial x_i} \tag{2.8}$$

where $K_s$ is the turbulent diffusivity for the standard deviation. Sykes et al. (1986) and Sykes and Gabruk (1997) adopted a second-order hypothesis to close the transport equation. This is not the focus of this thesis and hence will not be discussed. Though these closure hypotheses provide a solution to the Reynolds-averaged transport equation, the solution is only for the mean concentration field, and no information on higher moments of concentration or the extreme events (e.g. the peak-to-mean concentration ratio) is available.

For this phenomenon, the following three assumptions can be adopted for a simplified transport equation: 1) molecular diffusion is significantly smaller than eddy diffusion; 2) the direction of the mean flow is in the $x$ direction; and 3) the plume is thin, *i.e.* $\partial\overline{uc}/\partial x \ll \partial\overline{wc}/\partial z$ and $\partial\overline{uc}/\partial x \ll \partial\overline{vc}/\partial y$. The simplified Reynolds-averaged transport equation is written as,

$$U \frac{\partial C}{\partial x} = -\frac{\partial \overline{wc}}{\partial z} - \frac{\partial \overline{vc}}{\partial y} \tag{2.9}$$

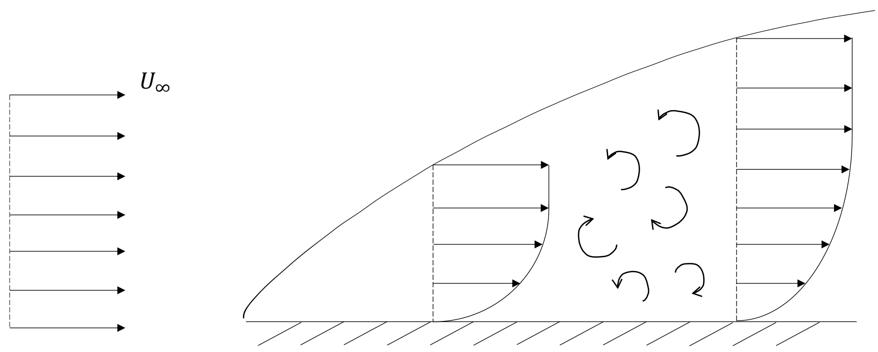


FIGURE 2.2: The development of a boundary layer along a flat surface.

## 2.3 Turbulent boundary layer

### 2.3.1 Turbulent boundary layer over smooth wall

The formation of a Turbulent Boundary Layer (TBL) is illustrated in figure 2.2. A uniform flow with a velocity of $U_\infty$ and finite viscosity approaches from the left. When this flow encounters a solid surface, the velocity at the surface becomes zero due to viscosity, known as the no-slip condition, $U = 0$ at $z = 0$. However, the existence of the mean flow dictates that the velocity must be non-zero elsewhere. Consequently, the velocity increases with distance from the surface, forming a region with a velocity gradient known as the boundary layer (BL). The theory of boundary layers was initially proposed by Prandtl (1905), who derived the boundary layer equations for a simplified case of a two-dimensional stable BL with constant streamwise pressure.

After a certain distance downstream from the initiation of the BL, the flow intermittently transitions into a turbulent state. Once the flow becomes fully chaotic within this region, it is commonly called the TBL. The thickness of a BL is generally denoted as $\delta$. A turbulent boundary layer can be characterised by the Reynolds number,

$$Re_\delta = \frac{U_\infty \delta}{\nu} \tag{2.10}$$

Here $\nu$ is the viscosity. Another commonly used non-dimensional diameter is the friction Reynolds number, defined as

$$Re_\tau = \frac{u_\tau \delta}{\nu}. \tag{2.11}$$

Here $u_\tau = \sqrt{\tau_w/\rho}$ is the friction velocity, and $\tau_w$ is the wall shear stress.

#### 2.3.1.1 Wall regions in a TBL

Turbulent motions exist within the Turbulent Boundary Layer (TBL) and exhibit scale variations, as discussed in section 2.2.1. The range of average motions differs closer to the wall compared to further away from it. A canonical TBL can be divided into several distinct regions, each characterised by its unique velocity profile in dimensionless form along the direction of the mean flow.

In the inner layer, viscosity, $\nu$, and the local velocity fluctuation are the dominating scale (chapter 5 in Tennekes and Lumley 1972), rather than $\delta$ and $U_\infty$. This is the law of the wall (Prandtl 1925). It is useful to define the friction velocity, $u_\tau$, as the velocity scale and use it to normalised velocity and wall-normal distance,

$$U^+ = \frac{U}{u_\tau}$$

$$z^+ = \frac{z u_\tau}{\nu}$$

The law of the wall can then be written mathematically,

$$U^+ = f_w(z^+) \tag{2.12}$$

where $f_w$ is a universal non-dimensional function for channel flow, pipe flow, and BL (Pope 2000). The viscous sub-layer is located at $z^+ < 5$, where $f_w(z^+) \approx z^+$ (Pope 2000).

In the vicinity of the boundary layer edge, the free stream velocity and the boundary layer thickness become more significant compared to the viscous scales. Moreover, “the similarity law has to be integrated from outside the BL toward the wall in order to obtain a similarity law for $U$” (chapter 5 in Tennekes and Lumley 1972). This leads to the formulation of the velocity defect law (Kármán 1930):

$$\frac{U_\infty - U}{u_\tau} = F_D\left(\frac{z}{\delta}\right) \tag{2.13}$$

where $F_D$ represents a non-dimensional function that varies depending on the flow conditions.

The region where the inner and outer scales overlap is commonly referred to as the inertial sub-layer or the logarithmic region. In this region, the velocity profile can be described by the logarithmic law of the wall proposed by Kármán (1930):

$$U^+ = \frac{1}{\kappa}\ln z^+ + B_1 \tag{2.14}$$

where $\kappa$ represents the von Kármán constant and $B_1$ is a constant term. The value of $\kappa$ is typically around 0.4±0.01 (Högström 1996). Alternatively, this relationship can be expressed as a power law (George and Castillo 1997; Nironi et al. 2015):

$$\frac{U}{U_\infty} = \left(\frac{z}{\delta}\right)^{n'} \tag{2.15}$$

#### 2.3.1.2 The mean velocity profile

Figure 2.3 illustrates typical velocity profiles in TBLs at various $Re_\tau$ values.

Coles (1956) proposed that the boundary layer profile can be described as a linear combination of the law of the wall and the law of the wake:

$$U^+ = \frac{1}{\kappa}\ln(z^+) + B_1 + \frac{\Pi}{\kappa}\mathcal{W}(\frac{z}{\delta}) \tag{2.16}$$

Here, $\mathcal{W}$ is the wake function, $\Pi$ is a profile parameter, and $B_1$ is a constant. The law of the wake, which is purely empirical, accounts for "the departure of the velocity profile from the logarithmic law by a universal function" (Tani 1977).

Musker (1979) modified the law of the wall employing a polynomial wake function. Chauhan et al. (2009) proposed a composite fit for the velocity profile, which takes into account all regions within a TBL and incorporates an exponential wake function in addition to Musker's law of the wall.

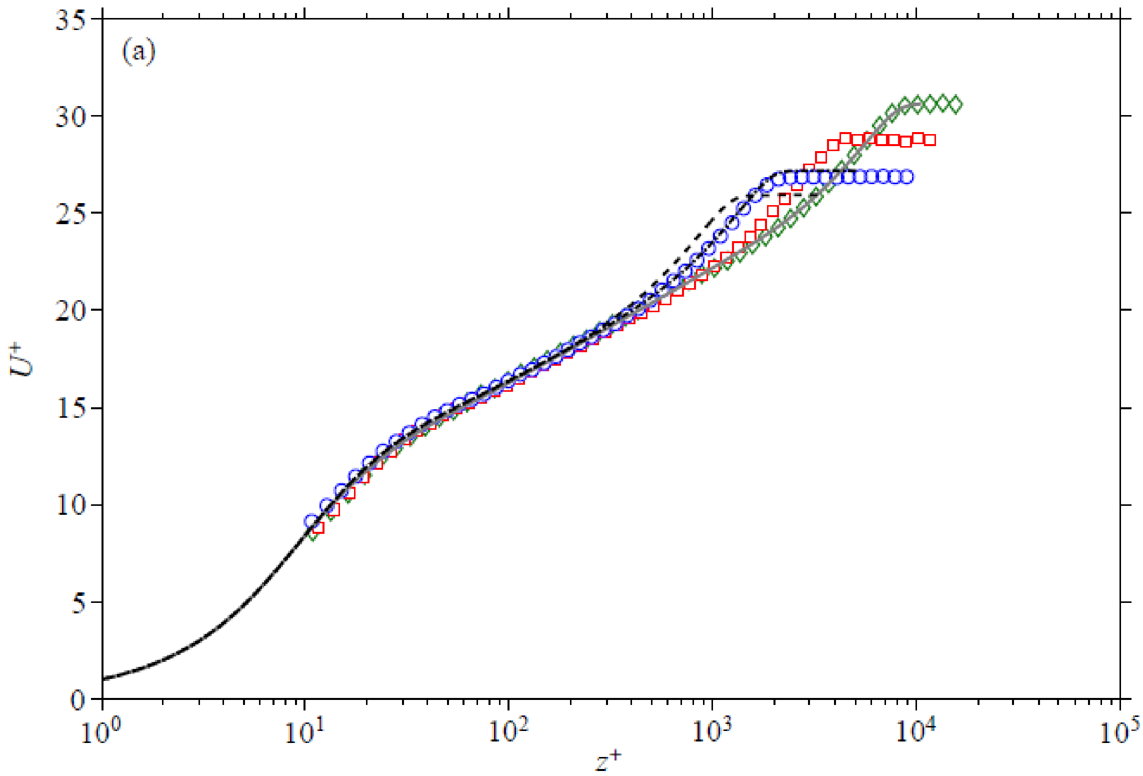


FIGURE 2.3: The mean velocity profile in typical TBLs. Dashed line: DNS results, $\delta_{99}^+ = 1270$; dashed-dotted line: $\delta_{99}^+ = 1990$; grey solid line: formulation at $Re_\tau = 10000$; circle: $\times$-wire results at $Re_\tau \approx 2500$, square: $\times$-wire results at $Re_\tau \approx 5000$; diamond: $\times$-wire results at $Re_\tau \approx 10000$. Adapted from figure 5.7 (*a*) in Baidya (2016).

#### 2.3.1.3 Spectra

The energy spectra $E(k)$ can be calculated by applying discrete Fourier transform to instantaneous velocity, $\tilde{U}_i(t)$. Here $k$ is the wavenumber. For example, for the streamwise velocity,

$$E(k) = \int_{-\infty}^{\infty} \tilde{U}(t) e^{-i2\pi t f} dt \tag{2.17}$$

Energy spectra provide valuable information about energy distribution across different scales of motion in a flow. Figure 2.4 illustrates a typical energy spectrum in a TBL. In 1941, Kolmogorov proposed the famous K41 theory, which states that in high-Reynolds-number flows, turbulence energy is dissipated isotropically through the smallest eddies at a universal rate $\epsilon$ due to viscosity. This dissipation process occurs in the dissipation range of the energy spectrum, as depicted in figure 2.4. K41 also states that within the inertial subrange, the

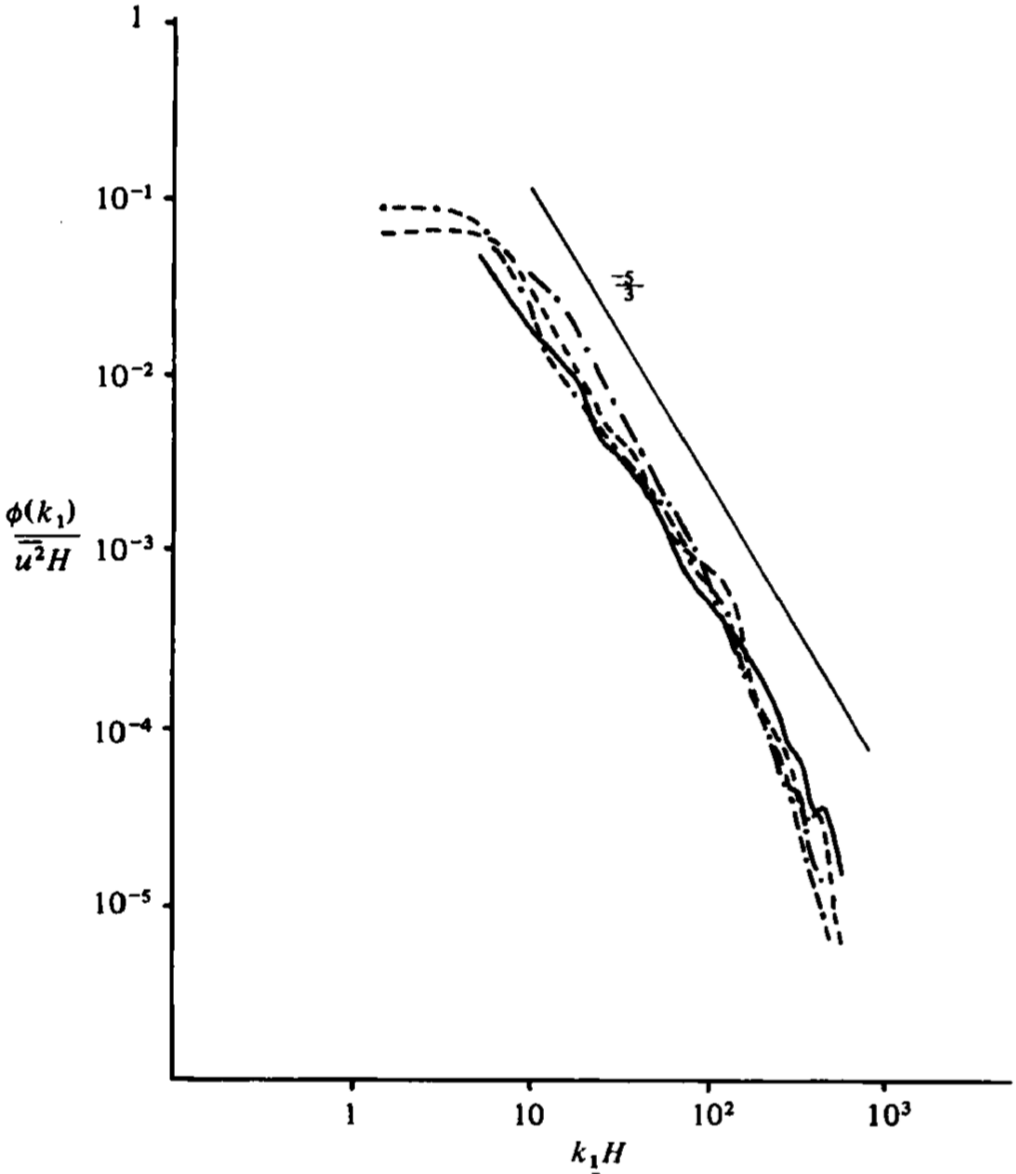


FIGURE 2.4: Typical energy spectrum in a turbulent boundary layer with a $-5/3$ slope in the inertial subrange (Fackrell and Robins 1982).

energy spectra exhibit a power-law behaviour with a slope of $-5/3$ on a logarithmic scale, given by

$$E(k) = \alpha\epsilon^{2/3}k^{-5/3} \tag{2.18}$$

Here, $\alpha$ is a universal constant, approximately 0.5 (Kaimal et al. 1972). In the wind tunnel-generated turbulent boundary layer, this subrange can extend over one to two decades (Fackrell and Robins 1982).

### 2.3.2 Turbulent boundary layer over rough wall

In the previous section, the focus was on smooth wall TBLs. This section provides a brief overview of rough wall TBLs. The presence of roughness elements in the flow affects the velocity field by introducing a new length scale into the problem. The size and arrangement of these elements play a significant role in modifying the velocity profile. Moreover, introducing roughness can enhance the mixing of momentum and scalar quantities by increasing turbulence levels in the flow. Roughness elements can also act as traps retaining scalar substances within their structures. In the atmospheric boundary layer (ABL), the velocity profile is further modified by buildings and vegetation, which act as natural roughness elements. Additionally, various dispersion events occur in the ABL, such as volcanic eruptions and chimney exhaust emissions. Therefore, studying TBLs over roughness is crucial for gaining insights into scalar dispersion processes in the ABL.

The layer occupied by and near the roughness is commonly referred to as the inner layer, drawing an analogy to the inner/viscous layer in smooth wall TBLs. However, it is important to note that the velocity profiles and the characteristics of this inner layer in rough wall TBLs are different. In this inner layer, the velocity profile and the friction velocity at the surface, $u_\tau$, are strongly influenced by the size and arrangement of the roughness elements. In contrast, the outer region, which lies beyond the inner layer, follows the wall similarity hypothesis proposed by Raupach et al. (1991), building upon the concept of Reynolds number similarity introduced by Townsend (1956, p. 53). According to this hypothesis, in the outer region of high Reynolds number flows over rough walls, the scaling laws governing the velocity profile, such as the logarithmic law (equation 2.14) and the velocity defect law (equation 2.13), are unaffected by the viscous length scale. However, the relative location of these regions within the boundary layer, the friction velocity $u_\tau$, and the boundary layer thickness $\delta$ are influenced by the presence of roughness. A large number of experiments performed afterwards proved the hypothesis to be valid (Flack et al. 2005; Connelly et al. 2006; Wu and Christensen 2010; Kim et al. 2020, among others).

Introducing roughness elements into a TBL leads to a downward shift of the velocity profile in wall units compared to that of a smooth wall. This shifted velocity profile can be expressed mathematically as follows:

$$U^+ = \kappa^{-1} \log z^+ + 5.1 + \frac{\Pi}{\kappa}\mathcal{W}(z/\delta) - \Delta U^+ \tag{2.19}$$

Here, $\Delta U^+$ represents the displacement length or roughness function (Jiménez 2004). An alternative expression is given by:

$$U^+ = \kappa^{-1} \log(z/k_s) + C_1 + \frac{\Pi}{\kappa}\mathcal{W}(z/\delta) \tag{2.20}$$

In this equation, $k_s$ denotes the equivalent sand grain roughness introduced by Nikuradse (1933), and $C_1 = 8.5$ corresponds to fully rough flow (Schlichting and Gersten 2016). The parameter $k_s^+ = k_s/(u_\tau/\nu)$, where $u_\tau$ is the friction velocity. The resemblance between the above equations and equation 2.16 can be observed. Figure 2.5 illustrates typical velocity profiles for different $\Delta U^+$ values in rough wall TBLs.

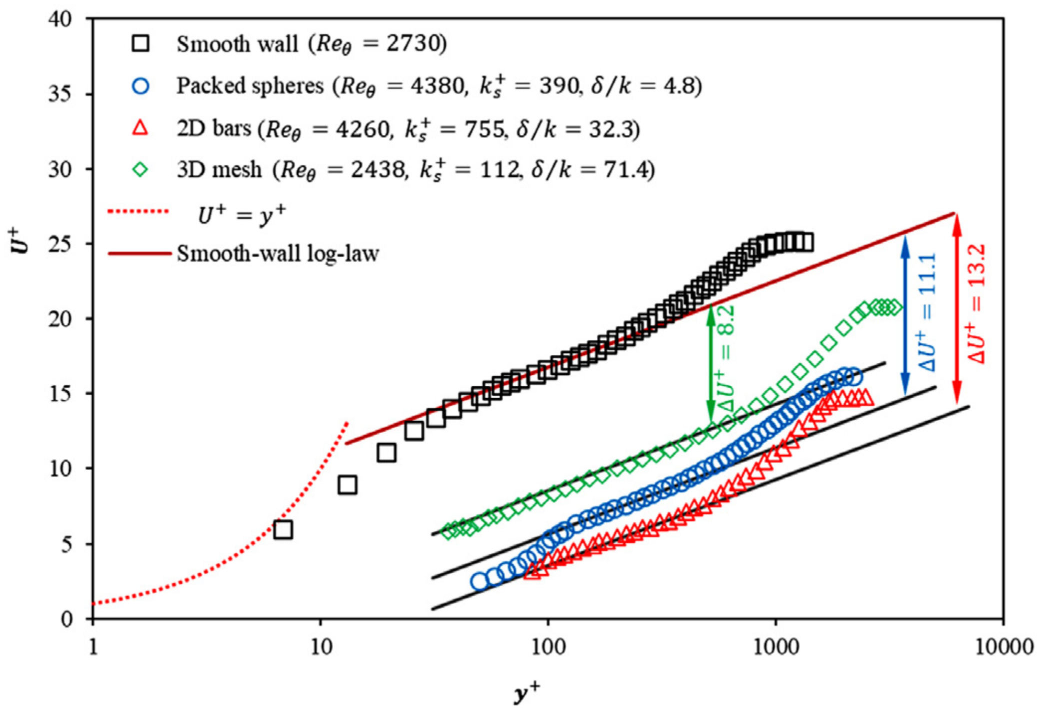


FIGURE 2.5: Mean velocity profiles of rough wall TBLs, depicting the downward shift $\Delta U^+$ compared to a smooth wall TBL (Kadivar et al. 2021). In this thesis, the vertical axis $y^+$ is interchanged with $z^+$.

The value of $k_s^+$ is utilised to classify boundary layer flows into three regimes based on roughness characteristics, as presented in table 2.1. Although the exact limits are not well-defined, the numbers in the table provide a general indication (Jiménez 2004; Abdelaziz et al. 2022).

| Category | Range of $k_s^+$ | Characteristics |
|---|---|---|
| Dynamically smooth | $k_s^+ \leq 5$ | "Roughness does not have a noticeable effect on the viscous sub-layer" |
| Transitionally rough | $k_s^+ \leq 70$ | "Both the pressure drag and the viscous drag contribute to the total drag" |
| Fully rough | $k_s^+ > 70$ | "A log-linear relationship between $\Delta U^+$ and $k_s^+$" |

TABLE 2.1: Turbulent flow regimes according to the size of the roughness elements are normalised by viscous units (Raupach et al. 1991; Kadivar et al. 2021).

The challenging aspect of applying the aforementioned equations is accurately calculating the friction velocity, $u_\tau$. While direct measurement of $u_\tau$ is preferred, it may not always be feasible in practice. One approach to calculating $u_\tau$ is by fitting the logarithmic law. Another method involves using the velocity defect chart proposed by Djenidi et al. (2019). This method relies on the wall similarity hypothesis, where the velocity defect in wall units, obtained from $u_\tau$, is compared to a 'standard' velocity defect profile derived from Direct Numerical Simulation (DNS) data.

The categorisation of roughness based on its size relative to the pipe diameter was first introduced by Perry et al. (1969). In the original paper, the roughness size is denoted as $k$, while the pipe diameter or boundary layer thickness is represented by $d$. Two types of roughness are depicted in figure 2.6 ($a$) and ($c$) below. For $k$-type roughness, the shift, denoted as $k_s^+$, depends on the size of $k$. Conversely, in the case of $d$-type roughness, the roughness size is comparable to $d$, and the downshift is proportional to $d$ rather than $k$, hence its name.

However, Jiménez (2004) cautioned that the conclusions regarding $d$-type roughness in the paper by Perry et al. (1969) should be interpreted carefully due to the limited range of $k/d$ ratios studied (10-20). Jiménez (2004) stated that $d$-type roughness "offers a way of constructing boundary layers with a single length scale... $d$-type layers have only outer scales". More recently, an intermediate type of roughness has been proposed by Li and Li (2020), where eddies of two different strengths are observed, as shown in figure 2.6 (*b*).

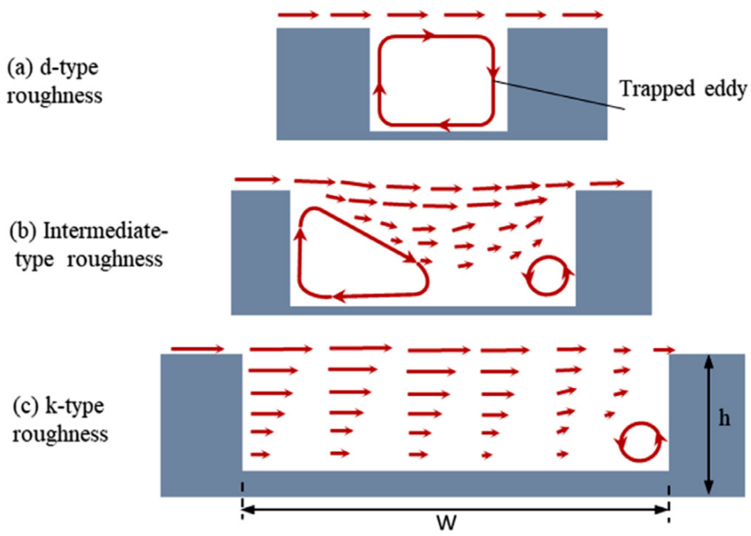


FIGURE 2.6: Geometry and eddies of (*a*) $d$-type, (*b*) intermediate type, and (*c*) $k$-type roughness. (Kadivar et al. 2021).

## 2.4 Plume dispersion

There are three important non-dimensional parameters in this phenomenon. The source Reynolds number,

$$Re_s = \frac{u_s d_s}{\nu} \tag{2.21}$$

with $u_s$ being the source velocity and $d_s$ the source diameter. The Richardson number is the ratio of buoyancy force and the inertial force, which equates to the ratio of density difference and the source velocity of the plume (Chakravarthy et al. 2018),

$$Ri = g\frac{d_s}{2}\frac{\rho_\infty - \rho_s}{\rho_s u_s^2}. \tag{2.22}$$

Sometimes the densiometric Froude number is adopted, which is the inverse of $Ri^2$,

$$Fr = \frac{u_s}{\sqrt{g' d_s}} \tag{2.23}$$

where $g' = g\dfrac{|\rho_s - \rho_\infty|}{\rho_\infty}$ is the reduced gravity.

### 2.4.1 Neutrally buoyant plumes

First, the behaviour of neutrally buoyant plumes is studied. The fluctuating plume model, proposed by Gifford (1959), describes the motion of the plume as a combination of bulk meandering and relative diffusion from the plume's centre, as illustrated in figure 2.7. This model allows for representing fluctuating quantities superimposed on the mean plume. However, it is an idealised model limited to isolated two-dimensional plumes in isotropic turbulence. Since its introduction, efforts have been made to enhance and modify the model. For instance, Luhar et al. (2000) updated the model to incorporate plumes in a convective boundary layer.

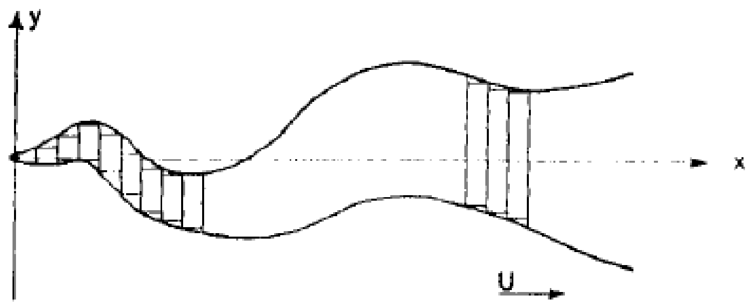


FIGURE 2.7: Fluctuating plume model with spreading disk element. Figure adapted from Gifford (1959).

A more recent model summarised and depicted in figure 2.8 by Cassiani et al. (2020), considers the relative sizes of eddies and the plume. Close to the source, the plume is small compared to the eddies, resulting in plume meandering. As the plume progresses downstream, it grows, and the eddies become smaller than the plume width. Consequently, the eddies no longer induce meandering but instead contribute to the relative diffusion of concentration within the plume.

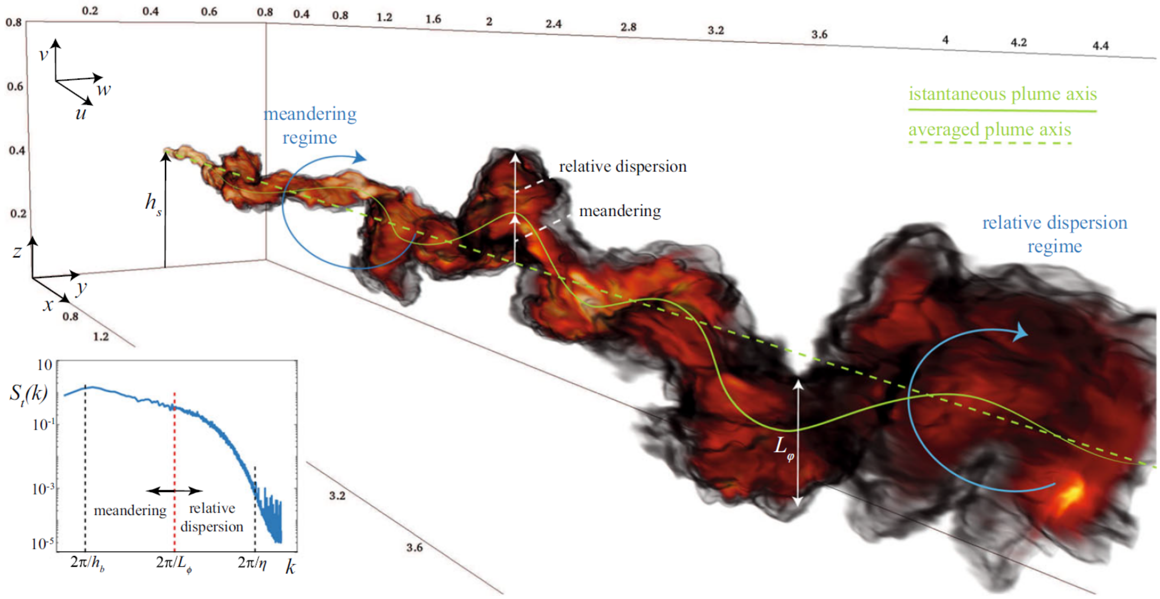


FIGURE 2.8: Plume dispersion regimes. The blue arc represents eddies of the same size. Close to the source, the plume meanders due to the presence of large eddies compared to the plume size, $L_\phi$. Downstream, on the right side of the figure, eddies contribute to the relative diffusion inside the plume. Figure adapted from Cassiani et al. (2020). Please note that in this thesis, the labels for $v$ and $w$ are interchanged compared to the figure.

#### 2.4.1.1 Mean concentration profile

Fackrell and Robins (1982) were the first to systematically study the difference between the vertical profile of a ground-level source (GLS) and an elevated source (ES) experimentally (Fackrell and Robins 1982). The comparison of a GLS and ES is illustrated in figure 2.9.

The mean vertical profile of an ES plume can be theoretically deduced from the simplified Reynolds-averaged transport equation 2.9, assuming a constant eddy diffusivity in the vertical direction (Wyngaard 2013). The Gaussian equation describes the mean concentration profile as follows:

$$C(z) = C_{\max} \exp\left[-\ln 2\left(\frac{z - z_{\mathrm{CL}}}{\delta_z}\right)^2\right] \tag{2.24}$$

In this equation, $C_{\max}$ represents the maximum concentration, subscript CL denotes the plume centreline, and $\delta_z$ represents the plume half-width. Numerous experimental studies have shown good agreement with the Gaussian model (Fackrell and Robins 1982; Yee and Biltoft 2004; Nironi et al. 2015; Talluru et al. 2017; Young et al. 2021).

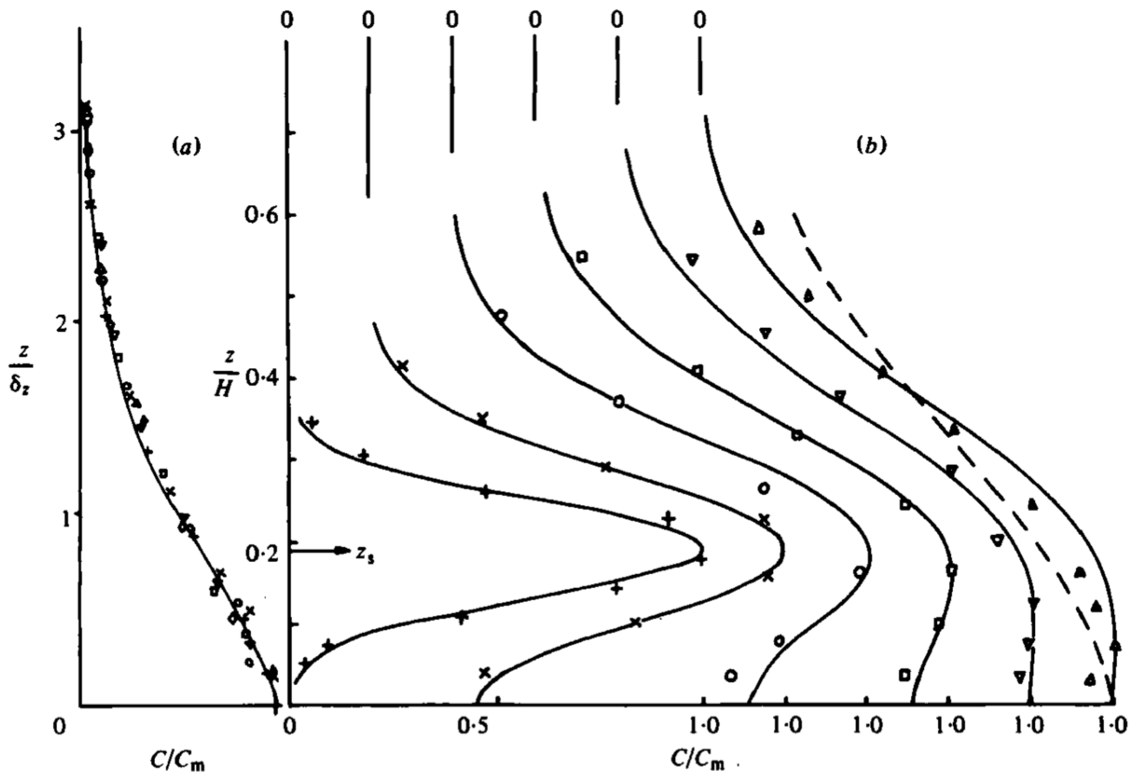


FIGURE 2.9: Downstream development of vertical mean concentration profile for (*a*) a ground-level source and (*b*) an elevated source. Figure adapted from Fackrell and Robins (1982).

The vertical concentration profile of a GLS plume is self-preserving and can be described by either a half-Gaussian or an exponential equation. The exponential equation is represented as follows:

$$C(z) = C_{\text{max}} \exp\left[-\ln 2\left(\frac{x}{\delta_z}\right)^b\right] \tag{2.25}$$

Here $b$ is a fitted constant, between 1.5 and 2 depending on the background flow (Hunt and Weber 1979; Fackrell and Robins 1982).

In the case of an ES plume affected by the presence of the ground, a Gaussian model is not suitable for accurately describing the vertical profile. Instead, a reflected Gaussian distribution is more appropriate to account for the influence of the ground on the plume's vertical spread. The reflected Gaussian equation is given by:

$$C(z) = C(z) = C_{\text{max}}\left[\exp\left(-\ln 2\frac{(z+z_{\text{CL}})^2}{\delta_z^2}\right) + \exp\left(-\ln 2\frac{(z-z_{\text{CL}})^2}{\delta_z^2}\right)\right] \tag{2.26}$$

As the plume propagates downstream, the vertical mean concentration profile of an ES gradually transitions to that of a GLS (Fackrell and Robins 1982; Nironi et al. 2015; Talluru et al. 2017).

The plume half-width, $\delta_z$, is defined as the height difference between the locations of $C_{\max}$ and $C_{\max}/2$. Under homogeneous turbulence, the plume width grows linearly with downstream distance in the near field and then follows an $x^{1/2}$ power law (Wyngaard 2013). In the context of the turbulent boundary layer (TBL), different growth rates have been observed, with the exponent ranging from 0.61 to 0.75 (Robins 1978; Fackrell and Robins 1982).

In isotropic turbulence, $C_{\max}$ is expected to vary as $x^n$ (Lavertu and Mydlarski 2005). However, experimental data indicate that the power law decay only applies to GLS plumes in a turbulent boundary layer (Robins 1978; Fackrell and Robins 1982). The power law relation between $C_{\max}$ and downstream distance for ground-level sources have been observed, although no specific fitting parameter $n$ was provided (Fackrell and Robins 1982). In the case of elevated sources, a power law does not provide a good fit (Fackrell and Robins 1982; Nironi et al. 2015; Lavertu and Mydlarski 2005).

Plume dispersion in various background flows has been studied, including grid-generated turbulence (Stapountzis et al. 1986), convective boundary layer (Weil et al. 2002), stable boundary layer (Robins et al. 2001b), turbulent channel flow (Lavertu and Mydlarski 2005), and canopy boundary layer (Coppin et al. 1986; Legg et al. 1986). For plumes over a canopy layer or in a channel flow, the mean vertical profile is not Gaussian and exhibits a reversal above and below the source in the near-field region. In addition to point sources, various source geometries have been investigated. Line sources, such as line thermal sources, have been studied in several papers (Legg et al. 1986; Lavertu and Mydlarski 2005). Their results were compared to research on line sources by Legg et al. (1986), revealing that the eddy diffusivity for heat depends on source geometry and turbulent properties. The interference between two or multiple line sources has also been examined (Warhaft 1984). It was concluded that the thermal wakes of each line source interact and merge downstream, and the line spacing and integral length scale strongly influence the onset of interaction.

#### 2.4.1.2 Standard deviation and higher moments of concentration

The standard deviation or root-mean-square (RMS) of concentration, $\sigma_c$, quantifies the magnitude of concentration fluctuations. The evolution of $\sigma_c$ follows a similar pattern as that of $C$. The vertical profile of $\sigma_c$ for GLS plumes is self-preserving and exhibits a half-Gaussian shape. In contrast, the profile for ES plumes is nearly Gaussian near the source and gradually transitions towards the profile of a GLS further downstream (Fackrell and Robins 1982). Since the distribution of $\sigma_c$ is also Gaussian, three parameters are required to describe the profile fully: the peak value, $\sigma_{c,\,\mathrm{max}}$; the half-width, $\delta_{z,\sigma}$; and the centreline height, $z_{\mathrm{CL},\,\sigma}$. This is analogous to defining the $C$ profile. The half-width calculated from the $\sigma_c$ profile, denoted as $\delta_{z,\sigma}$, increases as $Ax^{m_\sigma}$ (Lavertu and Mydlarski 2005). Interestingly, it is observed that $\delta_{z,\sigma}$ is larger than $\delta_z$ (Talluru et al. 2017).

Under homogeneous turbulence, the standard deviation profile exhibits two distinct phases as it progresses downstream: initially double-peaked and then transitioning to single-peaked (Warhaft 1984; Lavertu and Mydlarski 2005). This phenomenon is associated with the "bulk flapping of the wake". However, Sawford and Tivendale (1992) noted that the double peaks reappear at even greater downstream distances. They attributed the presence of double peaks to the relative size of the eddies with the scale at which the spanwise temperature gradient undergoes rapid changes. Notably, this double peak phenomenon in the standard deviation profiles is absent in high-aspect-ratio turbulent channel flow (Lavertu and Mydlarski 2005).

Experimental data have demonstrated that the concentration downstream of a ground-level or lower source exhibits less intense fluctuations than an elevated source, primarily due to the smaller scale of turbulent events near the wall (Fackrell and Robins 1982; Nironi et al. 2015). Consequently, $\sigma_c$ for an elevated source is more influenced by the source size than a ground-level source (Fackrell and Robins 1982). Moreover, both in the transverse and vertical directions, concentration measurements for a larger source exhibit less stability in the near field than a smaller source, and this effect gradually diminishes in the far field (Nironi et al. 2015).

The third and fourth moments of velocity, known as skewness, $Sk$, and kurtosis, $Ku$, respectively, play an important role in characterising turbulence. It has been shown by Chatwin and Sullivan (1990) and Nironi (2013) that the spanwise profiles of $Sk$ and $Ku$ exhibit self-similarity. Furthermore, there exists a relationship between $Sk$ and $Ku$, given by:

$$Ku = A(Sk^2) + B, \tag{2.27}$$

where the constants $A$ and $B$ depend on the specific flow, spatial, and temporal conditions and can be determined empirically (Schopflocher and Sullivan 2005). Equation 2.27 holds the potential for predicting probability density functions.

#### 2.4.1.3 Probability density function of concentration

The spread of a plume in a turbulent boundary layer has been extensively studied. However, due to the complexity of the turbulent flow, the prediction of the instantaneous concentration downstream of the source cannot be realised. Hence, one has to rely on statistics to *predict* the occurrence of instantaneous events with desired certainty, of which high-concentration events are of practical interest. The approach is to use the PDFs of concentration at different points in space as they contain information on all moments and the probability of occurrence of extreme events.

Chatwin and Sullivan (1990) highlight the scaling law between the mean concentration and the RMS of the concentration from both theory and experimental data for uniform source. They extend their theory to the similarity of the ratio of higher-order consecutive moments. However, their predictions are unsuitable for near fields where the concentration fluctuations are highly dependent on the source condition. Their work is complemented by that of Sawford and Sullivan (1995) for near field and background flow of homogeneous turbulence. Since the PDF includes information about all moments, these studies suggest the possibility of self-similarity of concentration PDFs. Various distributions are fitted to concentration data in past studies, including but not limited to Weibull, beta, gamma, log-normal, and Gaussian distributions, summarised by Cassiani et al. (2020, see table 2). The expressions for the PDFs are listed in table 2.2. Among the listed distributions, Gaussian, beta, log-normal, and gamma

| | |
|---|---|
| Gaussian | $f(x) = \frac{1}{\sigma\sqrt{2\pi}} \exp\left[-\frac{1}{2}\left(\frac{x-\mu}{\sigma}\right)^2\right]$ |
| log-normal | $f(x) = \frac{1}{x\sigma\sqrt{2\pi}} \exp\left[-\frac{1}{2}\left(\frac{\ln x-\mu}{\sigma}\right)^2\right]$ |
| beta | $f(x) = \frac{x^{\alpha-1}(1-x)^{\beta-1}}{B(\alpha,\beta)}$, where $B(\alpha,\beta) = \frac{\Gamma(\alpha)\Gamma(\beta)}{\Gamma(\alpha+\beta)}$ |
| gamma | $f(x) = \frac{1}{\Gamma(k)\theta^k} x^{k-1} \exp\left(-\frac{x}{\theta}\right)$ |
| Weibull | $f(x) = \frac{k}{\lambda}\left(\frac{x}{\lambda}\right)^{k-1} \exp\left[-\left(\frac{x}{\lambda}\right)^k\right]$ |
| Generalised Pareto Distribution (GPD) | $f(x) = \frac{1}{\sigma}\left(1+\xi\frac{x-\mu}{\sigma}\right)^{-1/\xi+1}$ |

TABLE 2.2: The probability density functions proposed in past literature to describe the instantaneous concentration. Note that the $x$ in this table is a random variable, different from the $x$ defined as streamwise location in the rest of this thesis.

distributions belong to the exponential family. Weibull distribution can have an exponential tail when the parameter $k$ is fixed. Most researchers have found agreement with the gamma distribution with their data (Nironi et al. 2015; Efthimiou et al. 2016; Oettl and Ferrero 2017), while Yee et al. (1993) concludes that a Weibull distribution describes the concentration PDFs better. Hence, there is no broad agreement on a representative functional form. It is to be noted here that these studies attempt to fit the full-signal PDF, which includes near-zero and non-zero concentrations. However, the instantaneous concentration of scalar, particularly in a meandering plume, is intermittent, *i.e.* the concentration is zero for a certain duration and then peaks to values much greater than the mean concentration at other times. Such concentration behaviour is not suitably represented by a gamma, log-normal or Weibull distribution, which prescribes $p(\tilde{C}=0)=0$. Here $\tilde{C}$ is the instantaneous concentration, and $p$ is the probability density function. Therefore when fitting the full range of the concentration PDF, one needs to consider both the possible peak at $\tilde{C}=0$ due to intermittency and the overall shape at $\tilde{C}>0$. Nironi et al. (2015) verifies the effect of intermittency, $\pi$, by plotting the PDF for signals with various intermittency. Hypothetically, the PDF of a uniform source with no molecular diffusion is,

$$p(\tilde{C};\mathbf{x},t) = \pi(\mathbf{x},t)\delta(\tilde{C}-\tilde{C}_1) + (1-\pi(\mathbf{x},t))\,\delta(\tilde{C}), \tag{2.28}$$

where $\tilde{C}_1$ is the source concentration (O'Brien 1978; Chatwin and Sullivan 1990). Here the intermittency is accounted for by the Dirac-delta function at $\tilde{C}=0$. When molecular diffusion is present, the first term becomes a probability function.

$$p(\tilde{C};\mathbf{x},t) = \pi(\mathbf{x},t) f(\tilde{C};\mathbf{x},t) + (1-\pi(\mathbf{x},t))\,\delta(\tilde{C}). \tag{2.29}$$

Here $f$ is the PDF (similar to equation 14 by Chatwin and Sullivan (1989)). In a follow-up study, Yee and Chan (1997) discusses fitting a shifted and clipped-gamma distribution to the full signal with assumptions that simplify the role of molecular diffusion. By examining the exceedance probability distribution of the data and the model, the higher concentrations are found to be under-predicted.

The tail of PDFs is of interest because the high concentration of pollutants is more concerning, whereas low concentration measurements are affected by the instrumentation (Cassiani et al. 2020). High concentration statistics, e.g. 90$^{\text{th}}$ and 98$^{\text{th}}$ percentile, are used in regulations to quantify odour impact (e.g. Oettl and Ferrero 2017; Invernizzi et al. 2020). The challenge of modelling the tail of concentration is compounded by the unavailability of reliable data as long sampling times are needed. Only a few studies focus on fitting certain distributions to the tail of the PDFs, although the extent of fits varies in each study. Schopflocher (2001) and Mole et al. (2008) used Extreme Value Theory to investigate the 'goodness' of fit of a Generalized Pareto Distribution (GPD) for concentration larger than the local mean. The variation of the shape parameter in the GPD cross-plume is found to be relatively constant in Schopflocher (2001). Efthimiou et al. (2016) used a gamma distribution to fit the 75$^{\text{th}}$ to 99$^{\text{th}}$ percentile of the concentration data, whereas Oettl and Ferrero (2017) found that a Weibull distribution describes the PDF well when the concentration is higher than the 90$^{\text{th}}$ percentile. Among these three fits, Weibull and gamma distributions have an exponential tail, while GPD does not.

#### 2.4.1.4 Scalar fluxes

Although the mean flow in the spanwise and wall-normal directions is zero, the instantaneous fluctuations of velocities in these directions are not zero. These velocity fluctuations play a significant role in scalar mixing in those directions. Therefore, studying the flux terms, $\overline{u_i c}$, in equation 2.6 is crucial for understanding the relative amount of scalar transported by different motions. However, due to their second-order statistical nature and the need for accurate measurements, there are limited experimental studies that have systematically investigated these fluxes.

Fackrell and Robins (1982) provided insights into the downstream development of vertical scalar fluxes, $\overline{wc}$. For GLS, whose mean profile is Gaussian, the shape of $\overline{wc}$ remains consistent at different downstream distances. In the case of ES, $\overline{wc}$ is positive above the centreline and negative below near the source. Further downstream, the behaviour of $\overline{wc}$ for ES transitions to that of a GLS (Fackrell and Robins 1982; Legg et al. 1986). Fackrell and Robins (1982) proposed a spanwise eddy diffusivity that depends only on $x$, as the lateral variation of fluxes $\overline{wc}$ is similar to that of mean concentration. The spanwise velocity fluctuations, $\overline{uc}$, exhibit opposite signs to $\overline{wc}$, but their behaviour is similar (Legg et al. 1986; Karnik and Tavoularis 1989; Lavertu and Mydlarski 2005). Warhaft (1976) concluded that the "scalar flux should be a function of the initial relative scale sizes of the velocity and temperature fields", based on a study of temperature fluctuations in grid-generated turbulence. However, Pope (1998) argued that scalar flux depends entirely on the fluid-particle motion at high $Re$. Vanderwel and Tavoularis (2016) used conditional analysis to demonstrate a strong correlation between events of scalar flux and Reynolds shear stress. This highlights the importance of understanding scalar transport by known coherent features.

### 2.4.2 Negatively and positively buoyant plumes

In the 1970s to 1990s, several studies aimed to develop engineering models for practical purposes, such as predicting plume centreline and ground-level concentrations. However, during that period, measurement techniques and computational devices were not as prevalent, resulting in limited variables being discussed in experimental studies. Although significant advancements have been made in measurement and computational techniques over the past 20 years, the overall study of positively and negatively buoyant plumes has remained relatively stagnant. Due to the separate nature of studies conducted on positively and negatively buoyant plumes, we will discuss them separately in the following sections.

#### 2.4.2.1 Positively buoyant plume

Csanady (1973) discusses the four phases of a positively buoyant plume as shown in figure 2.10. The jet phase is relevant when the plume is released vertically, and the effect of initial vertical momentum dissipates within a few chimney diameters. The last two phases, the breakup phase and the final phase, are analogous to the dispersion regime model for the neutral plume discussed in section 2.4.1. The phase most relevant for buoyant plumes is the second phase – the thermal phase. A common terminology used in buoyant plume dispersion is the bent-over plume, which refers to the first two phases. A classic model was developed

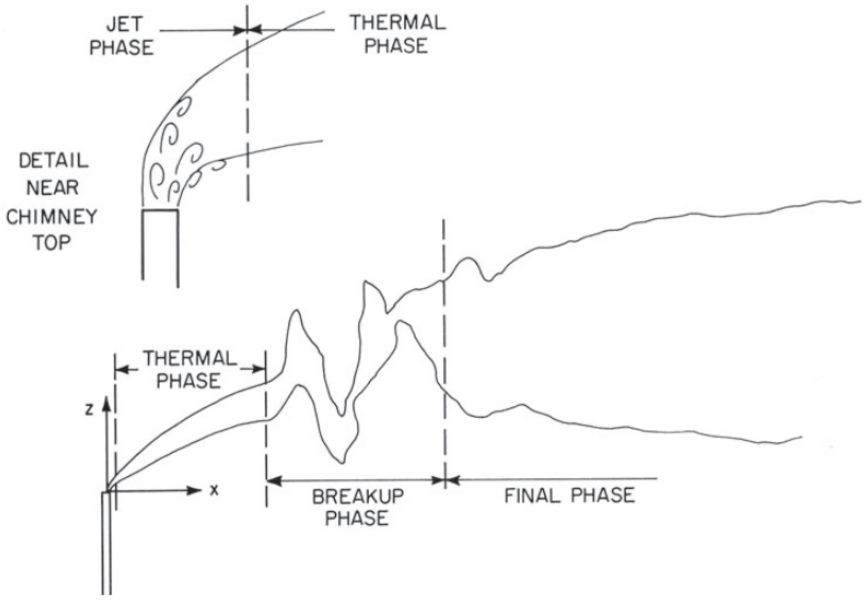


FIGURE 2.10: Schematic illustration of different phases of chimney plume behaviour. Adapted from Csanady (1973, figure 6.4).

by Briggs (1969) to predict the rise of the mean plume under neutral and stratified conditions. The plume rise follows a 2/3 law.

$$\Delta h = 1.6 F^{1/3} u_s^{-1} x^{2/3} \tag{2.30}$$

Here, $\Delta h$ represents the plume rise, $F$ is the buoyancy flux, and $u_s$ is the source speed. However, this equation is only applicable up to a distance at which atmospheric turbulence begins to dominate entrainment. This model has been validated by experimental data (Briggs 1969; Hewett et al. 1971; Hoult and Weil 1972) as well as field data (Lareau and Clements

2017). Hewett et al. (1971) also demonstrated that this law is independent of Reynolds number ($Re$) for stack exits with $Re > 150$. However, this model does not provide any information regarding plume width or higher moments of plume statistics, making it a primitive approach.

Hoult and Weil (1972) assumed linear relationships between the vertical and tangential velocity components and the entrainment rate, finding constant coefficients for fully turbulent flow and small density differences based on experimental data. Additionally, based on experimental and field data, it has been observed that the mean profiles of light plumes follow a Gaussian distribution (Stapountzis et al. 1986; Lareau and Clements 2017).

A physical explanation of concentration fluctuation was provided by Stapountzis et al. (1986, figure 19). According to their explanation, the initially smooth appearance of a hot plume is gradually transformed as it is transported downstream by the turbulent flow. The plume develops internal structure or variations, resulting in a patchier appearance. This internal structure persists and grows as the plume expands, eventually reaching a self-similar state. In this state, temperature fluctuations within the plume maintain the observed internal structure. These three phases vaguely correspond to the last three phases depicted in figure 2.10.

It should be noted that there are other studies that involve the use of line thermal sources. However, the excess temperature in these cases is so low that the scalar can be considered passive. Therefore, these studies, such as (Warhaft 1984; Stapountzis et al. 1986; Legg et al. 1986; Lavertu and Mydlarski 2005; Lepore and Mydlarski 2011), are not included in this discussion.

#### 2.4.2.2 Negatively buoyant plume

For heavy gas, more models were developed since it is more prone to produce higher concentrations at the ground level/pedestrian level. Hanna et al. (1993) reviewed 15 models for dense gas dispersion. While all models predict relatively well for passive release, only four of the models (AIRTOX, HGSYSTEM, PHAST and SLAB) predict more accurately for dense gas and exhibit a tendency to overestimate the lateral plume spread while underestimating the vertical plume spread, typically by approximately twice the actual values.

One of the earliest measurements of dense plumes in a TBL was conducted by Hoot et al. (1973), where the density ratio varied from 1 to 3. Their analysis focused on ground-level concentration decay with downstream distance and plume width. The experimental data revealed that the lateral mean profile follows a Gaussian distribution, although no explicit vertical profile was plotted. However, subsequent experimental studies by Roberts et al. (1994) and Robins et al. (2001a) explicitly demonstrated that mean vertical profiles of dense plumes are Gaussian.

In the early 2000s, there was renewed interest in studying the dispersion of dense plumes. Briggs et al. (2001) compared four wind tunnel studies conducted in different facilities that investigated the downstream development of negatively buoyant plumes released at ground level over roughness elements (Robins et al. 2001a; Robins et al. 2001b; Snyder 2001; Havens et al. 2001). This collaborative effort led to formulating entrainment velocity as a function of friction velocity at different source Richardson numbers. Some physical explanations were also provided. At high Richardson numbers (large density ratio), the plume exhibited a layered structure with a sharp upper interface and an intermittent turbulent motion was observed below the interface (Robins et al. 2001a; Snyder 2001). On the other hand, for fully turbulent plumes, entrainment velocities were found to be proportional to the inverse decay of ground-level concentration (Snyder 2001). Furthermore, the spreading of dense gas due to gravity was observed in the upstream direction from the source (Snyder 2001).

#### 2.4.2.3 Buoyant plumes over roughness

While there have been numerous experimental studies conducted on plume dispersion over rough terrain, the majority of them have primarily concentrated on passive scalar dispersion (Coppin et al. 1986; Legg et al. 1986; Davidson et al. 1995; Salizzoni et al. 2009; Carpentieri et al. 2012; Mo and Liu 2018). Experimental studies on buoyant plumes over roughness are summarised in the table 2.3. These studies exclusively focused on a single buoyancy scenario, either positive or negative. Moreover, the roughness configurations employed in each study differed, resulting in distinct wind profiles. Notably, only the initial two studies incorporated roughness elements characterised by repeating patterns. However, it is essential to note that in these first two studies, the height of the roughness elements relative to the boundary layer thickness remained relatively small, thereby placing the flow outside the fully rough regime (as indicated in Table 2.1). It is worth mentioning that none of these three studies explored the dispersion of an elevated plume released within a canopy. The relevant studies are already discussed in the previous sections and hence will not be repeated here. This section merely highlights the limited number of studies that incorporated roughness and buoyancy of plume dispersion.

| Reference | Source geometry | Source height | Roughness | Buoyancy |
|---|---|---|---|---|
| Roberts et al. (1994) | 0.1 m-diameter disk | GLS | Staggered 9-mm roughness of 4 different cross-sections | $\rho_s/\rho_0 = 1$, 1.4, and 5.74 |
| Briggs et al. (2001) | Line | GLS | Staggered rectangular baffles (max 5 cm height) | $\rho_s/\rho_0 \approx 1.57$ ($CO_2$) |
| Pournazeri et al. (2012) | Point | ES | Specific geometry of a real factory | $\rho_s/\rho_0 = 0.96$ and 0.98 |

TABLE 2.3: Experimental studies on buoyant plume dispersion over roughness. Note that experiments with passive scalar or in smooth-wall boundary layers are excluded.

CHAPTER 3

# Experiments for buoyant plumes

---

This chapter presents an overview of the buoyant plume experiments and details of the measurement setup used. The dispersion of plumes of varying densities in a turbulent boundary layer is simulated in a controlled laboratory environment. To the author's knowledge, no past experiments have compared heavy, neutral, and light plumes using the same experimental setup. Hence the experiments in this thesis are designed for systematic comparison between these three cases. The experiments reported in this chapter evolved from those conducted by Talluru et al. (2017), where neutrally buoyant plumes are released in a wind tunnel, and measurements of velocity and concentration are acquired downstream using a single hotwire (HW) and a Photo-Ionisation Detector (PID). In this study, the density of the plume being released is varied, and the tracer gas is released over three different surfaces: (i) smooth and (ii & iii)cube roughness with different streamwise spacings. Furthermore, an $\times$-wire is used to simultaneously measure the streamwise and vertical velocity components in the turbulent boundary layer.

Section 3.1 of this chapter comprehensively describes the specifications of the wind tunnel and the roughness types. The release mechanism and the initial flow conditions of the plume are detailed in section 3.2. The following two sections present the mechanism and calibration procedure of the sensors for velocity and concentration measurements. The background flow generated using the setup described is showcased in section 3.5.

## 3.1 Test facility

The experiments are conducted in the Boundary Layer Wind Tunnel (BLWT) at the University of Sydney. It is a closed-loop wind tunnel with a test section of $2\times2.5$ m$^2$, as illustrated in figure 3.1. There is a mild favourable pressure gradient of approximately 3% increase in the freestream over 12 m of flow development length. Full details of the wind tunnel are available in Talluru et al. (2017). Figure 3.2 illustrates the schematic of the experimental setup in the wind tunnel, and figure 3.3 is a photo of the releasing nozzle and the sensors used for measuring velocity and concentration of the tracer gas. The source height ($S_z$) and the source distance ($S_x$) are also schematically shown in 3.2.

The freestream velocity, $U_\infty$, is set to 2.5 m/s. The incoming turbulence intensity in the freestream is less than 0.4%. Low $U_\infty$ is adopted in this study because, at higher wind speeds, the advection of the plume is significantly stronger to observe buoyancy effects. Hence, no effect of density difference can be detected at a reasonable downstream distance. This is also the lowest $U_\infty$ achievable in the wind tunnel that can generate a flow with stationary turbulence statistics. At this freestream velocity, the unperturbed boundary layer is thin in the wind tunnel with timber walls along the development section of the tunnel. Therefore, LEGO baseboards are used at the start of the development section (approximately 12 m upstream of the measurement station) to introduce additional turbulence in the flow and increase the boundary layer thickness, $\delta$. This setup is schematically shown on the left side of figures 3.2 and 3.4. The LEGO baseboards consist of cylindrical studs, 4.8 mm in diameter and 1.6 mm in height, spaced 8 mm apart in a grid pattern. The LEGO baseboards occupy a streamwise distance of 1.05 m and span the entire width of the wind tunnel.

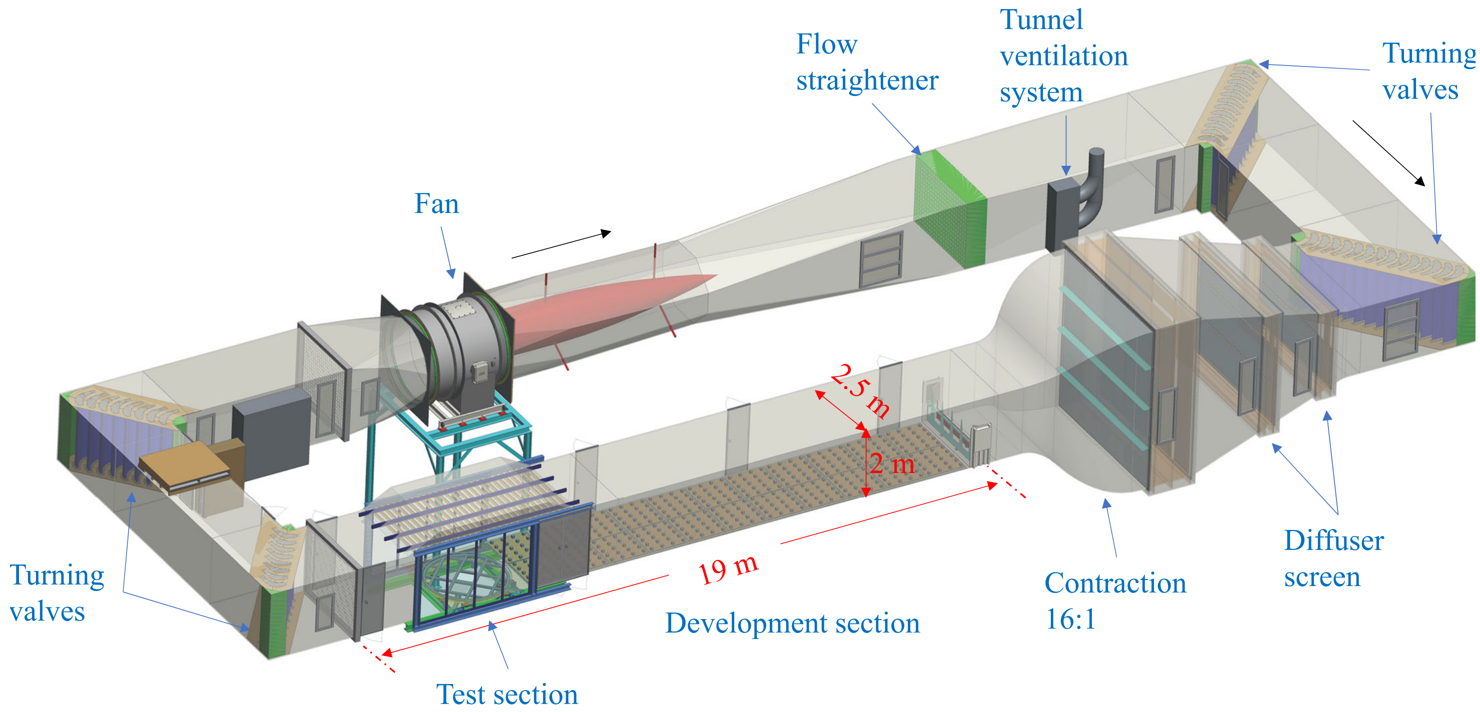


FIGURE 3.1: Schematics of the Boundary Layer Wind Tunnel at the School of Civil Engineering, the University of Sydney.

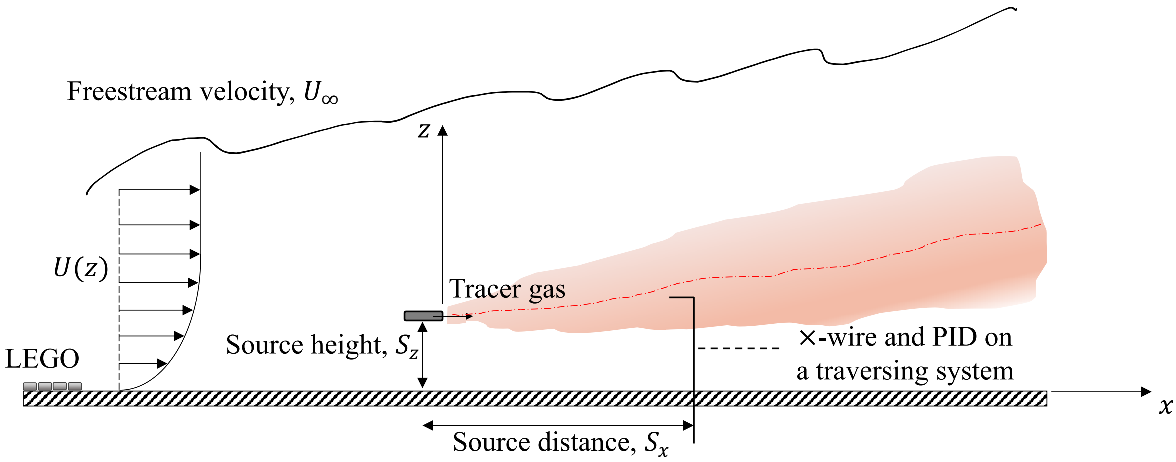


FIGURE 3.2: Schematic of the experimental setup.

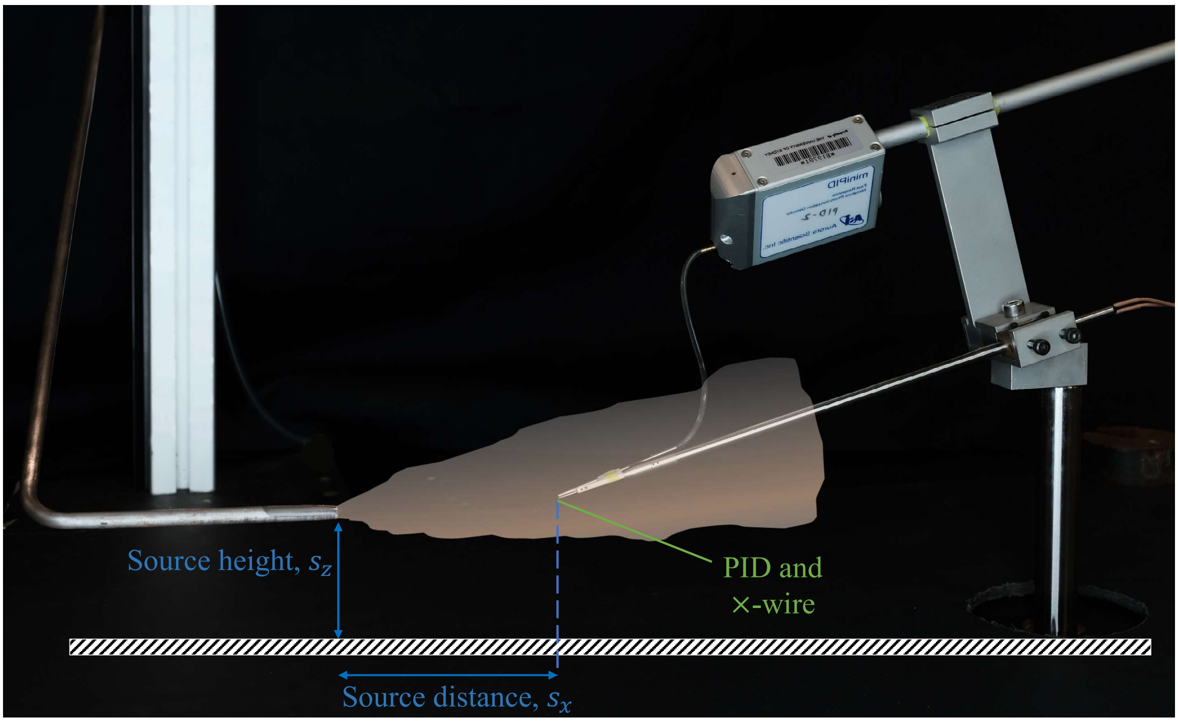


FIGURE 3.3: Photo of the experimental setup.

The second series of experiments focus on buoyant plume dispersion over different types of roughness, resembling more realistically the dispersion of pollutants over an urban landscape. The roughness elements introduce more turbulence into the flow field. All the roughness elements are wooden cubes with a dimension, $h$, of 40 mm. The layout of the cubes is staggered, and the lateral spacing between the blocks is always $h$. The difference between

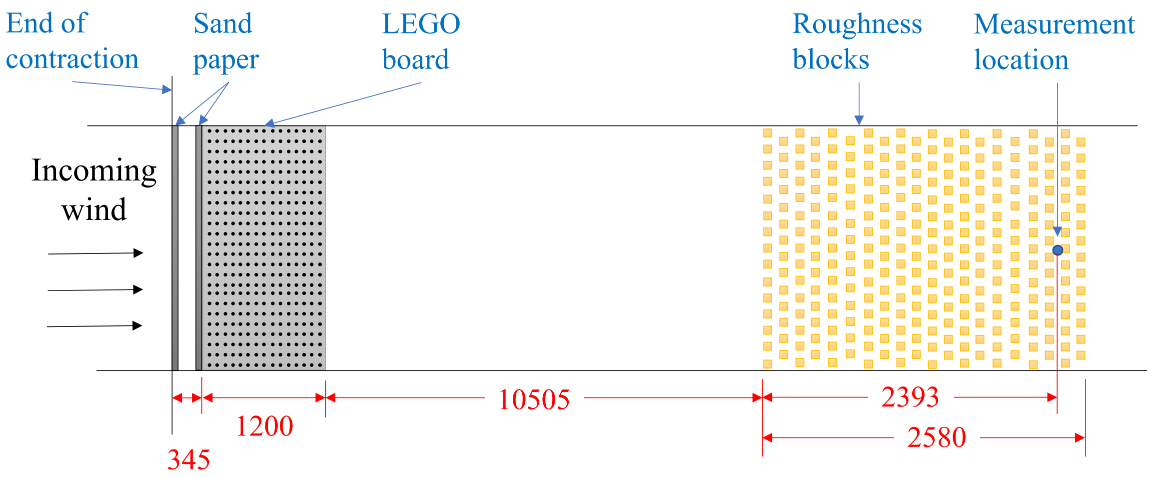


FIGURE 3.4: Location of the experimental setup from the beginning of the development section. All numbers are in mm.

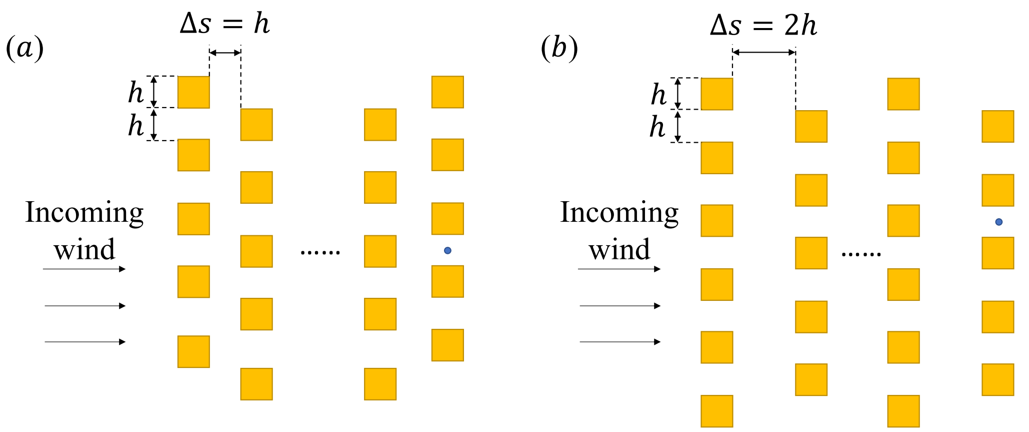


FIGURE 3.5: Layout of selected roughness elements with downstream spacing between rows of ($a$) $h$ ($b$) $2h$. The blue dots are measurement locations.

the two patterns is the downstream spacing between each row, $\Delta s$, one being $h$ and the other being $2h$, as shown in figure 3.5($a$) and 3.5($b$), respectively. The two downstream spacings represent both $k$- and $d-$ type roughness discussed in section 2.3.2. The spanwise extent of the blocks for both patterns in the wind tunnel is identical and is labelled in figure 3.4.

Three source heights, $S_z$, are tested for the smooth-wall setup (no wooden cubes): 0, $0.16\delta$, $0.31\delta$. Hereafter $S_z = 0$ is referred to as a Ground Level Source (GLS), and $S_z/\delta$ = 0.16 and

0.31 are referred to as Elevated Sources (ESs). The velocity and concentration measurements are collected at three downstream distances from the source release, $S_x/\delta$ =1, 2 and 4, where $\delta$ is the corresponding thickness of a smooth-wall boundary layer. For the roughwall boundary layer, the same three source heights are tested ($S_z/h$ =0, 1, and 2). In dimensional units, the elevated sources are released at $S_z = 40$ mm and 80 mm, which are integer multiples of the roughness height. The measurements over roughness are only acquired at $S_x/\delta = 1$ and 2 as it is found that the density of the plume beyond $2\delta$ is the same as the ambient flow. The data are acquired at a sampling frequency of 4096 Hz for a duration of 300 s for all measurement points.

## 3.2 Tracer gas

The gas mixture released from the discharge nozzle emulating a point source has a different density than the ambient flow. The mixture consists of 98.5% stable gas and 1.5% tracer gas (iso-butylene). The purpose of the stable gases is to adjust the overall density of the released mixture, $\rho_s$. Helium ($\rho_{\mathrm{He}}$), Nitrogen ($\rho_{\mathrm{N}}$), or Argon ($\rho_{\mathrm{Ar}}$) are used as stable gases for positively-buoyant, neutral, and negatively-buoyant plumes, respectively. The iso-butylene in the gas mixture is detected by the concentration sensor (mini-PID 200B, Aurora Scientific). The mass flow rate of the tracer gas is precisely controlled and monitored by a mass flow controller (Alicat Scientific MCS Mass Flow Controller). This arrangement is shown in figure 3.6. The tracer mix discharges from a round tube with an internal diameter of 4.5 mm ($0.015\delta$) at the local wind speed. The release nozzle is an L-shaped metal tube that is internally smooth, as shown in figure 3.3. The short side is 100 mm in length and aligned with the flow. The long side is diagonally supported from a stand approximately 400 mm away from the point of release and has minimal interference on the flow. A continuous metal tube is chosen for its rigidity and has no vibration under the background flow.

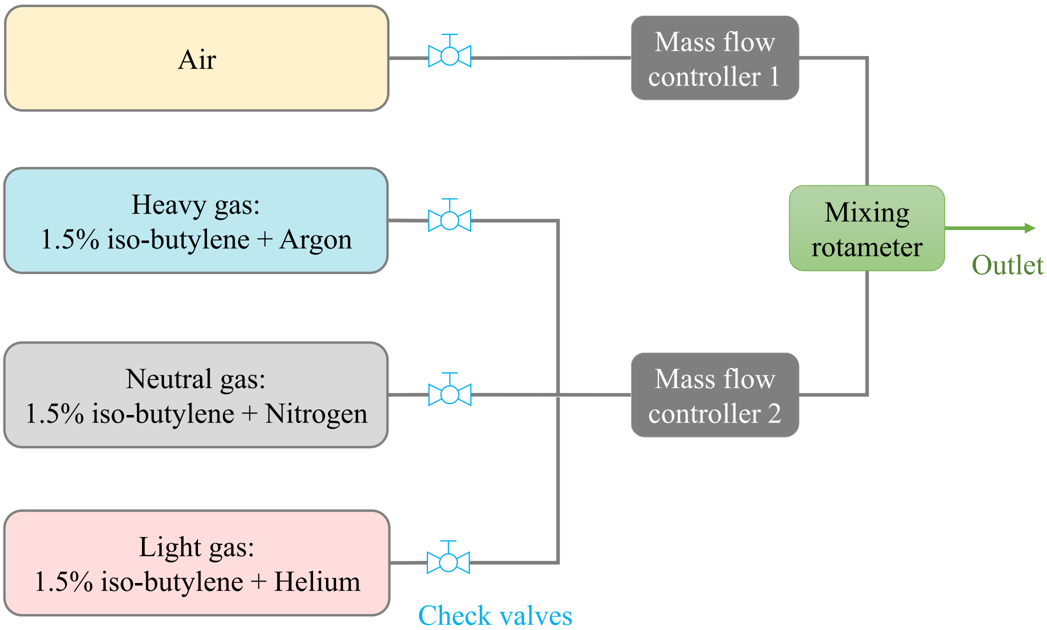


FIGURE 3.6: Schematic of the pneumatic system.

## 3.3 $\times$-wire

An $\times$-wire (also known as cross-wire) measures the streamwise and vertical velocity components. It is a straight miniature $\times$-wire probe with gold-plated tungsten wire (55P61) supplied by Dantec Dynamics. The diameter of the wire is 5 $\mu$m, and the length of the wire is 1.25 mm. This leads to a length-to-diameter ratio of larger than 200, as recommended by Ligrani and Bradshaw (1987), Hutchins et al. (2009), and others. The distance between two needles, $\Delta s_y$, is approximately 1 mm. In wall-normal units $\Delta s_y^+ \approx 6.4$. This is also smaller than the recommended range $\Delta s_y^+ < 20$ according to Hutchins et al. (2009), though it is worth noting that this is suggested for $Re_\tau \gtrsim 3000$. Baidya et al. (2019b) discussed the spatial averaging effects on second-order statistics by $\times$-wires close to the wall. A larger sensor dimension causes a reduction in $\overline{u^2}$ and an increase in $\overline{w^2}$. However, the large difference between the actual data and the measured second-order statistics is mainly in the region of $z^+ < 50$, see Baidya et al. (2019b, figure 10 in). Only a few measurement points close to the ground in this study are within this range, and hence the effects are minimal in the current study. The measurements within $z^+ = 50$ are excluded in the data analysis for higher-order statistics, e.g. scalar fluxes. Due to the size of the $\times$-wire holder, the $\times$-wire probe is 8 mm from the wall

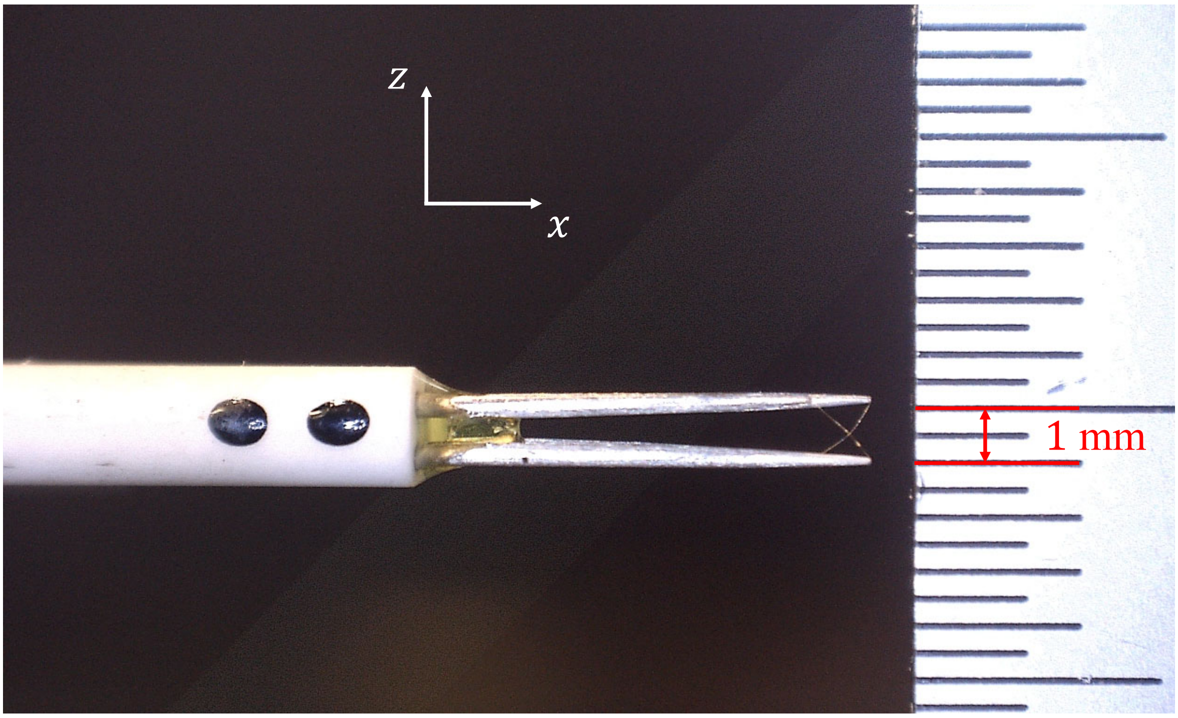


FIGURE 3.7: Side view of an $\times$-wire. The two Tungsten wires show $\times$ shape.

when held horizontally. To measure the velocity closer to the wall, the $\times$-wire is held at an angle of $15°$ from the horizontal with a compensation applied in the calibration. This allows velocity measurements very close to the wall, i.e., above 1 mm from the wall. The overheat ratio of the hotwires is 0.8.

### 3.3.1 Calibration

The calibration process establishes the relationship between the two voltage outputs, $E_1$ and $E_2$, from the $\times$-wire, and the velocity components, $u_1$ and $u_2$,

$$u_1 = f_1(E_1, E_2) \text{ and } u_2 = f_2(E_1, E_2). \tag{3.1}$$

The calibration procedure is similar to that described in Baidya (2016, section 4.3 in). The $\times$-wire is calibrated when both the direction and the speed of the incoming jet are varied. The calibration jet is generated by the StreamLine Pro Automatic Calibrator, whereas the direction of the probe with respect to the jet axis is changed using an in-house rotary table.

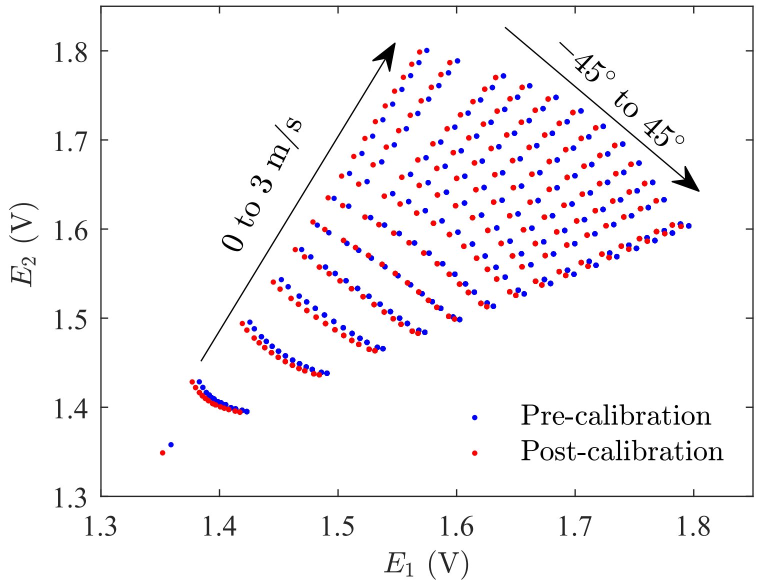


FIGURE 3.8: Comparison of pre- and post-calibration map of an ×-wire.

The jet speed ranges from 0.25 to 3 m/s, and the angle varies between ±45 °. Furthermore, because $f_1$ and $f_2$ are cubic equations, more calibration points are specified at smaller angles and lower jet speeds. Previous research shows that a look-up table approach is suitable for flows less than 6 m/s (Burattini and Antonia 2005). When applying the calibration function to the raw data, the velocity outputs are interpolated using a bi-linear function when the angle between the incoming velocity and the wire is less than 30°. The purpose is to minimise errors from fitting a bi-cubic function. At larger angles, two cubic equations are fitted to $E_1$ and $E_2$ to calculate $u_1$ and $u_2$, respectively. The voltage output from the ×-wire for the same incoming velocity can drift due to changes in temperature among other factors (Talluru et al. 2014, e.g.). The ×-wire is calibrated before and after each experiment to account for the drift. The drift is assumed to be linear in time between the two calibrations. Figure 3.8 provides an example of the typical voltage shift from pre-calibration to post-calibration. The blue and red symbols in figure 3.8 represent the pre- and post-calibration data points, which allows the quantification of the drift.

### 3.3.2 Error analysis

The error of a measurement can be categorised into systematic and random errors. For an $\times$-wire, one of the factors that contribute to a systematic error is the limitation of the calibration equipment, the StreamLine Pro Automatic Calibrator (Dantec Dynamics). As a dedicated calibrator, the relative standard error is calculated to be about 2% (Jørgensen 2004). Random errors result from the resolution of the Analog-to-Digital (A/D) device, probe positioning, temperature variations, ambient pressure, and humidity (Jørgensen 2004). The data is sampled at 4096 Hz/channel and digitised using a 24-bit National Instruments A/D card, NI 4303, with a range of $\pm$10 V. Error due to misalignment is minimised by aligning the $\times$-wire using a laser alignment tool for both calibration and profile measurement; hence, the misalignment is less than $1^{\circ}$. The temperature at the test site is monitored throughout the experiment and typically increases by 0.05°C to 0.15°C over the duration of one full experiment consisting of 20 or more measurement points. Ambient pressure variations are neglected since the experiments are performed in a closed loop wind tunnel, and the temperature variation is less than 0.15°C. Velocity measurements using a hotwire close to the wall might also introduce heat transfer to the wall. Since the lowest wall-distance in the experiments is greater than $y^+$ =3.5, or 0.5 mm, this error is also eliminated (Jørgensen 2004). As stated earlier, the wall of the wind tunnel is made out of timber, which further reduces the error due to wall-conduction of the hotwire. The combined error caused by all the reasons discussed above is computed using the method and coverage factors specified in Jørgensen (2004, chapter 13 in), where coverage factors are used to account for the distribution of the input variance. Furthermore, both velocity components require two voltages, as in equation 3.1($a$); both voltages are exposed to the above-mentioned errors. Thus, the overall uncertainty of the mean velocity output of the $\times$-wire is below 3%. Baidya et al. 2019a discusses the relative difference of second-order statistics involving $w$ (namely, $\overline{uw}$ and $\overline{w^2}$) measured due to the misalignment of $\times$-wire in the pitch angle. Because of the 15° inclination of the $\times$-wire, the relative difference can be as high as 10% for $\overline{w^2}$ and $\overline{uw}$ in the near-wall region and less than 1% for $z^+ > 50$(Baidya et al. 2019a, figure 9). Hence, data related to $w$ near the wall ($z < 8$ mm) will be treated with care.

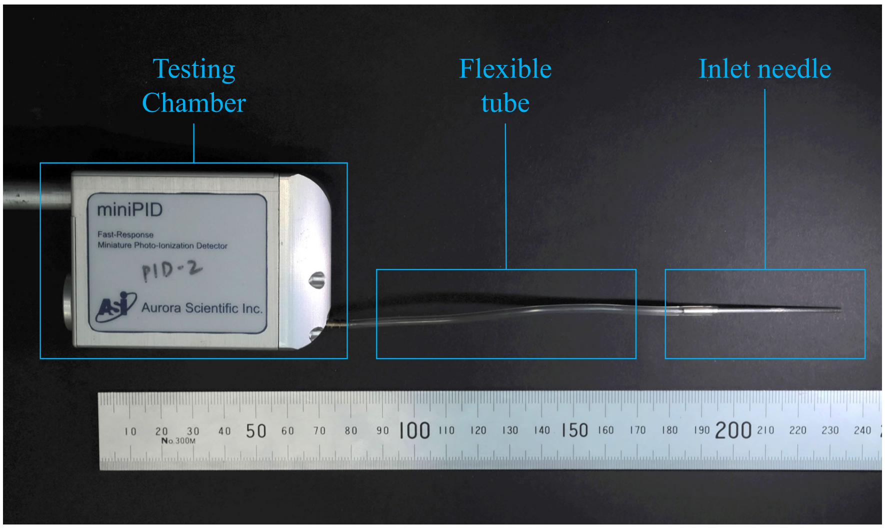


FIGURE 3.9: Image of Photo-Ionisation Detector (PID) with each essential component labelled.

## 3.4 Photo-ionisation detector

A Photo-Ionisation Detector (hereafter referred to as PID) measures the concentration of iso-butylene in the gas mixture in parts per million (ppm). Figure 3.9 shows a photo of the PID and its components. The sample gas is drawn into the testing chamber of the PID through an inlet needle. The gas inside the testing chamber is ionised using ultra-violet light from a flashing lamp. Positive ions are generated and discharged to adhere to the electrodes and generate a voltage output. The voltage output is typically in the millivolt range and needs to be amplified by an external amplifier to improve its detectability by the analog-to-digital converter. The voltage output is then related to the concentration of iso-butylene in the sample gas. The inner diameter of the inlet needle, $d_{\text{inner}}$, is 1.25 mm, and the outer diameter, $d_{\text{outer}}$, is 1.60 mm. In wall units, for the present study, $d^+_{\text{inner}} \approx 8$ and $d^+_{\text{outer}} \approx 10$. The Batchelor scale represents the typical length scale at which the scalar concentration fluctuations are diffused by turbulence, and its value determines the extent of spatial averaging that occurs within the sensing volume of the PID. It is defined as $\lambda_B = \eta/Sc^{1/2}$, where $\eta$ is the Kolmogorov length scale, and $Sc$ is the Schmidt number. $Sc = \nu/D$ for the specific gas used, $D$ being the diffusivity. In the experiments, $Sc_{\text{Ar}} \approx 0.78$, $Sc_{\text{N}} \approx 0.77$, and $Sc_{\text{He}} \approx 0.29$. This means that the smallest mixing length scale for a scalar is larger than that for velocity. Thus, $d^+_{\text{inner}} \approx 8$ is comparable to $\Delta s^+_y \approx 6.4$, and the spatial resolution of the PID is deemed acceptable.

The inlet needle must be placed in close proximity to the $\times$-wire, such that both concentration and velocity measurements can be attributed to a single location in the boundary layer, and further calculations of cross-correlations and joint-PDF are possible. The $\times$-wire and the PID probe are 6 mm apart, and a flexible, narrow tube connects the metal needle to the PID ionising chamber, as shown in figure 3.3 and 3.9. The arrangement is similar to Talluru et al. (2017).

The true frequency response of the PID is approximately 330 Hz. The voltage output from the PID is low-pass filtered at a cutoff frequency of 400 Hz using the Butterworth method through a Krohn-Hite 3380 Tunable Active Filter. Overall, repeatability error and the detection limit of the PID are the main sources of error for PID, which are estimated to be $\pm 2\%$ and $\pm 3\%$, respectively (Talluru et al. 2017).

### 3.4.1 Calibration

The PID is calibrated by supplying gas mixtures of known concentration through the testing chamber and recording the voltage output. Gas of known concentration is generated using the same setup as in figure 3.6: the pre-mixed gases at 15000 ppm are mixed with different portions of air, i.e., before and after an experiment for the positively buoyant plume, the pre-mix gas consisting of 98.5% Helium and 1.5% iso-butylene is further mixed with air to achieve varying concentrations, which is used for PID calibration; likewise for the neutral and negatively-buoyant plume. The resulting concentration of iso-butylene is calculated using the volume flow rates of the pre-mixed gas and air recorded from the two mass flow controllers (MFCs). The calibration points or concentration levels are linearly spaced between 0 and 500 ppm. A set concentration is held constant for 45 seconds, and the average quantities are used for curve-fitting. A quadratic equation is fitted to represent the concentration as a function of the output voltage. The output from the PID drifts over time due to factors such as dust accumulation in the testing chamber, humidity, significant temperature variations,

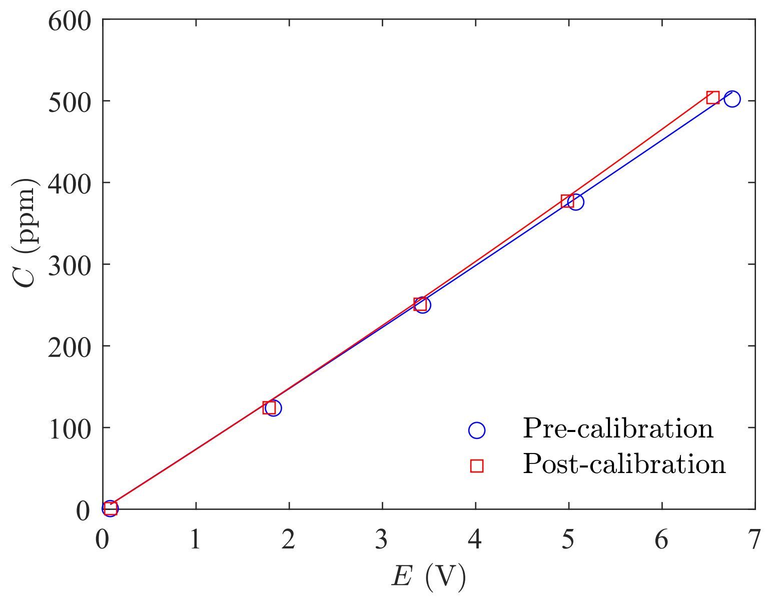


FIGURE 3.10: Comparison of pre- and post-calibration map of a Photo-ionisation detector (PID).

etc. Measured voltages in any given experiment are thus corrected by acquiring pre- and post-calibration curves, as discussed in (Talluru et al. 2019a). Figure 3.10 compares a typical pre- and post-calibration for a PID. Talluru et al. (2017) verified that the PID voltage drifts linearly with time during their experiments; therefore, the linear voltage drift in time (at a set concentration) is corrected, similar to the correction procedure adapted for the $\times$-wire. The background concentration in the wind tunnel is also monitored regularly and subtracted from the concentration data (Nironi et al. 2015).

## 3.5 Background flow

### 3.5.1 Smooth wall boundary layer

The background flow is generated using the smooth wall setup described in section 3.1. The corresponding mean and root-mean-square (RMS) profiles of velocity are compared with Direct Numerical Simulation (DNS) data by Schlatter and Örlü (2010) and Sillero et al. (2013) in figure 3.11 and 3.12. Here, both the mean and the RMS profiles of velocity are normalised using wall units. The resultant boundary layer thickness at the measurement

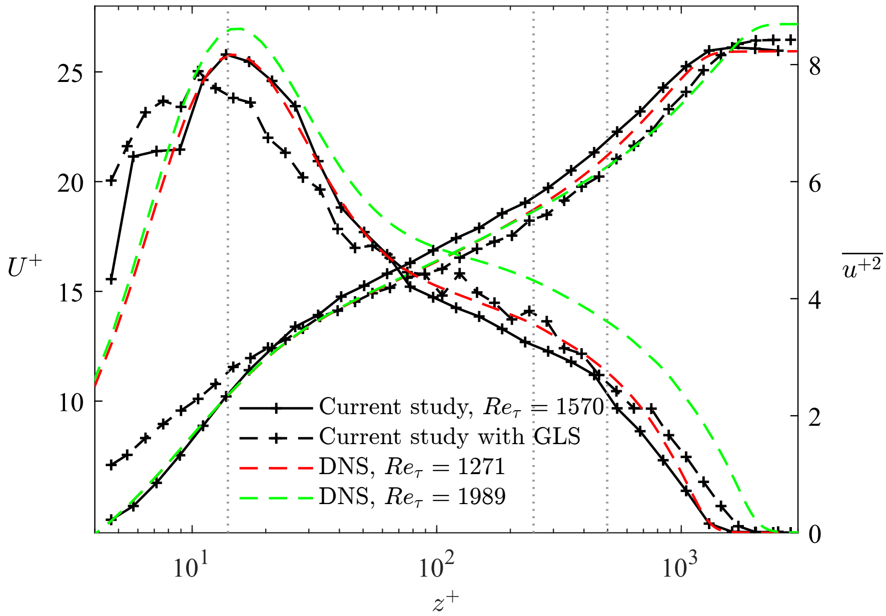


FIGURE 3.11: Profile of mean velocity and RMS, comparing with DNS data. The black dashed lines highlight the flow with the interference due to the releasing nozzle mechanism. Red dashed line: Sillero et al. 2013. Green dashed line: Schlatter and Örlü 2010. The grey dotted lines represent the mid-height of the source diameter for all three source heights: the ground level source (GLS), $S_z/\delta = 0.16$ and 0.32.

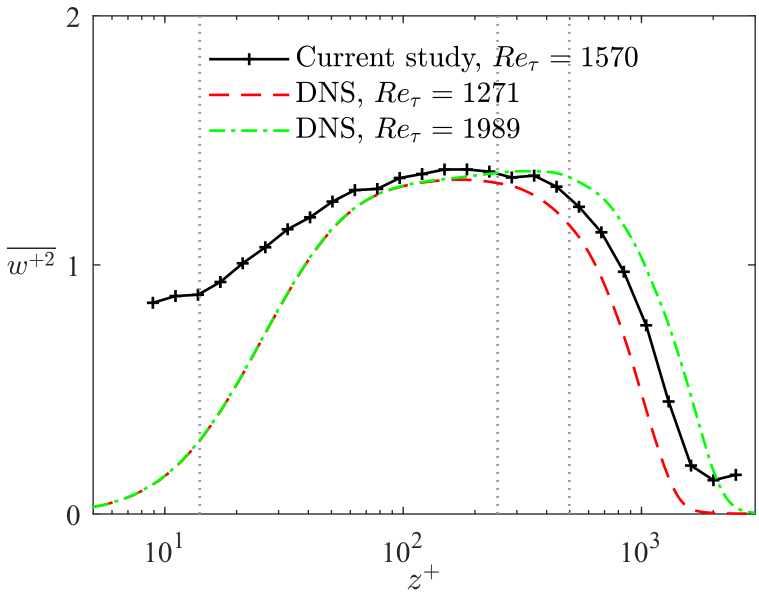


FIGURE 3.12: Profile of wall-normal velocity RMS compared with DNS data, normalised by wall units. Legend same as figure 3.11.

location is $\delta$ = 0.255 m, leading to a local Reynolds number based on freestream velocity, $Re = U_\infty \delta/\nu \approx 43,100$, where $\nu$ is the kinematic viscosity of air at 20 °C. Due to low freestream velocity, the logarithmic region is not well-established in the mean velocity profile, and its span is less than one decade. The friction velocity, $u_\tau \approx 0.0938$ m/s, is calculated using a fit to the composite profile by Chauhan et al. (2009). A low frictional Reynolds number, $Re_\tau = u_\tau \delta/\nu \approx 1570$, is thereby achieved. For the smooth wall boundary layer, the inner peak of $\overline{u^2}^+$ is observed at $z^+ = 15$, and the profile then plateaus after a brief descent (Baidya 2016). In figure 3.11, a clear plateau is present in agreement with DNS data of comparable $Re_\tau$. The profile of $\overline{w^2}^+$ shows an extended plateau between $z^+ \approx 80$ and 130 in figure 3.12, consistent with that from DNS. However, $\overline{w^2}^+$ at $z^+ \lessapprox 70$ ($z \lessapprox 8$ mm) measured by $\times$-wire deviates from DNS results due to the finite size of the $\times$-wire (Baidya 2016). Therefore, the statistics related to $w$, such as the vertical scalar fluxes, in this range will be treated with care and the deviation does not affect the elevated sources, whose locations are indicated by the two grey dashed lines on the right in figure 3.12. The interference of the releasing nozzle is negligible on the mean velocity profile. For $\overline{u^2}^+$, a slightly lower plateau at smaller $z^+$ due to the nozzle can be observed at the nozzle height for the ground level source, similar to the previous observations made by Talluru et al. (2017) in the same facility. The streamwise velocity spectra at the measurement location at different heights are plotted in figure 3.13. The slope of the energy spectrum on a log-log scale in the inertial subrange of a fully turbulent flow (very large $Re$) should be $-5/3$, as shown in equation 2.18. However, this is not the case for the low-$Re$ flow in this study, and hence the inertial subrange is barely recognisable.

### 3.5.2 Rough wall boundary layer

The velocity profiles over the two roughness patterns are compared against the smooth wall profile in figure 3.14. The measurements are taken halfway between two adjacent roughness blocks, as shown by the blue dots in figure 3.5. As expected, the roughness elements significantly reduce $U$ and increase $\sqrt{\overline{u^2}}$ in the lower part of the boundary layer. The profiles of $U$ and $\sqrt{\overline{u^2}}$ for both roughness cases are similar above the block height, as indicated

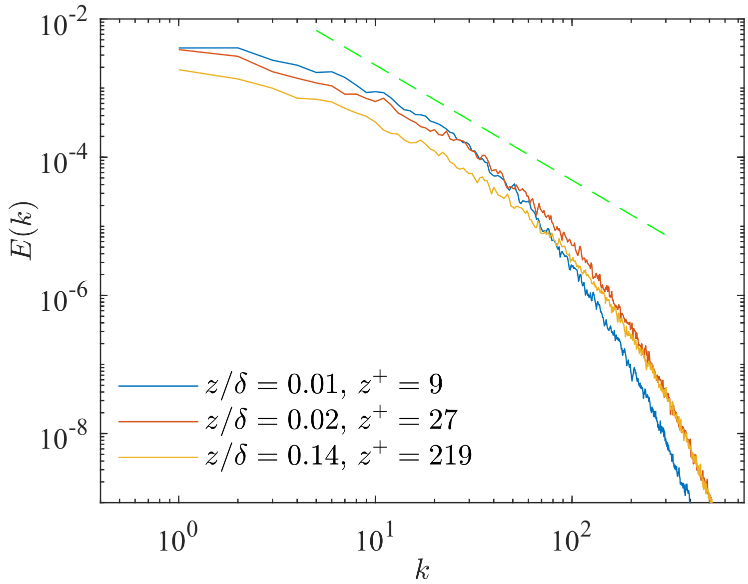


FIGURE 3.13: Velocity spectra at different heights in the smooth wall TBL. The green dashed line indicates the $-5/3$ law.

by the grey dashed line. The subscripts 'R1' and 'R2' are used to refer to the rough-wall configurations with $\Delta s/h = 1$ and $\Delta s/h = 2$, respectively. In comparison to the smooth wall boundary layer, the boundary layer over both roughness configurations is slightly thicker than that of the smooth wall, i.e., $\delta_{\mathrm{R1}} = \delta_{\mathrm{R2}} = 0.340$ m. As a result, $h/\delta_{\mathrm{R1}} = h/\delta_{\mathrm{R2}} = 0.123$. In figure 3.14($b$), maximum velocity fluctuations are observed at the height of the roughness blocks, which is visible as a peak in the RMS profile at $z = 0.04$ m. Additionally, $\sqrt{\overline{u^2}}$ at $z = \Delta s$ for R1 is higher than R2 since the streamwise spacing for R1, $\Delta s_{\mathrm{R1}}$, is smaller.

The velocity profiles in wall units are plotted in Figure 3.16. Since the roughness elements introduce more turbulence into the flow, the logarithmic region in both rough-wall boundary layers is more prominent than the smooth wall case. The velocity defect chart method developed by Djenidi et al. (2019) is used to calculate the friction velocity. The velocity defect chart for $\Delta s/h = 1$ is plotted in figure 3.15. $\delta_{99}$ is set to 0.2235 m. The residual sum of squares (RSS) of velocity defect between $0.3 < y/\delta_{99} < 1$ is computed for different $u_\tau$ values, and the $u_\tau$ associated with the smallest RSS has been chosen. Though the lower limit is recommended to be $y/\delta_{99} = 0.2$, it is not feasible in this study as the roughness is too large in comparison to the boundary layer thickness and causes a jump in the mean velocity profile.

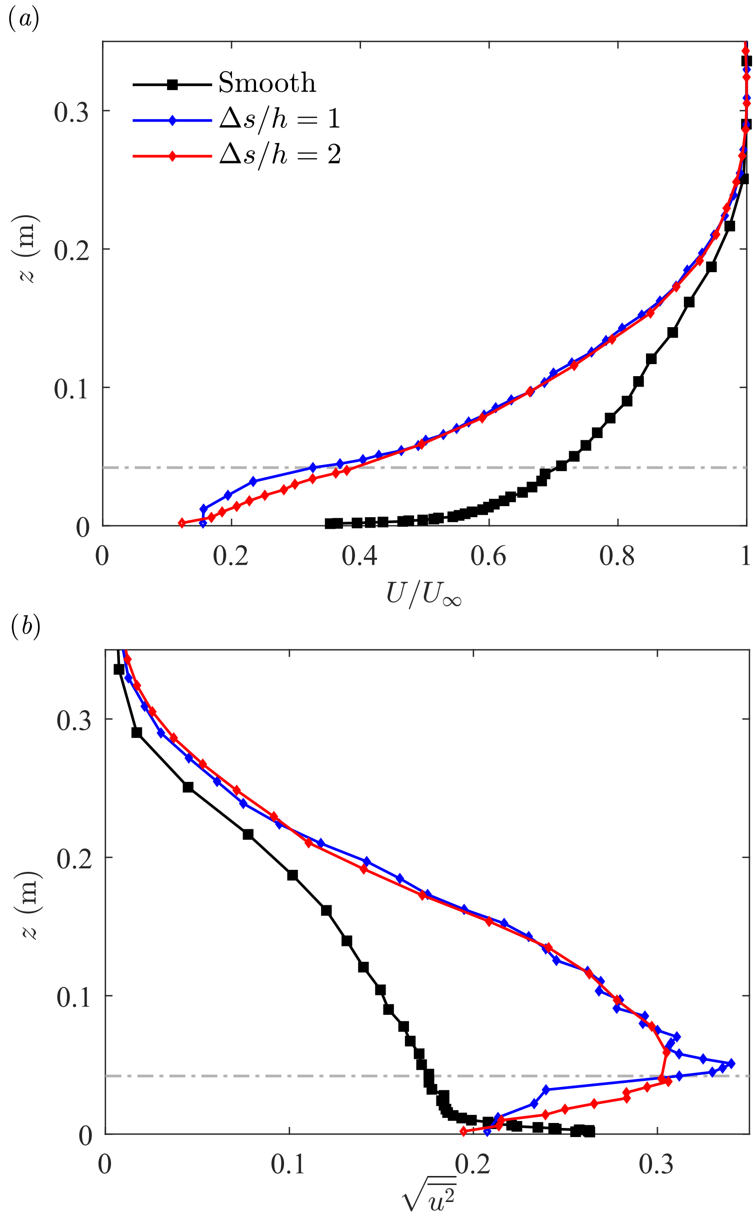


FIGURE 3.14: Comparison of the velocity field between the smooth and rough wall boundary layers. $\Delta s/h$ is the streamwise spacing between cubic blocks. (*a*) mean streamwise velocity and (*b*) RMS of streamwise velocity. The grey dash-dotted line represents the height of the roughness elements.

The friction velocity for the two roughness configurations, thus obtained, are listed below: $u_{\tau,\,\mathrm{R1}} = 0.208$ m/s, $u_{\tau,\,\mathrm{R2}} = 0.206$ m/s.

Figure 3.16(*a*) highlights the difference in $U^+$ between the smooth wall and rough wall cases. As discussed in section 2.3.2, surface roughness leads to a downshift of the mean velocity

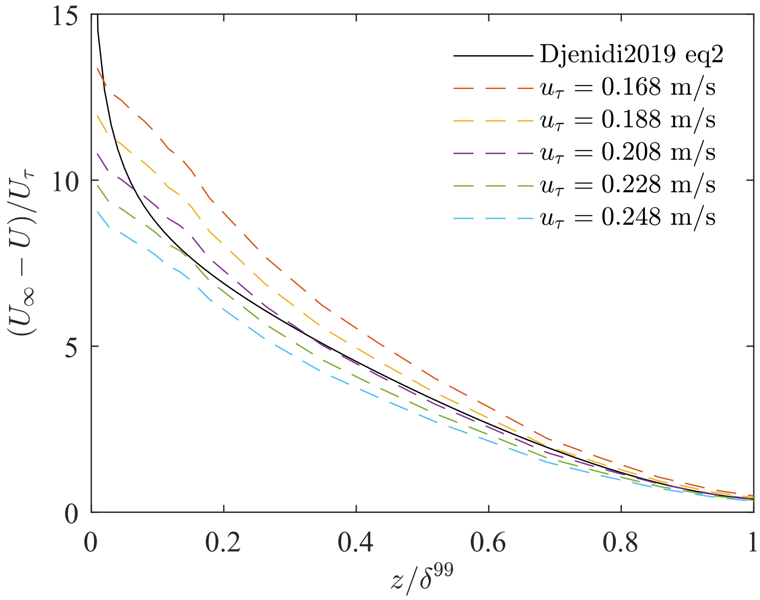


FIGURE 3.15: Velocity defect chart method to estimate $u_\tau$. The solid black line is equation 2 by Djenidi et al. 2019.

profile of magnitude $\Delta U^+$, as per equation 2.19. $\Delta U^+$ for $\Delta s/h = 1$ and $\Delta s/h = 2$ is approximately 14. However, the shift of R1 is slightly larger than that of R2 by approximately 0.3. This is similar to the past experimental results by Abdelaziz et al. (2022) where the larger spacing of sinuous roughness and rod roughness resulted in a smaller $\Delta U^+$. Another method to quantify the roughness is to calculate its equivalent sand-grain roughness, $k_s$ or $k_s^+$. Fitting the data points in the logarithmic region to equation 2.20, $k_{s,\,\mathrm{R1}} \approx k_{s,\,\mathrm{R2}} \approx 477$. In wall units, $k^+_{s,\,\mathrm{R1}} \approx 1092$, $k^+_{s,\,\mathrm{R2}} \approx 1104$. Therefore both roughness patterns fall into the fully rough regime according to table 2.1. Figure 3.16(*b*) shows the RMS of the velocity. The velocity measurement at the height of approximately $z^+ \approx 15$, where the inner peak is expected to occur in a smooth wall turbulent boundary layer, was not obtained. However, there is no indication that the inner peak is present at this location. The outer peak at $200 < z^+ < 300$ commonly observed for rough flow is not present here either. Instead, there is a peak near the roughness height. This is because for fully rough flow where the size of the roughness element is large relative to the boundary layer thickness ($\delta/h = 8.5$ in this case), the large roughness elements break down the near-wall turbulent structures (Squire et al. 2016).

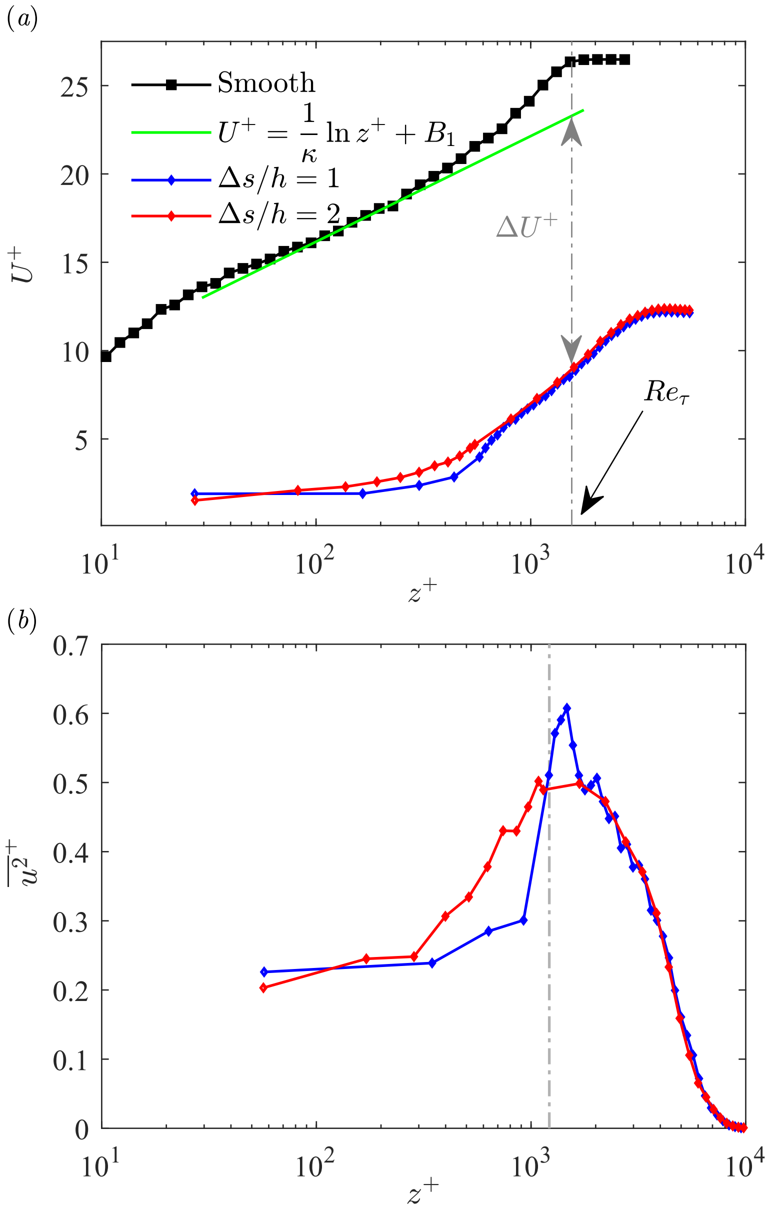


FIGURE 3.16: (*a*) Profiles of mean velocity in wall units for the smooth wall and the rough wall boundary layers, showing the downshift $\Delta U^+$. The green lines are the logarithmic law. (*b*) Profiles of RMS of velocity in wall units for the rough wall boundary layer. The smooth case is omitted here as its magnitude is significantly larger. The grey dashed line is the height of roughness.

The spectra and pre-multiplied spectra at the height of the roughness elements of the rough wall boundary layer are compared with the smooth-wall spectra in figure 3.17. The inertial subrange for the roughness case is more prominent due to the larger $Re_\tau$, extending around a decade. Furthermore, at higher frequencies, the energy spectrum decreases slower for the

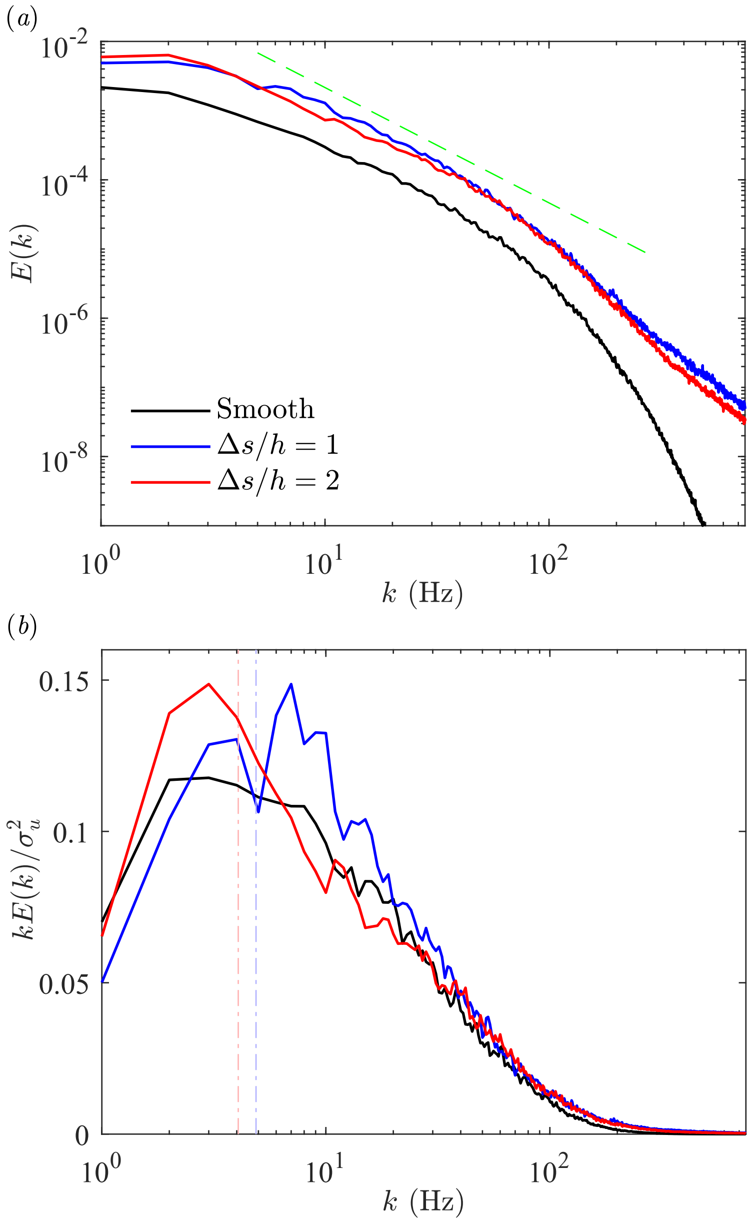


FIGURE 3.17: (*a*) Velocity spectra at the height of the block (40 mm) for all three roughness configurations. The green dashed line indicates the $-3/5$ law. (*b*) Pre-multiplied spectra at the height of the roughness block.

rough wall flow field. As observed in figure 3.17(*b*), the peak frequency $k_{peak}$ is approximate $U(z = h)/\lambda$ where $\lambda$ is the distance between the leading edges of two adjacent roughness elements in the streamwise direction. The peak on the pre-multiplied energy spectra for R1 is at a lower frequency compared to that of R2 since R1 has a smaller spacing. For the smooth case, the peak is the least prominent.

CHAPTER 4

# Plume evolution

---

This chapter presents the experimental results obtained from the smooth wall experimental setup discussed in the last chapter. The emphasis is on the evolution and self-similarity of the mean concentration and the standard deviation for the smooth wall case.

## 4.1 Mean and RMS of Concentration

The concentration field can be decomposed like the velocity field: $\tilde{C} = C + c$. The RMS of concentration, denoted by $\sigma_c$, is calculated as $\sigma_c = \sqrt{\overline{(C - \tilde{C})^2}}$. Notably, the effect of density difference on the concentration field can be observed for both source heights. For elevated sources, the relative rise and plunge of the positively- and negatively buoyant plume can be observed in the profiles in figure 4.1. The lighter plumes appear to be higher, though the difference in plume widths is not obvious in figure 4.1, and a quantitative comparison will be discussed later. There is yet any wall effect at $S_x/\delta = 2$ for $S_z/\delta = 0.31$ in figure 4.1($h$). The vertical profile of $C$ and $\sigma_c$ of an elevated source away from the wall is Gaussian, repeated here,

$$C(z) = C_{\text{max}} \exp\left[-\left(\frac{z - z_{\text{CL}}}{\delta_z}\right)^2\right] \tag{2.24}$$

with $z_{\text{CL}}$ being the plume centreline height and $\delta_z$ the plume half-width inferred from the mean concentration. It is worth noting that equation 2.24 can also be used to describe the behaviour of $\sigma_c$ by replacing $C_{\text{max}}$ and $\delta_z$ with $\sigma_{c,\text{ max}}$ and $\delta_\sigma$, respectively. The dashed lines in the figure are the fit of equation 2.24 to the data, evidencing the Gaussian model's applicability. As the plume grows further downstream or when an elevated source is released closer to the wall ($S_z/\delta = 0.16$), a Gaussian model does not fully describe the spread due to the presence of the ground. This applies to the data for $S_z/\delta = 0.16$ at $S_x/\delta = 4$ in figure 4.7($f$). Here a reflected-Gaussian distribution is more appropriate to describe the vertical profile of $C$ and $\sigma_c$. Using the mean concentration $C$ as an example,

$$C(z) = C_{\text{max}} \left[ \exp\left( -\frac{(z+z_{\text{CL}})^2}{2\delta_z^2} \right) + \exp\left( -\frac{(z-z_{\text{CL}})^2}{2\delta_z^2} \right) \right]. \tag{2.26}$$

This observation is consistent with those of Fackrell 1980; Nironi et al. 2015; Talluru et al. 2017, etc.

For a ground-level source, $C_{\text{max}}$ is always at the wall and is larger for the denser plume, and the plume spread is thinner. but the plumes spread, $\delta_z$, is thicker for lighter gas. The mean concentration profiles of a ground-level source can be described by a half-Gaussian, which is consistent with that by Robins et al. (2001a).

The dimensional profiles of the standard deviation of concentration, $\sigma_c$, are shown in figure 4.2. The evolution of $\sigma_c$ is similar to that of $C$. The RMS profile for the ground-level source in figure 4.2 likewise can be described as a half-Gaussian or reflected-Gaussian.

As per the equations presented above, the mean and RMS concentration profiles can be fully characterised by three key parameters: the plume centreline, the maximum value at the plume centreline, and the plume half-width. The downstream variation of these parameters enables the full description of the mean or RMS concentration profile. Therefore, this section focuses on investigating these three parameters. In the case of an elevated source, the parameters are derived from the Gaussian equation given by 2.24 or the reflected-Gaussian equation given by 2.26. It is important to note that the mean plume-centreline height is not discussed for the ground-level source, as the power-law fit for the profile assumes it is at the wall.

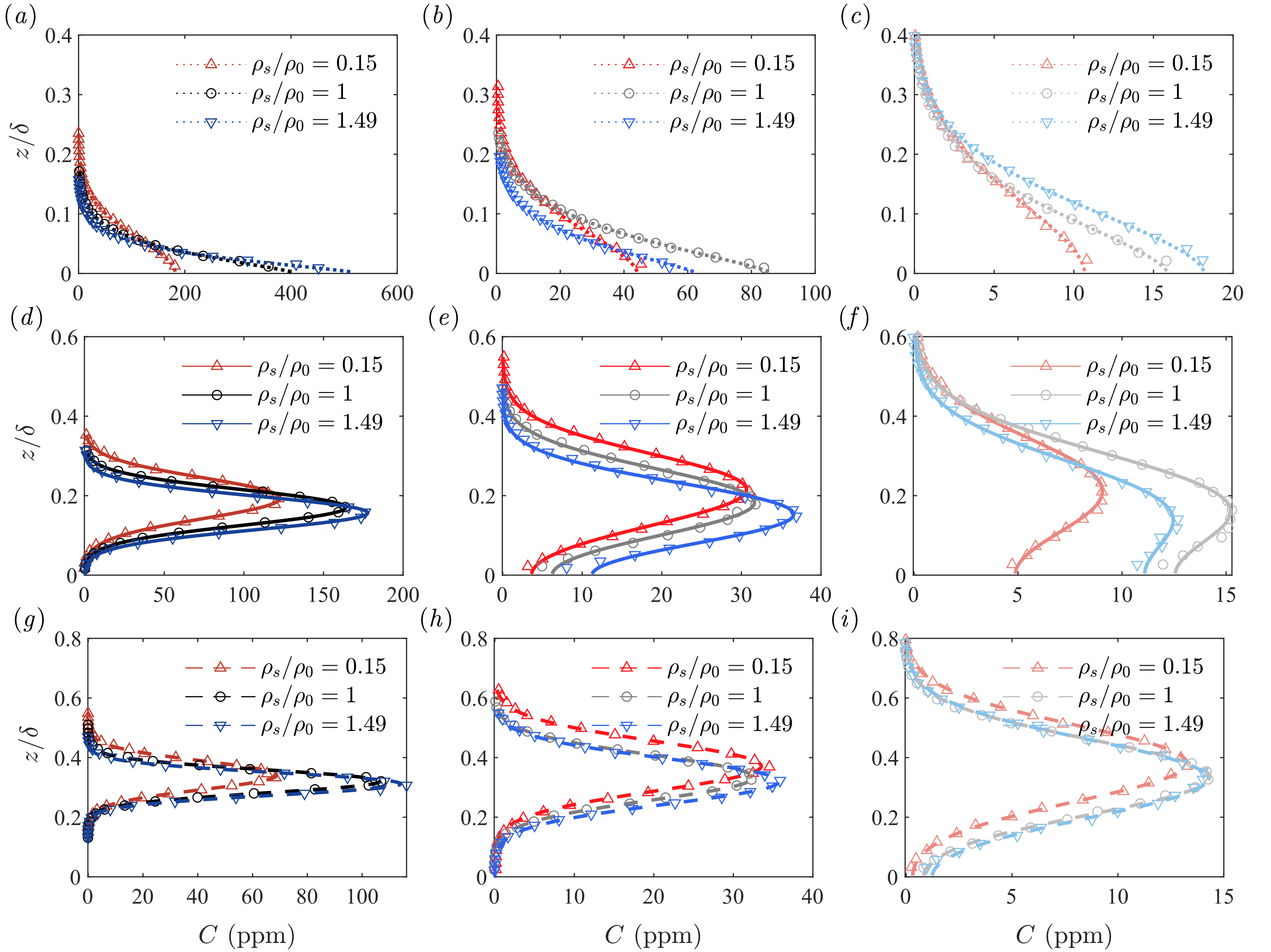


FIGURE 4.1: Vertical profile of mean concentration for all source distances, source heights, and density ratios. The dotted lines, solid lines, and dashed lines are either Gaussian or reflected Gaussian. (*a-c*): $S_z = 0$. (*d-f*): $S_z = 40$ mm. (*g-i*): $S_z = 80$ mm. (*a,d,g*): $S_x/\delta = 1$. (*b,e,h*): $S_x/\delta = 2$. (*c,f,i*): $S_x/\delta = 4$.

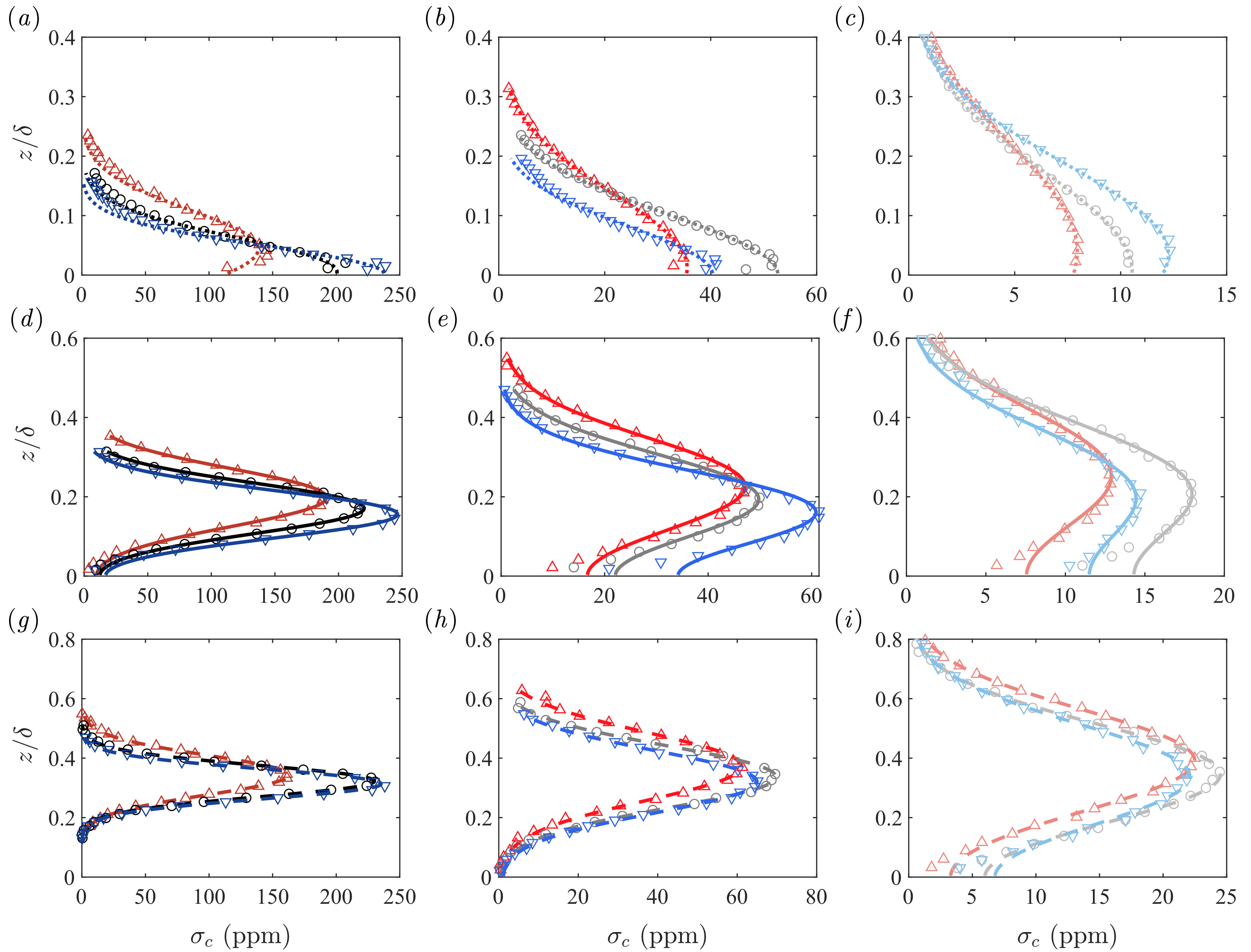


FIGURE 4.2: Vertical profile of standard deviation of concentration for all source distances, source heights, and density ratios. The dotted lines, solid lines, and dashed lines are either Gaussian or reflected-Gaussian. (*a*-*c*): $S_z = 0$. (*d*-*f*): $S_z = 40$ mm. (*g*-*i*): $S_z = 80$ mm. (*a,d,g*): $S_x/\delta = 1$. (*b,e,h*): $S_x/\delta = 2$. (*c,f,i*): $S_x/\delta = 4$. Legend same as figure 4.1.

## 4.2 Plume centreline

To study how the height of the plume centreline changes with downstream distance quantitatively, the height of the plume centreline for $S_z$ = 40 mm and 80 mm is plotted against the downstream distance in figure 4.3. The variation in plume centreline height due to density difference is observable in this figure. For ground-level source $C_{\text{max}}$ is always at the wall therefore, the mean plume centreline is omitted.

The behaviour of $\rho/\rho_\infty = 1$ is analysed first as the baseline. For $S_z$ = 40 mm, the $z_{\text{CL}}$ tends upwards from $S_x/\delta$ = 1 to 2. From $S_x/\delta$ = 2 to 4, $z_{\text{CL}}$ grows gradually because the plume is wide enough to be affected by the wall, and it is slowly evolving to the mean profile of a ground-level source. This behaviour is also observed by (Fackrell and Robins 1982). For the neutral plume released at $z_{\text{CL}}$ = 80 mm, $z_{\text{CL}}$ does not decrease for any $S_x/\delta$ locations, which means there is no wall effect yet. Briggs (1969) proposed $\Delta z \propto x^{2/3}$ to describe the plume rise, where $\Delta z$ is the change in height of the plume centreline. The model is fitted for the light case from $S_x/\delta = 0$ to 2 in figure 4.3 as the red-dashed and the red-dotted lines. The data at $S_x/\delta = 4$ is excluded because the plume centreline lowers as the profile transforms to a half-Gaussian.

$z_{\text{CL}}$ of the light plume deviates further from the source height than those of the neutral and heavy plumes, very likely resulting from the different $\Delta\rho$ relative to the ambient. The authors found no empirical equation to describe the relation between $z_{\text{CL}}$ and the downstream distance for the heavy or neutral gas.

The plume centreline of the RMS profile for the ground-level source tends upwards, also observed by Fackrell and Robins (1982). This is due to the wall-normal fluctuations in the lower part of the turbulent boundary layer.

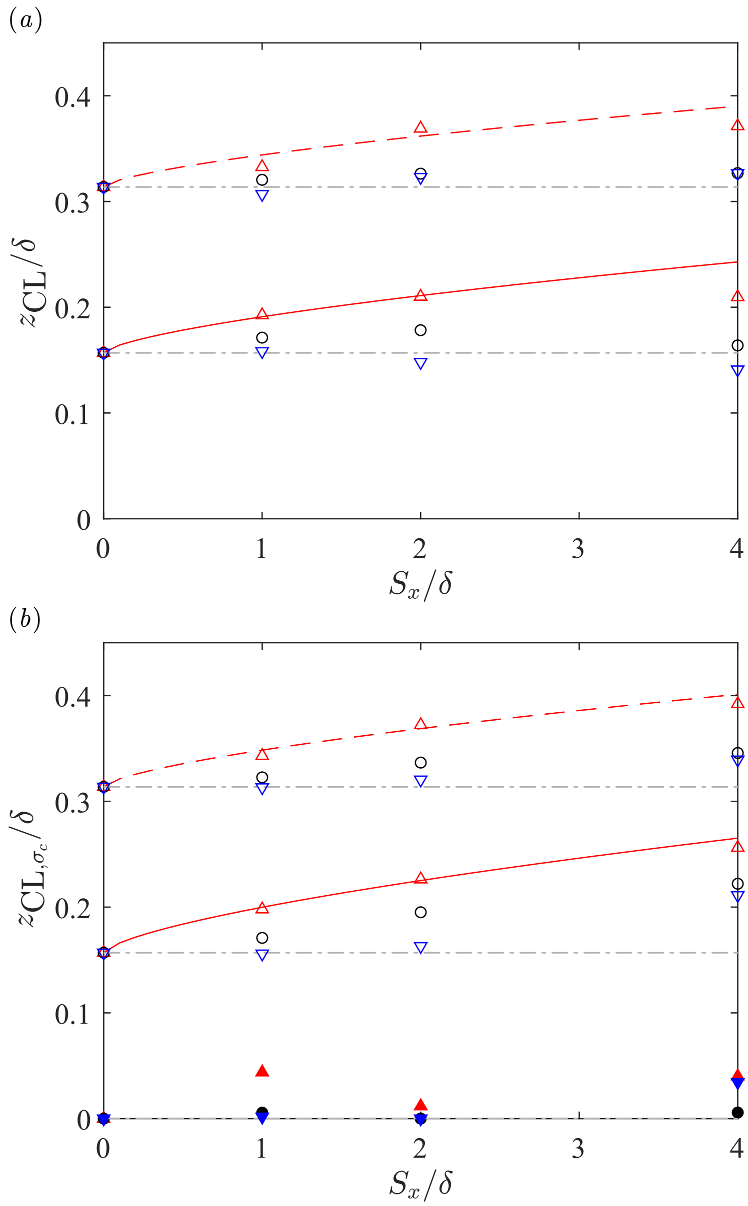


FIGURE 4.3: Plume centreline for (*a*) mean concentration and (*b*) RMS of concentration. The grey lines are the source height. The red-dashed and the red-dotted lines are fitted to $\Delta z \propto x^{2/3}$. Legend same as figure 4.1.

## 4.3 Local maximum of mean and RMS

Figures 4.4(*a*) and 4.4(*b*) display the peak values of mean and RMS at each downstream distance, respectively. The decay of these values with distance follows a power-law behaviour, such that $C_{\max}$ and $\sigma_{c,\,\max}$ are the largest for heavy gas and smallest for light gas. The widest

| $\rho_s/\rho_\infty$ | 1.48 | | 1 | | 0.15 | |
|---|---|---|---|---|---|---|
| | $C$ | $\sigma_c$ | $C$ | $\sigma_c$ | $C$ | $\sigma_c$ |
| GLS | -2.06 | -2.07 | -2.32 | -2.13 | -2.36 | -2.15 |
| $S_z = 40$ mm | -1.88 | -1.94 | -1.74 | -1.83 | -1.95 | -2.07 |
| $S_z = 80$ mm | -1.18 | -1.42 | -1.44 | -1.61 | -1.50 | -1.71 |

TABLE 4.1: Decay rate for $C_{\text{max}}$ and $\sigma_{c,\,\text{max}}$

plume (in the vertical) is associated with the lightest gas, while the narrowest is linked to the heaviest gas. This aspect will be discussed later. In terms of each source height, the ground-level source sees the quickest decay (larger power-law exponent compared to the elevated sources). This is due to high Reynolds shear stress close to the wall. The decay rate of $C_{\text{max}}$ and $\sigma_{c,\,\text{max}}$ is very similar for the same gas and same source height, as indicated by the exponents listed in table 4.1. Another interesting trend is that $C_{\text{max}}$ of the ground-level source is larger than that of the two elevated sources, but $\sigma_{c,\,\text{max}}$ ground level is smaller, consistent with the findings by Fackrell and Robins (1982) and Baidya (2016). This is because the turbulent scales are smaller close to the ground.

Past studies have assumed that $C_{\text{max}}$ decays according to a power-law of the form $C_{\text{max}} \propto x^q$, citing varying values of $q$. For instance, Hoot et al. (1973) reported a value of $q \approx -1.68$ for heavy gas released at ground level and noted that as the concentration of denser gases slowly approaches that of air, their maximum concentrations decay at a slightly faster rate due to the attenuation of density effects by diffusion. The power-law decay has been observed for $C_{\text{max}}$ of a neutral plume in TBL, while $\sigma_{c,\,\text{max}}$ does not exhibit power-law decay (figure 3 in Fackrell and Robins 1982). However, for a heat source in homogeneous turbulence, Karnik and Tavoularis (1989) found that the decay rate of $\sigma_{c,\,\text{max}}$ varies from 1.7 to 3.2.

## 4.4 Plume half-width

The plume half-width calculated from the mean and the standard deviation, $\delta_Z$ and $\delta_{z,\sigma}$, is plotted for the ground-level source as shown in figures 4.5($a$) and 4.5($b$). For ground-level sources, Robins (1978) found that $\delta_z$ follows a power law, where $\delta_z \propto x^m$ and $m = 0.61$ to

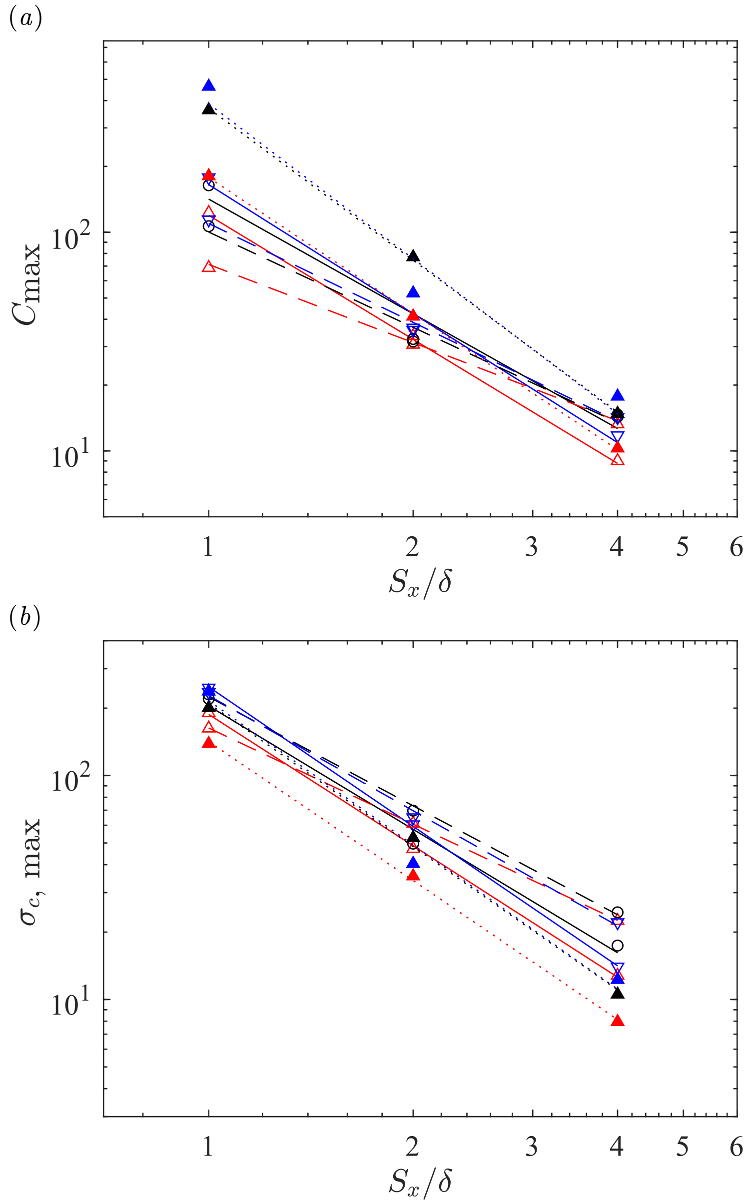


FIGURE 4.4: Value at plume centreline for (*a*) mean concentration and (*b*) RMS of concentration. Legend same as figure 4.1.

0.65 for rural flow when the mean velocity exponent, $n'$, is 0.14 (see equation 2.15). The power-law fits are plotted as dotted lines in Figure 4.5, and the calculated exponents are tabulated below in Table 4.1. However, it is warranted that due to the small number of data points in $x$, the value of $m$ is only indicative. In contrast, Fackrell and Robins (1982) released neutrally buoyant gas in a turbulent boundary layer and found $m$ = 0.75 for $1 < z_{\mathrm{CL}}/\delta < 10$.

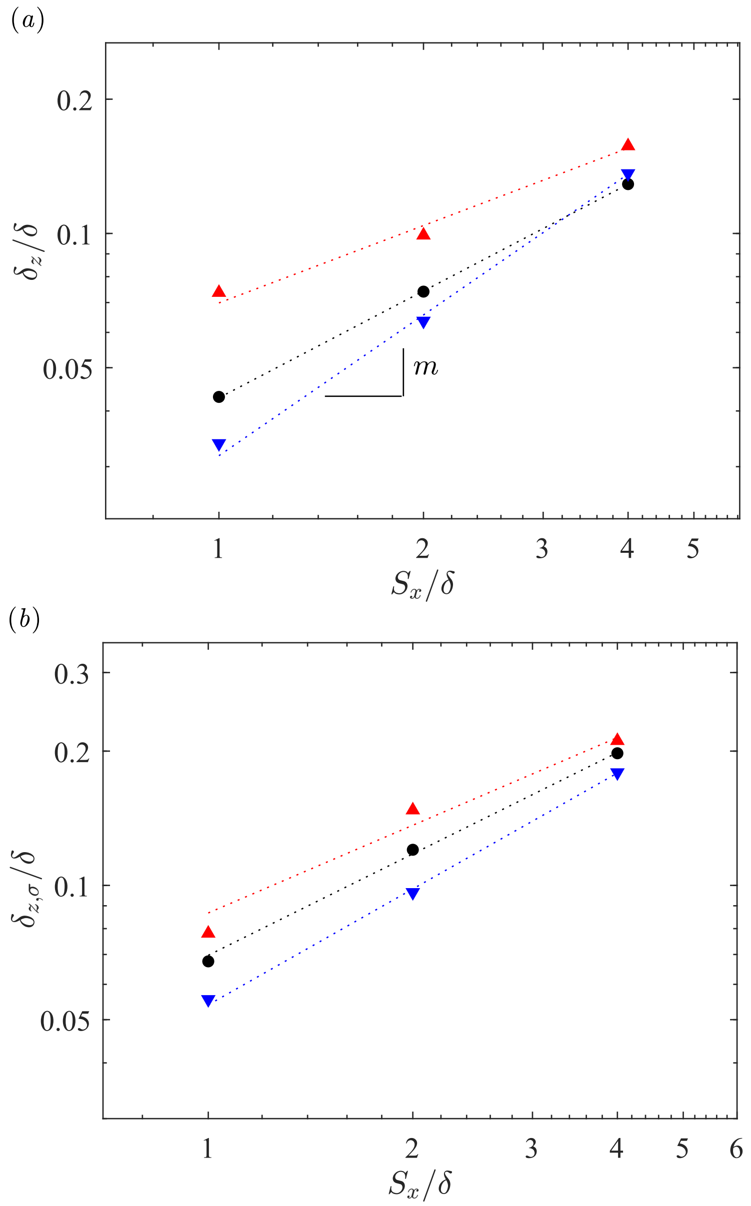


FIGURE 4.5: Half-width of ground-level source calculated from (*a*) mean concentration and (*b*) RMS of concentration. The dotted lines are power-law fits, and the exponent $m$ are tabulated in table 4.2. Other legends as figure 4.1.

The half-widths for elevated sources are plotted in Figure 4.6. The power-law fit for ground-level sources is excluded for elevated sources because the fit is poor for all elevated sources. Stapountzis et al. (1986) reported that $m$ is a constant dependent on the downstream distance, varying from 0.4 to 1, then 0.5 in grid-generated turbulence. Fackrell and Robins (1982)

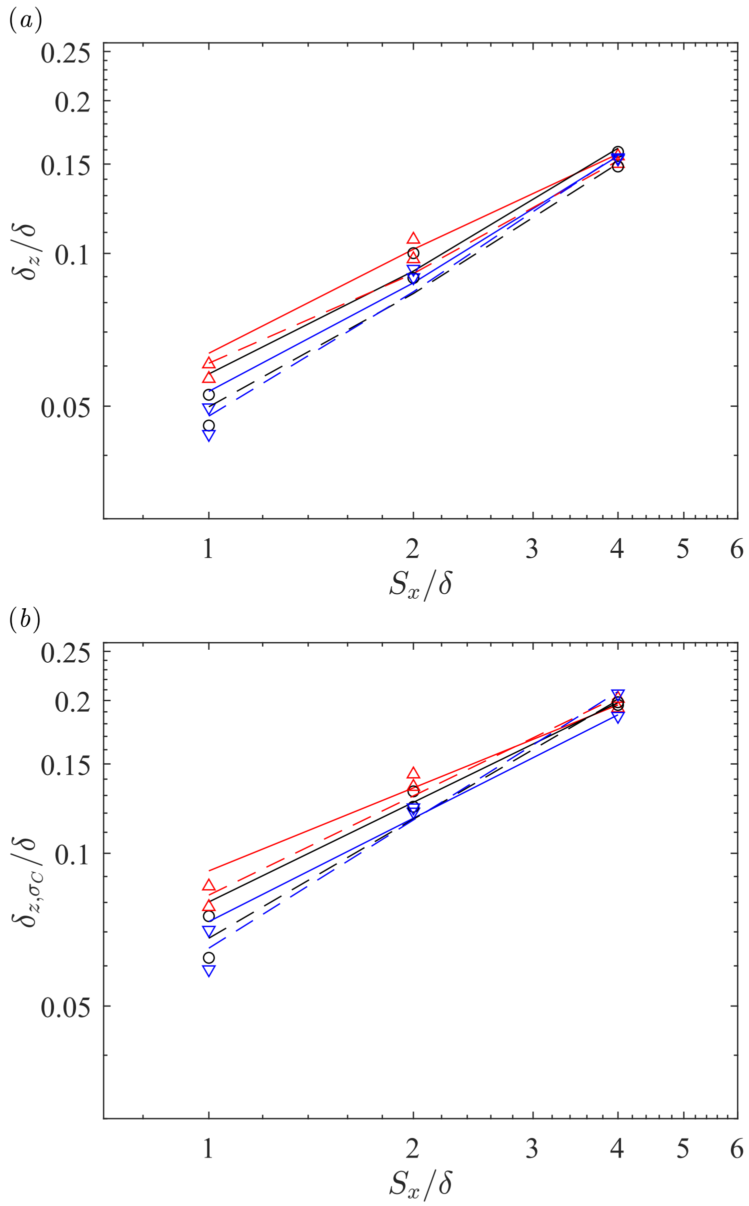


FIGURE 4.6: Half-width of elevated source calculated from (*a*) mean concentration and (*b*) RMS of concentration without fit. The lines are used to differentiate source heights and are not functional trend lines. Legend same as figure 4.1.

observed that the half-width for elevated sources is significantly larger than that for ground-level sources, which is also observed in the current study. However, the magnitude of the difference is smaller. This observation is only valid up to a certain height in a turbulent boundary layer. Talluru et al. (2019b) studied point-source tracer gas released at eight

| $\rho_s/\rho_\infty$ | 1.48 | 1 | 0.15 |
|---|---|---|---|
| $m$ for $\delta_z$ | 1.06 | 0.774 | 0.579 |
| $m$ for $\delta_{z,\sigma}$ | 0.84 | 0.711 | 0.686 |

TABLE 4.2: Predicted growth rate, $m$, for plume half-width calculated from mean and r.m.s of concentration for ground-level sources.

different heights in a turbulent boundary layer and found that both $\delta_z$ and $\delta_{z,\sigma}$ scale with the standard deviation of vertical velocity and are largest at around $0.1\delta$.

An interesting trend is also observed where $\delta_{z,L} > \delta_{z,N} > \delta_{z,H}$ for almost all cases and $\delta_{z,L}$ and $\delta_{z,H}$ approaches the neutral plume width downstream. A similar trend was also observed by Hoot et al. (1973) for heavy plumes of various densities ($1 \leq \rho_s/\rho_\infty \leq 3$). According to Talluru et al. (2019b), the vertical half-width of neutral plumes, $\delta_z$ or $\delta_{z,\sigma}$, scale well with the local vertical turbulence intensity, $\overline{w^2}$. For an incompressible fluid, where $\rho_\infty$ is constant, $\overline{w^2}$ also represents the vertical shear stress. In the case of buoyant plumes, one needs to consider the buoyancy force. The associated stress is proportional to $(\rho_s - \rho_\infty)gl$ where $l$ is a relevant length scale, and $g$ is the acceleration due to gravity. For a heavier gas, the buoyancy stress points downward, opposing the positive vertical shear stress $\overline{w^2}$. This forces the plume to diffuse/spread laterally compared to neutral and lighter gas plumes, and hence its vertical plume width is thinner compared to a neutral and a positively buoyant plume. The buoyancy stress of a lighter plume is positive and acts in the same direction as $\overline{w^2}$, leading to a thicker plume in the vertical direction compared to a heavier plume.

Furthermore, $\delta_{z,\sigma}$ is larger than $\delta_z$, as previously reported by Warhaft (1984) and Talluru et al. (2017). The ratio is approximately 1.5 in grid-generated turbulence Warhaft (1984).

Assuming a slender plume with a symmetrical spread,

$$Q = 2\pi U(z_{\mathrm{CL}})C_{\mathrm{max}}\sigma_1^2 \tag{4.1}$$

where $Q$ is the volume flow rate and $\sigma_1$ is a scale of the symmetrical plume width (Arya and Arya 1999, see eqn 6.44). This equation indicates that the decay of $C_{\mathrm{max}}$ is twice the plume growth rate in either direction when the release is constant. According to table 4.1 and

4.2, the growth rate of the mean plume for the ground level source is less than half of the decay of $C_{\text{max}}$. Therefore, in this experiment, it can be inferred that, for $S_z = 0$, the plume is asymmetric, and the plume is thicker in the spanwise direction than in the vertical direction. Though the growth rate of the mean plume is not calculated for elevated sources in table 4.1, an estimate of the slope of the curves in figure 4.6($a$) shows that for $S_z = 40$ mm, the spanwise plume width is larger than the vertical plume width while this is not the case for $S_z = 80$ mm.

## 4.5 Self-similarity of mean and standard deviation of concentration

The normalised profile of $C$ and $\sigma_c$ are plotted in figure 4.7 using the three parameters discussed above that can fully characterise the mean and RMS concentration profiles, namely the plume centreline, the maximum value at the plume centreline and the plume half-width, as shown in the above equations. The vertical axis represents the distance relative to the plume centreline, $\xi = z - z_{\text{CL}}/\delta_z$. A self-evident collapse is observed for $C$ and $\sigma_c$. However, for the normalised profile of $\sigma_c$, outliers from the ground-level source data (solid symbols) are observed near the upper tail and the centreline. This behaviour could be attributed to ground-level source profiles being more exponential than Gaussian. Additionally, outliers in the upper tail for both normalised profiles mainly correspond to the heavy gas (blue symbols).

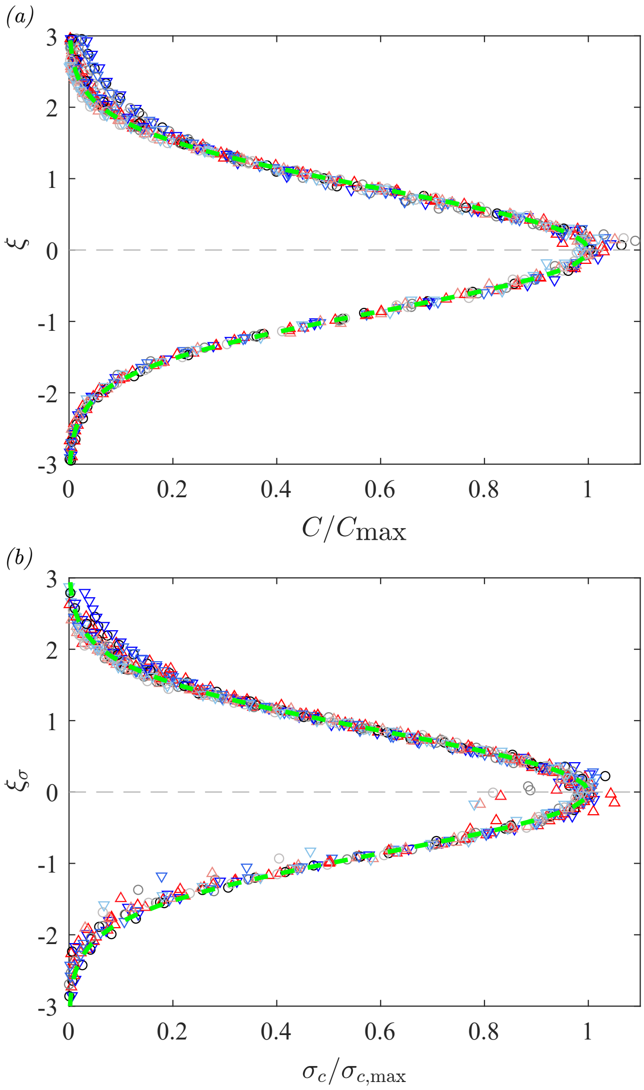


FIGURE 4.7: Profile of (*a*) mean and (*b*) r.m.s. of concentration, normalised. The green dashed lines are standard Gaussian.

CHAPTER 5

# Self-similarity of higher-order moments of concentration

---

Chapter 4 discusses the plume evolution of the mean and r.m.s. of concentration fluctuations, which are the first two moments of the instantaneous concentration. Higher-order moments are examined in this chapter. High-order moments are only studied in a few past studies in the 90s and early 00s. The amount of work dedicated is very little compared to the first two moments. A possible reason is that calculating the higher-order moments accurately requires long-duration measurements and stationary flow conditions.

In the first section, attention is given to the third and fourth-order moments and the mathematical relation deducted by Mole and Clarke (1995) is tested using the present data. The next section discusses higher-order moments ($n > 4$) and their similarity.

## 5.1 Skewness and kurtosis

The skewness and kurtosis of concentration are defined as

$$Sk = \frac{\overline{(\tilde{C}-C)^3}}{\sqrt{\overline{c^2}}^3}, \tag{5.1}$$

$$Ku = \frac{\overline{(\tilde{C}-C)^4}}{\sqrt{\overline{c^2}}^4}. \tag{5.2}$$

The $Sk$ vs $Ku$ for all $S_z$ and $S_x$ are plotted in figure 5.1. The green-dashed line plots the fitted equation 2.27 discussed in section 2.4.1.1, repeated as below,

$$Ku = A(Sk^2) + B \tag{2.27}$$

Figures 5.1($a$) & 5.1($b$) plot the distributions of $Ku$ and $Sk$ along with the fitted curve on linear-linear axes in 5.1($a$) and log-linear axes in 5.1($b$) to emphasise small $Sk$ values. As evident in the figures, the curve fits the data quite well. The parameters $A$ and $B$ from the current study are compared against those reported in previous studies in table 5.1. The value for $A$ agrees relatively well with some variation in $B$.

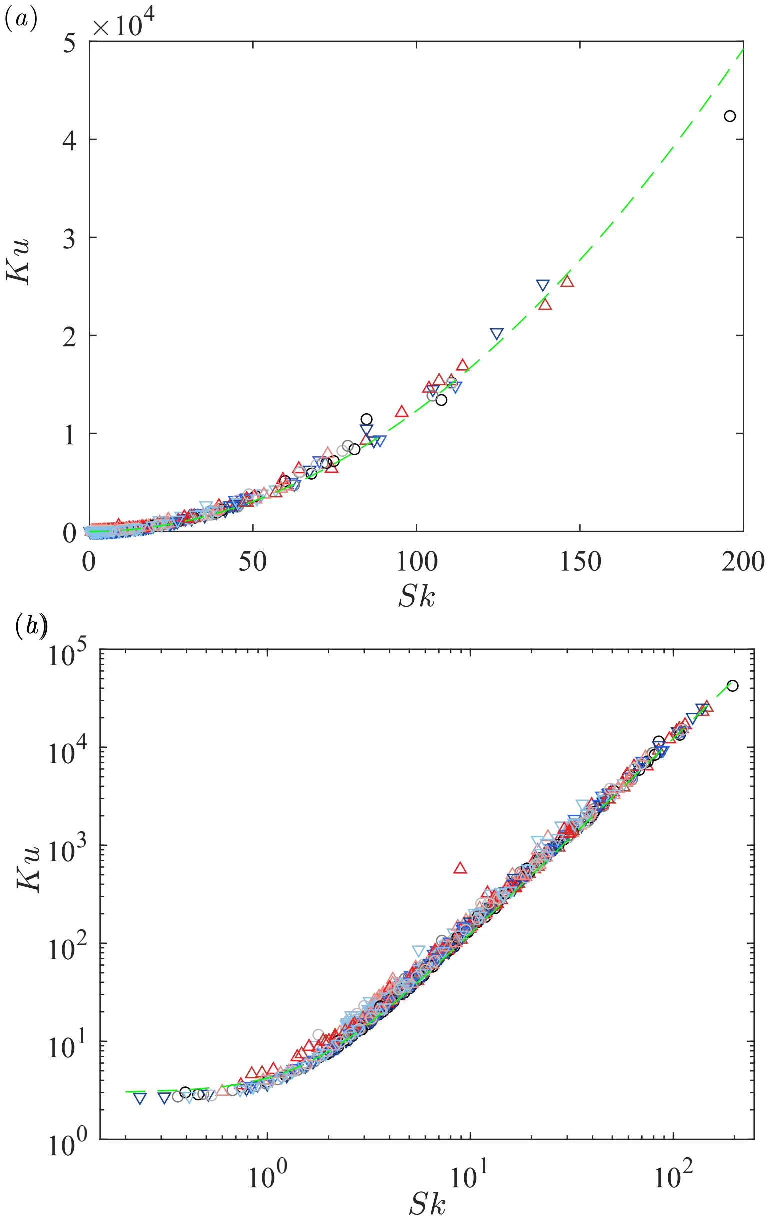


FIGURE 5.1: Skewness vs kurtosis of concentration for all source heights and source distances on a ($a$) linear-linear scale ($b$) log-log scale. The green dashed line is fitted to equation 2.27 with $A = 1.231$ and $B = 3$.

| | A | B | Notes |
|---|---|---|---|
| Mole and Clarke (1995) | 1.31 | 0.6 | |
| Schopflocher and Sullivan (2005) | 1.13-1.43 | around 2 | $A$ and $B$ increase downstream. |
| Nironi et al. (2015) | 1.67 | 2.99 | Fitting $Ku = A \cdot Sk^C + B$ where $C = 1.97$. |
| Current study | 1.231 | 3 | |

TABLE 5.1: Comparison of fit parameters for equation 2.27 in past studies.

In chapter 4 and previous studies, it has been observed that the mean and RMS profiles of concentration exhibit self-similarity within a plume. By normalising the profiles using the three Gaussian parameters from equations 2.24 or 2.26, namely the centreline height, the centreline concentration, and the plume half-width, the profiles collapse onto a single curve. This method is also applied to test if the normalised skewness ($Sk$) and kurtosis ($Ku$) exhibit self-similarity. Figure 5.2 shows the normalised $Sk$ and $Ku$ profiles for elevated sources as a function of normalised $z-$ coordinate. In this plot, the vertical axis is represented by $\xi = \dfrac{z - z_{\text{CL}}}{\delta_z}$, which is the normalised distance from the plume centreline, similar to the normalisation used for $C$ in Figure 4.7($a$). Both $Sk(z)$ and $Ku(z)$ are divided by their respective values at the centreline, $Sk_{\text{CL}}$ and $Ku_{\text{CL}}$. It is observed that the normalised skewness ($Sk_c$) and kurtosis ($Ku_c$) profiles of concentration also exhibit self-similarity within the plume. Previous studies, such as Sawford and Tivendale (1992), plotted $Sk$ similarly to demonstrate its Gaussian behaviour. For the elevated source, both $Sk$ and $Ku$ profiles collapse onto a single curve after the adopted normalisation, exhibiting symmetry about the plume centreline. However, there is no specific equation that describes these curves, unlike the Gaussian equation for mean and RMS profiles. In the case of the ground-level source, $Sk$ and $Ku$ behave differently than the ES for $\xi > 0$, as shown by the solid symbols in Figure 5.2. The $Sk$ of the ground-level source decreases more rapidly from the centreline compared to the elevated source. The concentration signal always exhibits positive skewness ($Sk > 0$) because of $\tilde{C} > 0$, resulting in a right-skewed distribution. The magnitude of $Sk$ becomes significantly larger at large $|\xi|$, consistent with observations by Chatwin and Sullivan (1990) and Karnik and Tavoularis (1989). This is because the distribution becomes more skewed towards zero (relative to the mean) due to higher intermittency further away from the plume centreline. The intermittency is caused due to strong shear at the interface between the plume and the background flow. Regarding $Ku$, its value also increases with distance from the centreline. This is because the maximum instantaneous concentration is significantly larger than the mean concentration at locations further from the centreline. It is worth noting that the plots of $Sk$ and $Ku$ exhibit more scatter compared to those of $C$ and $\sigma_c$ since higher-order moments require longer data acquisition time to converge. As a reminder, in this study, the sampling duration is 300 seconds. Nironi (2013) plotted the dimensional third and fourth

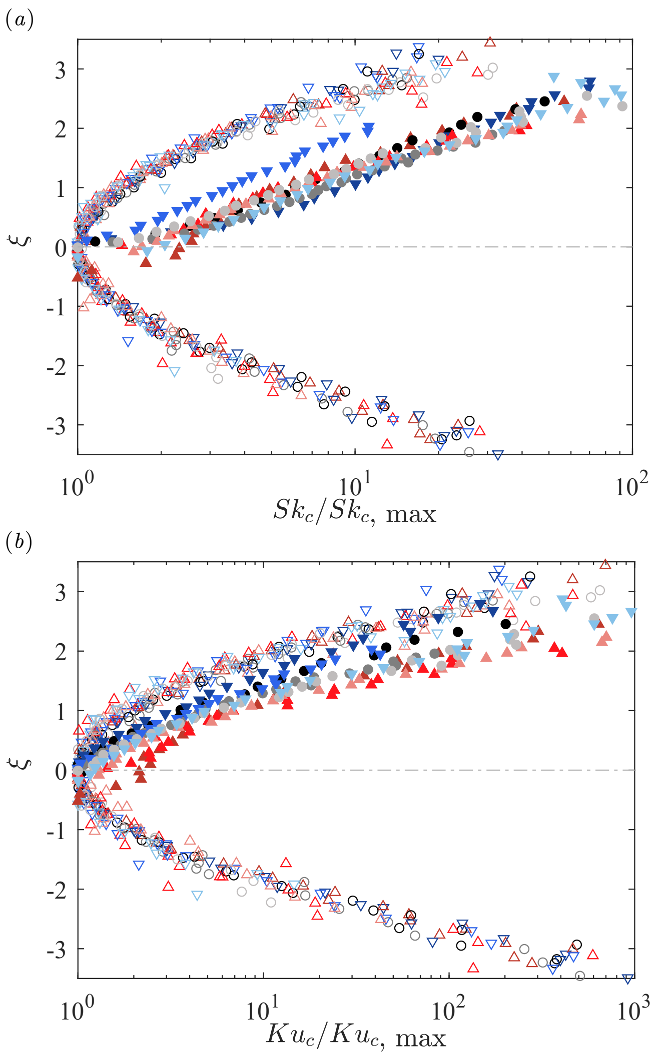


FIGURE 5.2: Profile of (*a*) Skewness of concentration normalised by the centreline value and (*b*) Kurtosis of concentration normalised by the centreline value. The solid symbols are ground-level sources, and the hollow symbols are elevated sources ($S_z = 40$ mm and 80 mm).

central moments in their figures 7.3 to 7.6. Though their vertical axis is not normalised as $\xi$, the profiles are Gaussian-like by inspection.

For the first four moments studied in this section and the previous chapter, the difference between each density ratio is indistinguishable (see figure 4.7 and 5.2) when the three normalising parameters are used (plume centreline, plume half-width, and the corresponding value at the plume centreline).

## 5.2 Self-similarity of higher central moments

Chapter 4 and the preceding section explored four moments: $C$, $\sigma_c$, $Sk$, and $Ku$. Of these, $C$ and $\sigma_c$ possess dimensions, while $Sk$ and $Ku$ are dimensionless and referred to as normalised central moments. A general expression for the $n$-th normalised central moment can be given as:

$$\frac{\overline{c^n}}{\sqrt{\overline{c^2}}^{n/2}} = \frac{\overline{(\tilde{C} - C)^n}}{\sqrt{\overline{c^2}}^{n/2}},\ n > 1 \tag{5.3}$$

Substituting $n = 2$ in the above equation yields $\dfrac{\overline{c^2}}{\sqrt{\overline{c^2}}^{1/2}} = \sigma_c$. Similarly, for $n = 3$, we obtain $Sk$, and so forth.

In contrast, the numerator in equation 5.3 represents the central moments of concentration. These moments quantify the deviation from the mean, $C$. Mathematically, the $n$-th central moment is defined as:

$$\overline{c^n} = \overline{(\tilde{C} - C)^n},\ n > 1 \tag{5.4}$$

Within this section, the focus lies on the dimensional central moments. Since $\overline{c^1} = 0$ and does not represent the same concept as $C$, $n = 1$ is excluded. As $\overline{c^1}$ = 0, $C$ is considered the reference for comparing higher central moments.

The analysis of $\overline{c^n}$, where $n$ ranges from 1 to 6, reveals that the higher-order central moments also exhibit Gaussian distributions. Therefore, the same method, which is used to collapse the profiles of mean and standard deviation in figure 4.7 in chapter 4, is also employed to normalise the higher-order moments. Equation 2.24 can be modified as follows for the higher-order moments:

$$\overline{c^n}/\overline{c^n}_{\text{max}} = \exp\left[-\left(\frac{z - z_{\text{CL}}}{\delta_{z,n}}\right)^2\right],\ n > 1 \tag{5.5}$$

Here, $\overline{c^n}_{\text{max}}$ represents the maximum value of the $n$-th central moment, and $\delta z, n$ is the plume half-width calculated from the $\overline{c^n}$ profile. The term $z_{\text{CL}}$ denotes the location of the plume centreline. A subscript $n$ is not used here because the plume centreline for each moment, typically the location of $\overline{c^n}_{\text{max}}$, remains unchanged. Figure 5.3 presents the central moments for $n = 1$ to 6 when normalised by their respective centreline values. The figure demonstrates that the profiles of the first six central moments are well-described by a Gaussian equation. The mean and RMS profiles of concentration for all source conditions collapse relatively well onto a Gaussian curve (5.5) with only a few outliers at $\xi = 0$ and at large $|\xi|$. Higher-order moments exhibit larger scatter due to difficulties in achieving statistical convergence (Sreenivasan et al. 1980; Chatwin and Sullivan 1990). For example, two outliers are circled to illustrate the slower convergence of higher-order moments in figures 5.3(*d*), 5.3(*e*), and 5.3(*f*). In figure 5.3(*d*) corresponding to $\overline{c^4}$, the two outliers are located above the Gaussian curve at approximately $\xi = 2$. They further deviated from the standard Gaussian in figure 5.3(*e*). This discrepancy becomes more pronounced in the figure 5.3(*f*) for $\overline{c^6}$. Those two points might suffer from the inaccuracy of the mean concentration itself.

An intriguing trend emerges; $\overline{c^2}$ approaches 0 at approximately $\xi = 2$, while $C$ and higher-order moments approach 0 at $\xi = 4$. This suggests that $\overline{c^2}$ has a wider plume width than the other moments.

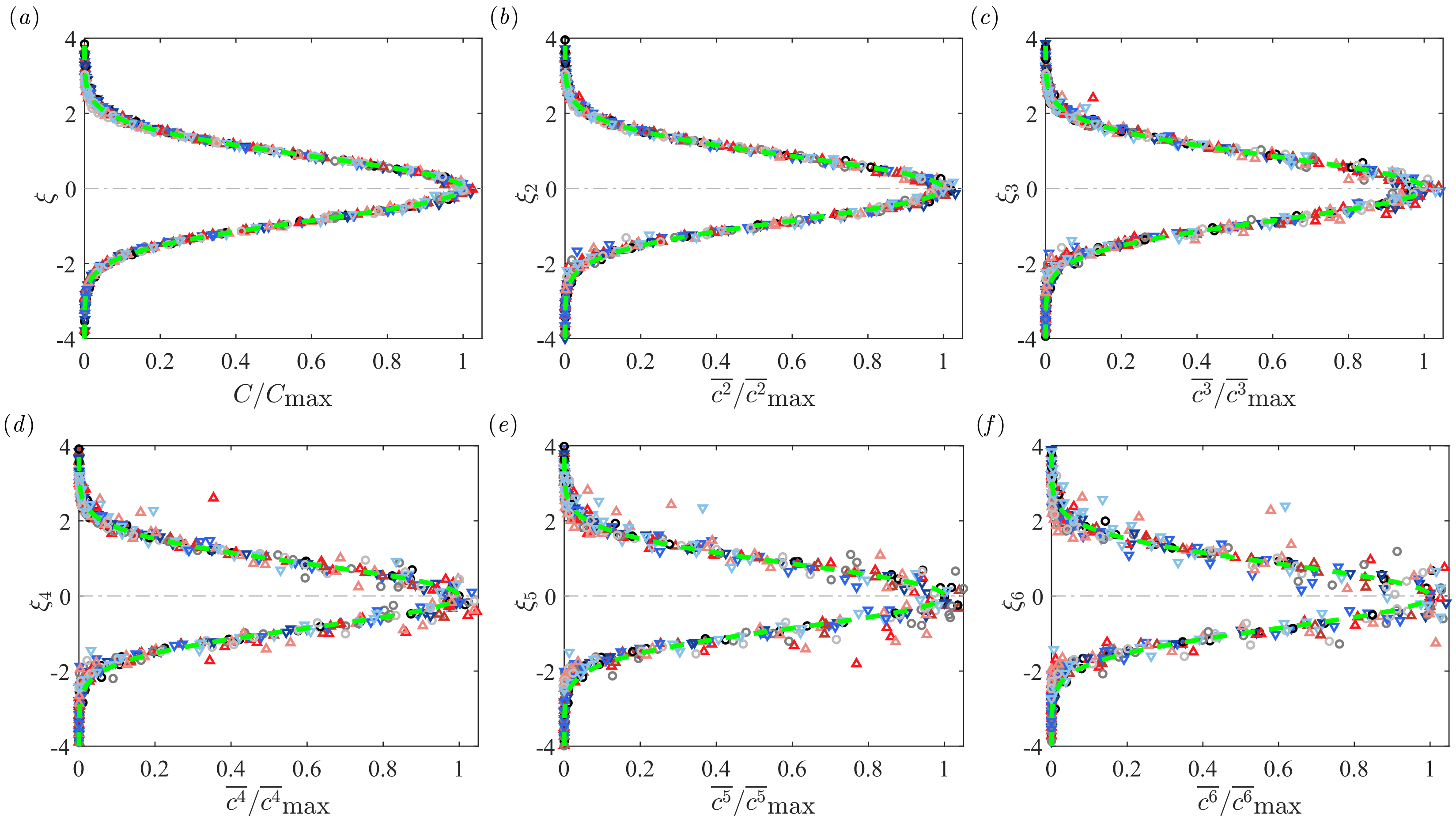


FIGURE 5.3: Profile of first to sixth central moments for elevated sources. The vertical axes are normalised by the relative plume half-width and plume centreline. The horizontal axes are normalised by the centreline value.

Figure 5.4 displays the plume half-widths calculated from each moment for all measurements with elevated sources. The half-width of the second central moment, $\delta_{z,2}$, is the largest, approximately 1.35 to 1.45 times $\delta_z$. Although no specific study has reported this value, data extracted from Talluru et al. (2017, figure 8) indicate a similar ratio. For each moment, the half-width decreases from $n = 2$ onwards. Sawford and Tivendale (1992) also observed that the plume width narrows for higher-order moments though they only studied up to $n = 4$. This is because higher-order moments decrease more rapidly towards the plume edges, resulting in a shorter vertical distance between the height of $\overline{c^n}_{\text{max}}$ and $\overline{c^n}_{\text{max}}/2$ as $n$ increases.

An exception occurs at $S_z = 40\,\text{mm}$, when $S_x = 4\delta$. In this case, $\delta_{z,2}$ is only around 20% larger than $\delta_z$. Additionally, the ratios $\delta_{z,n}/\delta_{z,1}$ for $n \geq 3$ are lower than the other cases. This discrepancy arises because of the influence of the wall on the plume development, and thus, it cannot be considered an isolated elevated source.

Except for the outlier profiles for $S_z = 40\,\text{mm}$ when $S_x = 4\delta$, all other plumes released aloft the ground level can be regarded as originating from an isolated elevated source. The difference in plume spread can be observed in figure 4.1. This indicates that a single-length scale characterises the mixing of the scalar for isolated elevated sources. In the analysis presented here, it is found that the plume half-width is the appropriate length scale that can be used to model the mixing of an isolated scalar plume of different densities.

The author would like to note that the density difference affects the higher-order moments the same way as it does on mean and r.m.s.; the half-widths of $\overline{c^n}$ of the light case is the largest and the corresponding $z_{\text{CL}}$ is the highest compared to the neutral and the heavy plumes, though the exact values are not plotted here. Furthermore the plume centreline height is independent of $n$ but on $\rho_s/\rho_0$ and $S_x$. It is interesting that the effect of $\rho_s/\rho_0$ diminishes in figure 5.3, meaning the density difference did not affect the symmetry about the plume centreline for higher moments.

Using $\overline{c^n}/\overline{c^n}_{\text{max}}$ instead of moments normalised as in equation 5.3 offers two advantages. Firstly, $\overline{c^n}/\overline{c^n}_{\text{max}}$ can be accurately described by a three-parameter Gaussian model. In contrast, the model that describes the shape of higher-order moments normalised as in equation 5.3,

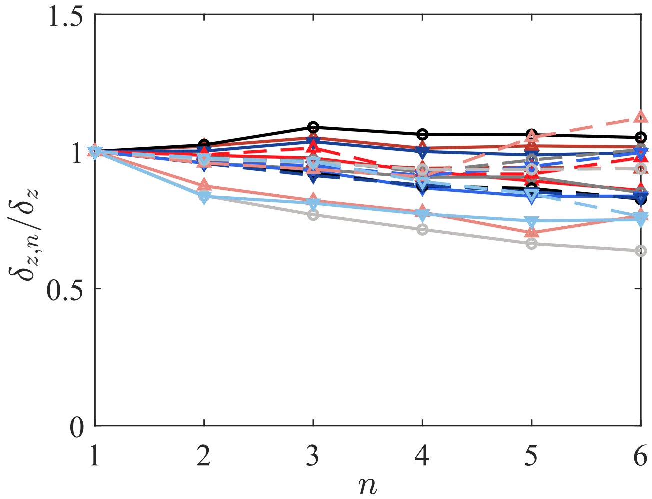


FIGURE 5.4: Plume half-width calculated from the $n$-th moment divided by plume half-width calculated from mean concentration profile for elevated sources only.

such as $Sk$ and $Ku$ as shown in figure 5.2, remains unknown. Secondly, the use of moments normalised as in equation 5.3 tends to exaggerate the effects of high intermittency at the plume edges, where the mean concentration $C$ is relatively low. Consequently, the variations in the moments normalised as in equation 5.3 closer to the plume centreline, which are of greater interest, are difficult to observe. By utilising $\overline{c^n}/\overline{c^n}_{\max}$, the variations of higher-order moments near the plume centreline are clearly observed.

## 5.3 Comparison with Chatwin and Sullivan (1990)

The results obtained in this study are compared with the $\alpha - \beta$ model proposed by Chatwin and Sullivan (1990). This model establishes a relationship between higher-order central moments and the mean, $C$. The constants $\alpha$ and $\beta$ represent the effects of molecular diffusion on $C_{\max}$ and $\overline{c^2}$, respectively. The equation presented in their work (Chatwin and Sullivan (1990, equation 3.3)) is as follows:

$$\overline{c^2} = \beta_2 C(\alpha C_{\max} - C) \tag{5.6}$$

The values of $\alpha$ and $\beta_2$ for different datasets are provided in table 2 of Chatwin and Sullivan (1990), where it is observed that $1 < \alpha < 2$ and $\beta_2 < 1$. Fitting our data to this equation gives $\alpha$ close to 1.9, and $\beta_2 \approx -4$.

Chatwin and Sullivan (1990) also derived a relationship between $C$ and higher-order moments. For higher-order moments, their equation 4.4 in Chatwin and Sullivan (1990) can be expressed as follows:

$$\overline{c^n} = \beta_n \frac{C_{\text{max}}^n}{\alpha}[x(\alpha - x)^n + (-1)^n(\alpha - x)x^n] \tag{5.7}$$

where $x = C/C_{\text{max}}$. $\beta_2$ corresponds to the same $\beta_2$ in equation 5.6. Their findings indicate that while this theory accurately reproduces $\overline{c^2}$, it fails to generate accurate values for $Sk$, and the predicted trend of $Ku$ does not align with the observed data (figure 7 in Chatwin and Sullivan 1990).

It is attempted to predict higher-order moments using equation 5.7 and the $C$ values obtained in this study. Although the input profile of $C$ follows a Gaussian distribution, the output profiles of higher-order moments may not necessarily exhibit a Gaussian shape. Since all higher-order moments ($n > 2$) have the same shape, the profile of $\overline{c^2}/\beta_n$ is plotted for different values of $\alpha$. The parameter $\beta_n$ is included here since it is a constant and does not affect the shape of the profile. The shape of the predicted higher-order moments is influenced by the value of $\alpha$. When $\alpha$ falls within the range of $1 < \alpha < 2$ as suggested by Chatwin and Sullivan (1990), the profiles exhibit multiple peaks that do not agree with our data. However, as $\alpha$ increases, the profiles tend to evolve towards a Gaussian shape. Interestingly, previous studies by Warhaft (1984) and Lavertu and Mydlarski (2005) have reported the presence of double peaks in higher-order moment profiles near the source, suggesting that $\alpha$ may differ in the near field or far field region.

Alternatively, fitting equation 5.7 using higher-order moments yields values of $\beta_n$ that are less than 1, which is consistent with the findings of Chatwin and Sullivan (1990). However, it is important to note that the value of $\alpha$ is not constant across different moments and varies significantly within the range of $O(0)$ to $O(2)$, deviating considerably from the proposed range of $1 < \alpha < 2$ by Chatwin and Sullivan (1990).

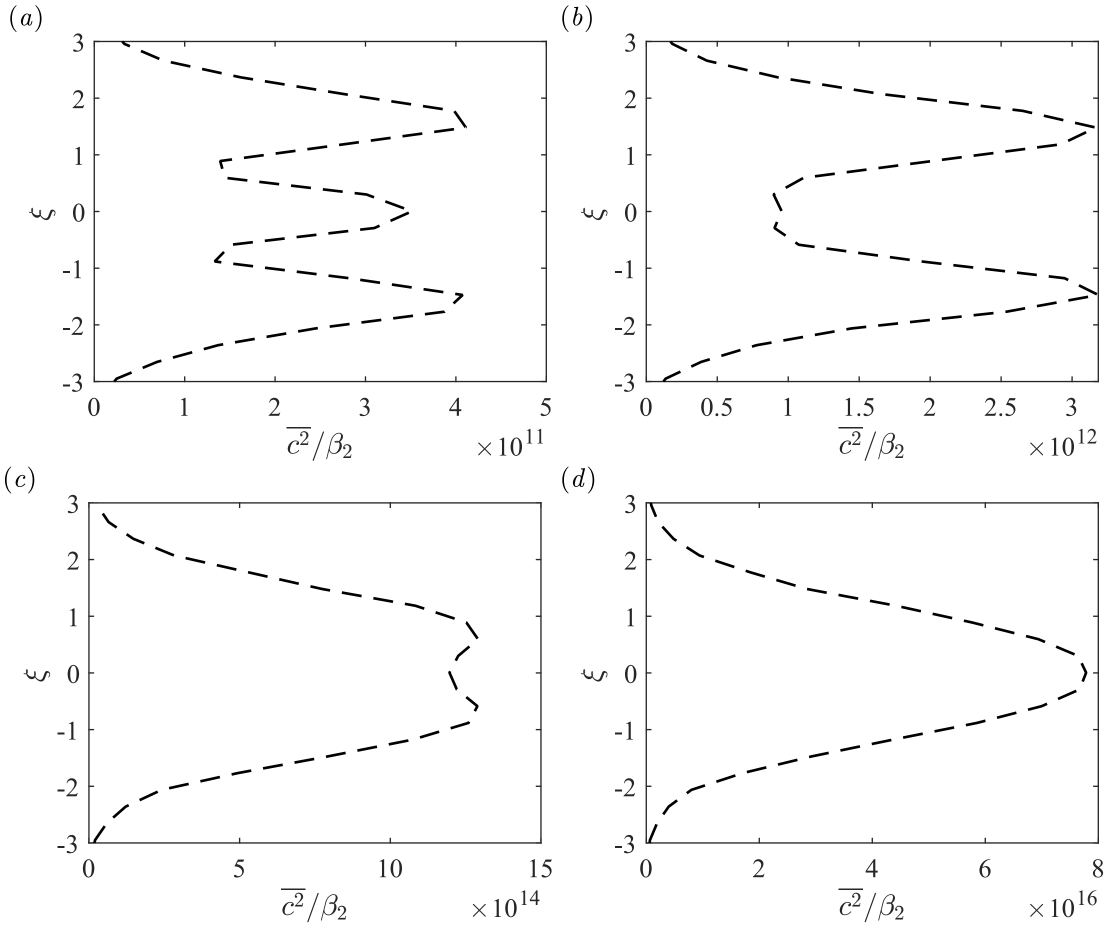


FIGURE 5.5: Influence of $\alpha$ in equation 5.7 on the shape of higher moment profiles. The input is the mean concentration $C$ at $S_x/\delta = 1$ and $S_z = 80$ mm of the neutral plume. (*a*) $\alpha = 1.31$. (*b*) $\alpha = 1.84$. (*c*) $\alpha = 5$. (*d*) $\alpha = 10$.

## 5.4 Summary

In this chapter, the investigation focused on the behaviour of higher-order moments of concentration fluctuations in neutral and buoyant plumes. Initially, the study explored the behaviour of the third and fourth-order normalised central moments, namely skewness, $Sk$, and kurtosis, $Ku$, respectively. The relationship between $Sk$ and $Ku$, as derived by Schopflocher and Sullivan (2005), accurately described our data. It is also found that profiles of $Sk$ and $Ku$ of concentration exhibit self-similar behaviour about the plume centreline.

Subsequently, the attention shifted towards higher-order central moments. It is observed that the profiles of the first six central moments exhibited Gaussian-like characteristics, similar to those of the mean and standard deviation. These findings provided further insight into the distribution of concentration within the plume.

Additionally, comparisons are made with the $\alpha - \beta$ model proposed by Chatwin and Sullivan (1990), which aimed to relate higher central moments to the mean value. The shape of the higher moment profiles indicated a potential dependence of $\alpha$ on downstream distance, contradicting the conclusion by Chatwin and Sullivan (1990) that $\alpha$ is constant. These results underscore the need for additional research to refine our understanding of the complex relationship between higher-order moments and the mean concentration.

The self-similarity observed in the first six moments also suggests the possibility of self-similarity in the probability density function of concentration. This aspect will be further discussed in chapter 6.

CHAPTER 6

# Probability density function of concentration

---

This chapter discusses the initial findings on the parameterisation of the high-concentration tails using data from plumes released at different source heights in a turbulent boundary layer. The data were acquired in a previous study, the relevant details are briefed in section 6.1 while the data analysis is the work of this thesis.

## 6.1 Experiment setup

A neutrally buoyant gas mixture (1.5% iso-butylene mixed in 98.5% Nitrogen) is released from a point source at different heights in a turbulent boundary layer. Further details of the facility and the experiments can be found in Talluru et al. (2017). Simultaneous measurements of velocity and concentration measurements are acquired. However, here, the only concern is with the concentration measurements. The instantaneous concentration downstream of the plume source is measured using a Photo-Ionisation Detector (PID) that is sensitive to the iso-butylene present in the release mixture and has a frequency response of 400 Hz. Multiple acquisitions are made across the plume with a sampling time of 300 sec for each position. The PID is calibrated before and after each experiment to account for background concentration and instrument drift. After applying the calibration technique outlined in Talluru et al. (2019a), the mean- and RMS-concentration profiles are found to agree well with the Gaussian (or Reflected-Gaussian) behaviour that is well-known (Talluru et al. 2017; Talluru et al. 2018). However, there is still a $\pm 3\%$ systematic error and $\pm 2\%$ repeatability error (Talluru et al. 2017). Here the concentration signals when the plume is released at $S_z/\delta = 32/\delta^+, 350/\delta^+, 0.1$, and 0.25, are examined, with $S_z$ being the source height and

$\delta = 0.31$ m being the boundary layer thickness. The measurements are acquired at a distance $S_x$ =0.5$\delta$, $\delta$, 2$\delta$, and 4$\delta$ downstream of the source.

## 6.2 Shape of PDF

Although various distributions are used in literature (e.g. Cassiani et al. 2020) to fit the full-signal probability density function (PDF) of measured concentration, none is appropriate for describing the full range of concentration signal. The fit quality, typically assessed by some measure such as the R-square, also depends on the fidelity of the experimental data and the range over which fitting is performed. Most experimental observations indicate that Weibull and gamma distributions describe the concentration PDFs better. The gamma distribution is given as,

$$p(\tilde{C}) = \frac{1}{\Gamma(k)\theta^k}\,\tilde{C}^{k-1}\,\exp\left(-\frac{\tilde{C}}{\theta}\right), \tag{6.1}$$

where $k$ is the shape parameter, $\Gamma(k)$ is the gamma function of $k$, and $\theta$ is the scale parameter.

Typically, PDFs of the instantaneous concentration, $\tilde{C}$, and instantaneous concentration normalised by its RMS, $\tilde{C}/\sqrt{\overline{c^2}}$, where ($c = \tilde{C} - C$, concentration fluctuations), are used as a variable (Nironi et al. 2015; Talluru et al. 2017). Since $\overline{c^2}$ varies across the plume, to compare the PDFs at two distinct locations, here the PDF of the instantaneous concentration, $\tilde{C}$, are studied. Figure 6.1 illustrates how well existing distributions describe $p(\tilde{C})$. For PDF at the plume centreline in figure 6.1 (*a*) & (*c*), gamma distribution describes well the entire range on both linear – log axes and linear – linear axes while the others fail to capture the characteristics partially or entirely. The shape of the PDF off-centreline in figure 6.1 (*b*) & (*d*) distinguishes from that at the centreline due to intermittency, therefore none of the existing distributions describe the PDF well.

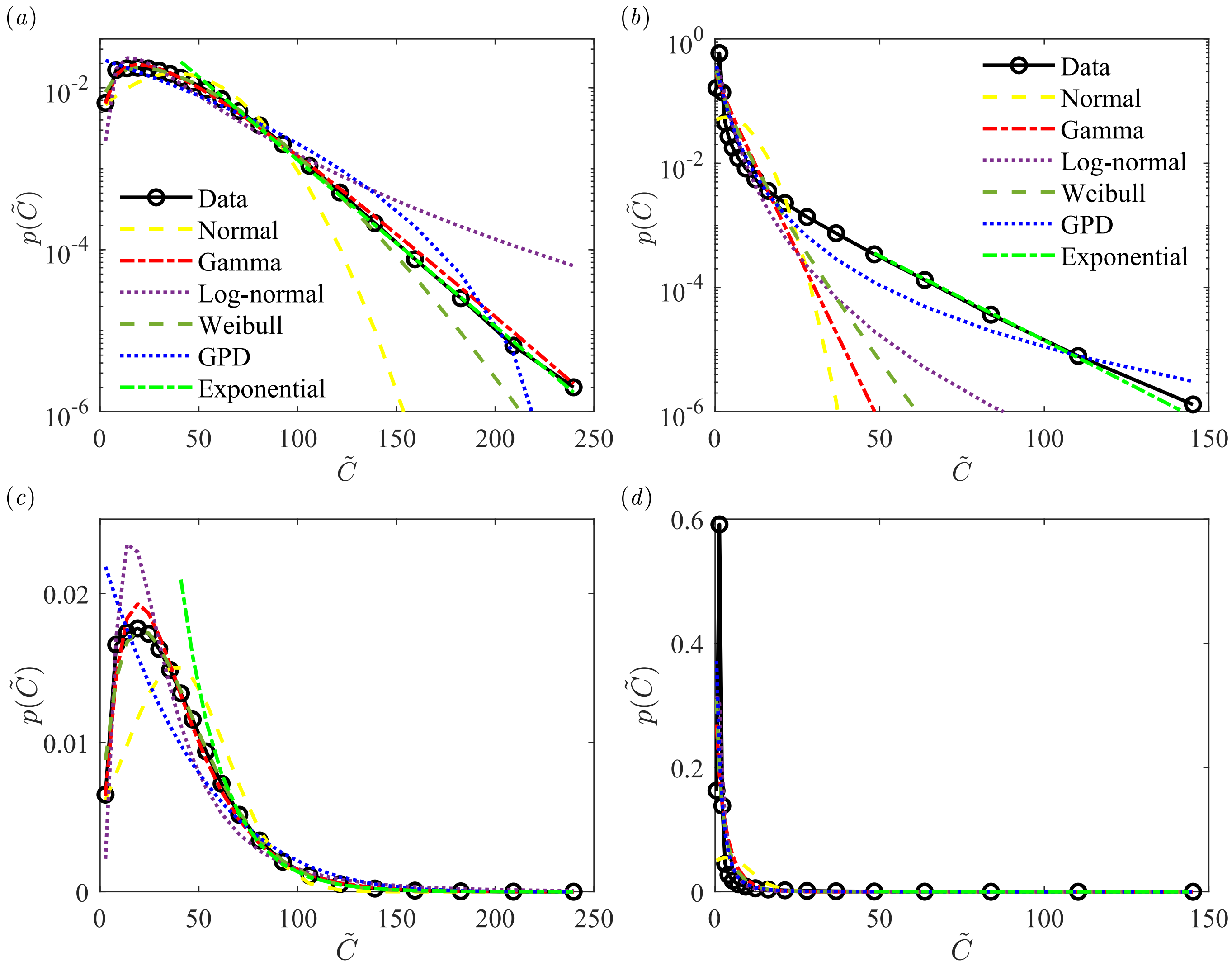


FIGURE 6.1: Comparison of distributions for the concentration PDF on linear – log axes and linear – linear axes for $S_z/\delta = 350/\delta^+$, $S_x/\delta = 1$. (*a*) & (*c*) at the plume centreline. (*b*) & (*d*) further from the plume centreline at $\xi \approx 1.2$. The distributions are defined in table 2.2.

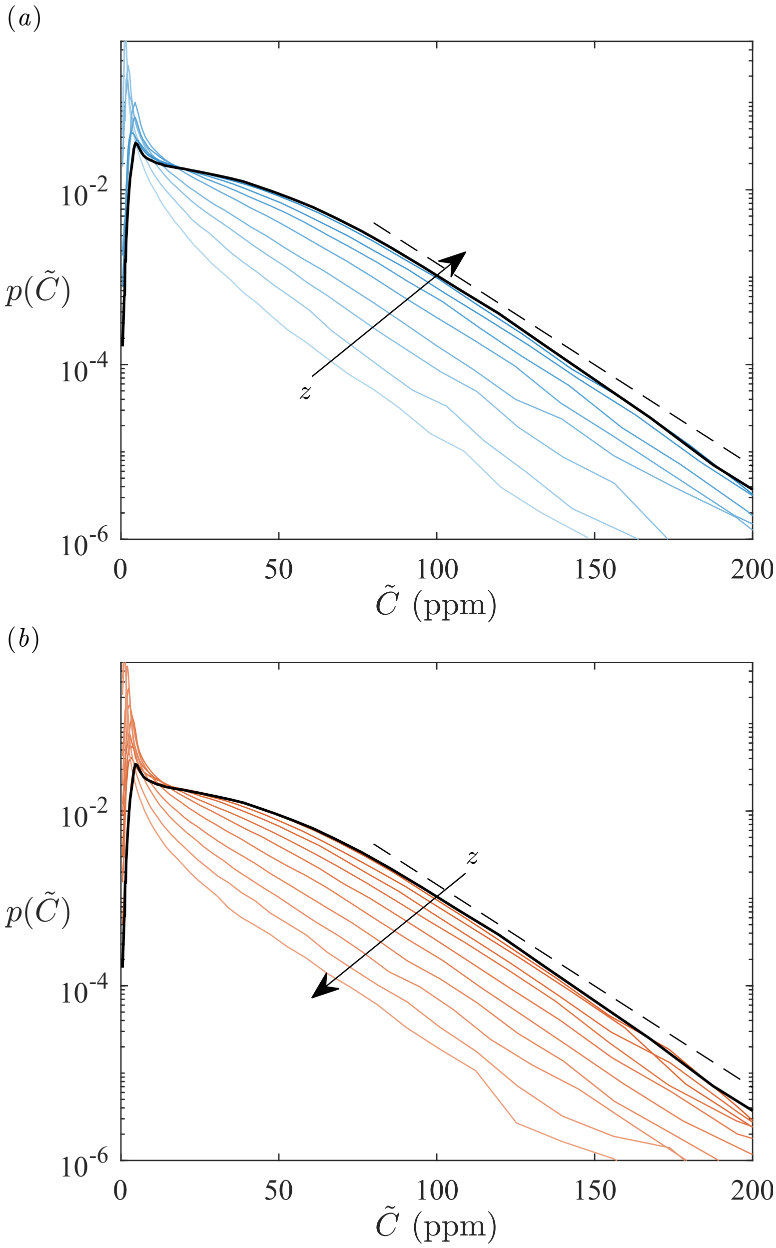


FIGURE 6.2: Probability density functions (PDFs) of the instantaneous concentration, $\tilde{C}$, for $S_x = 0.1\delta$, $S_z = 1\delta$. The solid black line represents the PDF on the plume centreline, the red lines are above the centreline, and the blue lines are the PDFs below the centreline. The dashed black line indicates the exponential behaviour.

Figure 6.2 plots the experimentally determined PDFs for $S_x = 0.1\delta$, $S_z = 1\delta$. The solid black line shows the PDF at the plume centreline. PDFs for measurements below the centreline are shown by red lines in figure 6.2($a$), whereas those for measurements above the centreline are shown by blue lines in figure 6.2(*b*). It is evident that the high-concentration tails have an exponential behaviour (a straight line on linear – log axes). Moreover, the indicative slope of the tail of each PDF appears to be similar too, *i.e.* they have similar decay exponent. Also, it is seen that in the vicinity of $\tilde{C} = 0$, the PDFs exhibit a sharp peak due to the presence of near-zero values in the signal resulting from the intermittent nature of concentration in a meandering plume. This peak behaviour near $\tilde{C} = 0$ cannot be modelled by the gamma distribution, even though it is suitable for higher concentration values. Since the gamma distribution is characterised by the exponential term in equation 6.1 at higher concentrations, consistent with the experimental observations, the fitting to the tail is simplified using a purely exponential function given as,

$$p(\tilde{C}) = A_1 \cdot \exp\left(-\frac{\tilde{C}}{\theta}\right), \ \tilde{C} > C' \tag{6.2}$$

where $C'$ is arbitrary. Two other studies focusing on the tail of the concentration PDF are by Mole et al. (2008) and Schopflocher (2001). They use Generalized Pareto Distribution (GPD) instead of an exponential function, defined as

$$p(\tilde{C}) = \frac{1}{\sigma}\left(1 + \xi\frac{\tilde{C} - \mu}{\sigma}\right)^{-1/\xi+1} \tag{6.3}$$

where $\sigma$ is the scale parameter, $\xi$ is the shape parameter, $\mu$ is the location parameter. A GPD fitted to the data as an example is plotted in figure 6.1. It can be observed that, though the prediction of a GPD seems to be acceptable on a linear – linear plot in figure 6.1 (*c*), it over-predicts in the range of approximately 75 ppm$< \tilde{C} <$200 ppm on a linear – log scale and under-predicts beyond that in figure 6.1 (*a*). Thus its prediction appears reasonably good on a linear plot; more stringent examination reveals that the GPD does not suitably represent the present data. The parameters $A_1$ and $\theta$ in equation 6.2 are determined using an iterative non-linear least squares method for each PDF, and their variation across the plume is shown in figure 6.2. The decay exponent, $\theta$, is plotted in figure 6.3(*a*) as filled symbols, whereas the coefficient, $A_1$, is plotted in figure 6.3(*b*). It is found that the tail of PDF for wall-normal locations near the edge of the plume on either side has a slightly different decay exponent. This indicates a decreased statistical convergence towards the plume edge (Chatwin

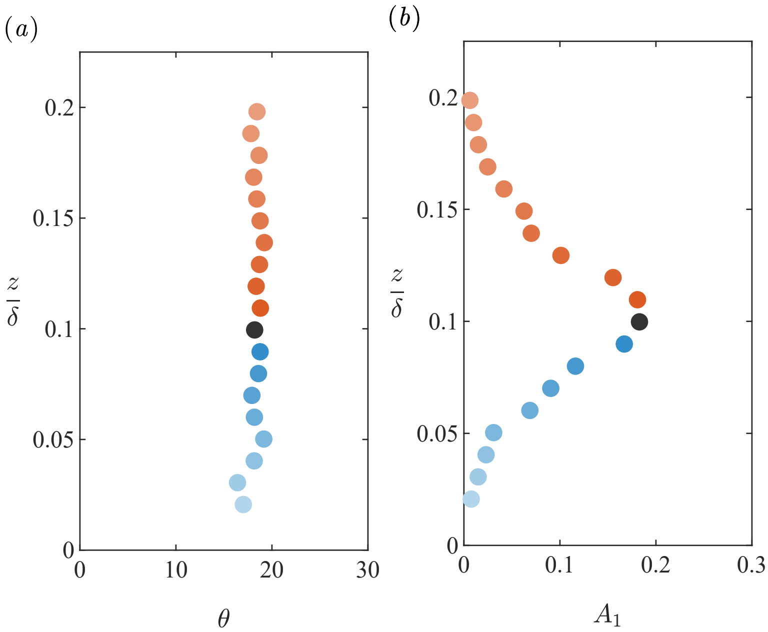


FIGURE 6.3: For $S_x = 0.1\delta, S_z = 1\delta$, (*a*) $\theta$, the decay exponent, from the exponential fit to the high concentration tail of the PDFs. The filled circles are for full-signal PDFs and the empty circles are from PDFs of peaks. (*b*) Coefficient $A_1$ for full-signal PDFs.

and Sullivan 1990; Yee and Chan 1997). Based on the above observation, figures 6.2 and 6.1 only includes the locations in the plume where $C > 0.1\,C_{\max}$, where $C_{\max}$ is the mean concentration at the plume centreline. It is seen that the decay exponent is almost constant across the plume, indicative of a statistical similarity for high-concentration events. This behaviour of the concentration tail is analogous to the similarity of concentration spectra observed by Talluru et al. (2019b). The median of decay exponents in figure 6.3(*a*) is used to plot the dashed line in figures 6.2(*a*) and 6.2(*b*), indicating that all tails could be modelled using a single $\theta$ value. Schopflocher (2001) and Mole et al. (2008) also found the shape parameter that they used to fit a GPD to the PDF tail to be constant. They argue that since molecular diffusion and the local turbulent structures responsible for convecting concentration are uniform across the plume. Further, it is noted that the distribution of coefficient $A_1$ has a Gaussian shape about the plume centreline, as illustrated in figure 6.3(*b*).

## 6.3 Spatial variation of distribution parameters

In this section, the analysis is extended to other source distances and source heights. Hereafter, $S_z/\delta = 32/\delta^+$ is referred to as Ground Level Source (GLS) and the other three $S_z$ as Elevated Sources (ES). It is observed that PDFs of all ES considered here exhibit a near-constant behaviour of the decay exponent, $\theta$ (as observed in figure 6.2*b*, although $\theta$ varies for each $S_z$ and $S_x$ combination). This implies that the PDFs of $\tilde{C}$ can be multiplied by a factor such that the tails of the PDFs for each source condition will collapse onto a single curve. Here this factor is denoted as $1/\mu$. It is obvious that $\mu \equiv A_1/A_{1,\text{CL}}$ from equation 6.2 and $\mu = 1$ at the plume centreline. Figure 6.4(*a*) shows the resulting PDFs for $S_x = 0.5\delta$ and $S_z = 0.1\delta$ and 6.4(*b*) plots those of $S_x = 4\delta$ and $S_z = 0.1\delta$. Similar to figure 6.2, the solid black line is the PDF at the plume centreline, and the dashed black line represents the average slope of the tail. Figures 6.4(*a*) and 6.4(*b*) demonstrate the self-similarity of PDF tails and the possibility of developing scaling laws for modelling. A representative decay exponent $\theta$ is determined for the plume released from four source distances and four source heights. Then the trend of the decay exponent is examined by plotting $\theta$ and $\theta_{\text{max}}$, where $\theta$ is the mean decay exponent, and $\theta_{\text{max}}$ is the decay exponent at the plume centreline. $\theta$ at the plume centreline and the mean $\theta$ across the plume is plotted against the downstream distance in figure 6.5. The plume width for all $S_z$ scatters vertically at the same $S_x$, especially prominent for $S_x/\delta$ =0.5 (red symbols) and $S_x/\delta$ =4 (black symbols). For a certain source height, as the plume grows wider downstream, the absolute difference between the mean concentration and the maximum instantaneous concentration lessens, leading to a steeper exponential tail and hence smaller value of $\theta$. Figure 6.6 illustrates the relationship between $\theta$ and the plume half-width calculated from the $\sigma_c$ profile, $\delta_{z,\sigma}$, for all ES. Firstly, the values of $\theta$ and $\theta_{\text{max}}$ for a given $S_z$ and $S_x$ combination are close, except for those of $S_x = 4\delta$ and $S_z/\delta = 350/\delta^+$ (black diamond symbol). A possible reason is that at further downstream distances from the source, the profile of a lower ES evolves to be similar to that of a GLS. Secondly, it is apparent that $\theta$ decreases in the streamwise direction and is proportional to $\delta_{z,\sigma}^{B_2}$, where $B_2$ is some exponent.

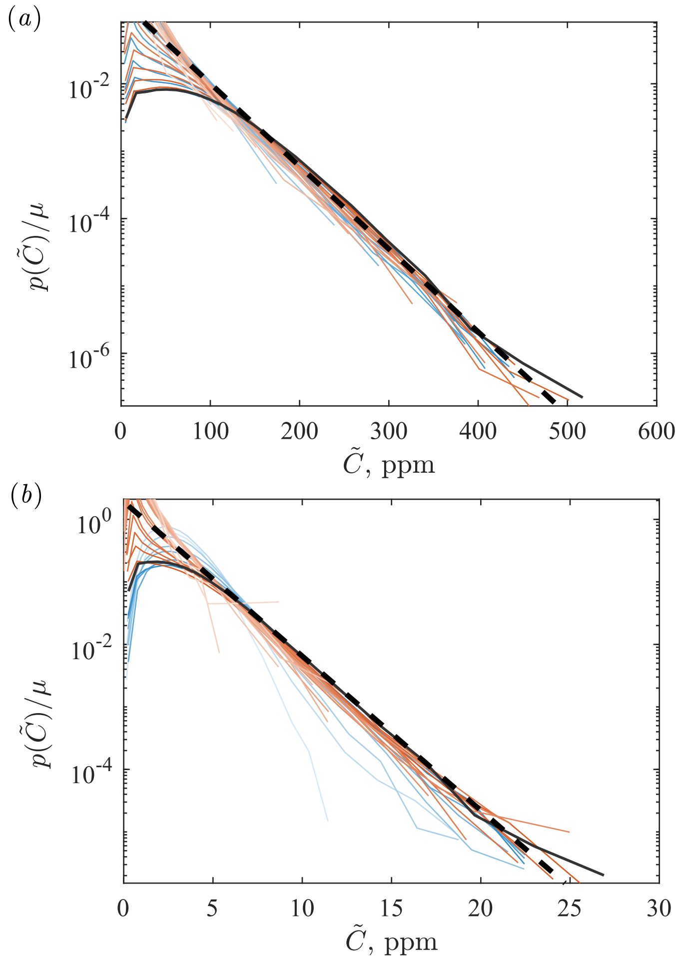


FIGURE 6.4: Collapsed PDFs of $\tilde{C}$ for (*a*) ES $S_x = 0.5\delta$, $S_z = 0.1\delta$. (*b*) ES $S_x = 4\delta$, $S_z = 0.1\delta$. The collapsed PDFs are obtained by dividing the original PDF $p(C)$ by $\mu$.

The other parameter in equation 6.2, $A_1$, shows a Gaussian-like behaviour, as plotted in figure 6.3(*b*). Thus $\mu$ is likely to be related to the mean concentration. Figure 6.7 plots $C/C_{\text{max}}$ vs $\mu$ in a log-log scale for all ES. It is observed that $\mu \propto (C/C_{\text{max}})^D$, where $D$ is some exponent. Again, decreased statistical convergence is observed for $S_x = 4\delta$ and $S_z/\delta = 350/\delta^+$ here (black diamond symbol). In contrast to the above observation, the decay exponent $\theta$ varies significantly across the plume for a GLS. The change in slope for each PDF is evident in figure 6.8(*a*) and consequently, the PDF tails do not collapse to a single curve after being scaled. Instead the profile of $\theta$ for GLS in figure 6.8(*b*) resemble the mean concentration profile for the GLS. It is inferred that this behaviour of changing decay exponent might be due to the wall effect and further analysis is needed to characterise this behaviour.

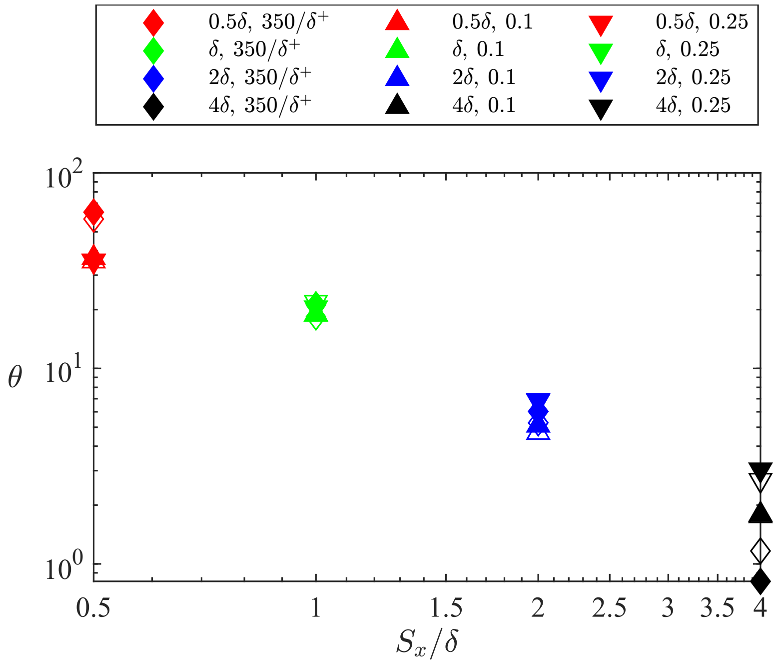


FIGURE 6.5: $\theta$ vs $S_x/\delta$ for all ES. The first number in the legend is the source distance, $S_x$, and the second is the source height, $S_z/\delta$. Solid symbols are centreline PDFs and hollow ones are the average slopes for all PDFs.

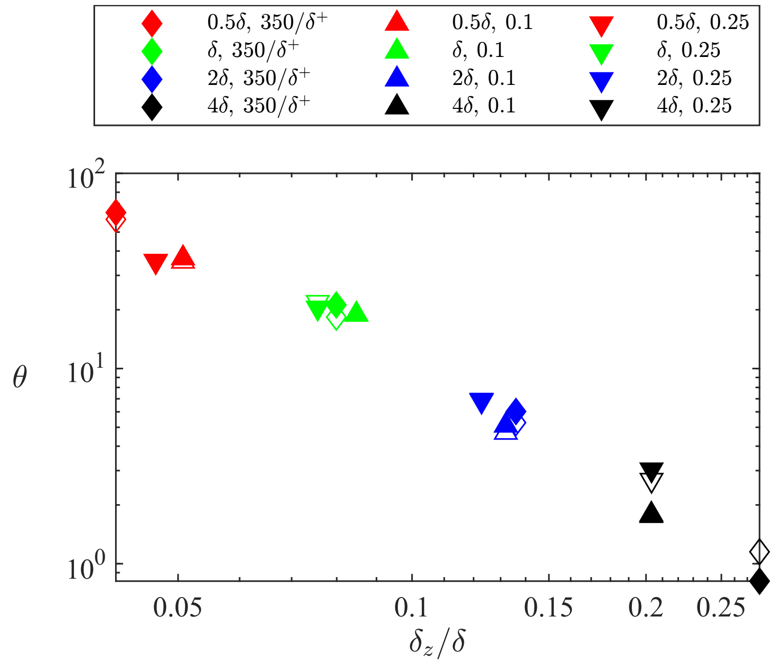


FIGURE 6.6: $\theta$ vs $\delta_{z,\sigma}$ (half-plume width) for all ES. The first number in the legend is the source distance, $S_x$, and the second is the source height, $S_z/\delta$. Solid symbols are centreline PDFs and hollow ones are the average slopes for all PDFs.

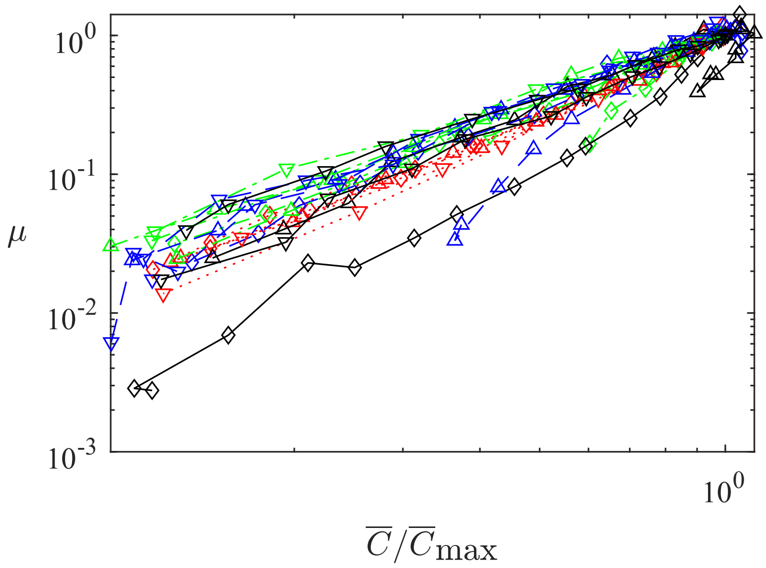


FIGURE 6.7: The factor used to collapse $p(\tilde{C})$, $\mu$, plotted against $C/C_{\text{max}}$ for all ES. For legend refer to figure 6.6.

## 6.4 Extreme event analysis

In this section, the PDFs for the extreme values in the concentration signal are examined. While the PDF of the entire data set provides a comprehensive view of the concentration distribution, it does not explicitly illustrate the intervals between occurrences of extreme concentration events. Understanding these intervals is crucial for determining the timing and frequency of such extreme events, forming a fundamental part of risk assessment and preparedness. Similar methodologies are used in fields like seismology, meteorology, and hydrology to anticipate extreme events such as earthquakes, storms, and floods over specific durations. To effectively evaluate associated risks and develop efficient preventive and mitigative strategies, adopting approaches from these fields to examine the PDF of extreme concentration events becomes imperative. Two approaches are adopted. First, all the local maxima that are above a threshold are examined and second, the local maxima over multiple segments of the signal are analysed.

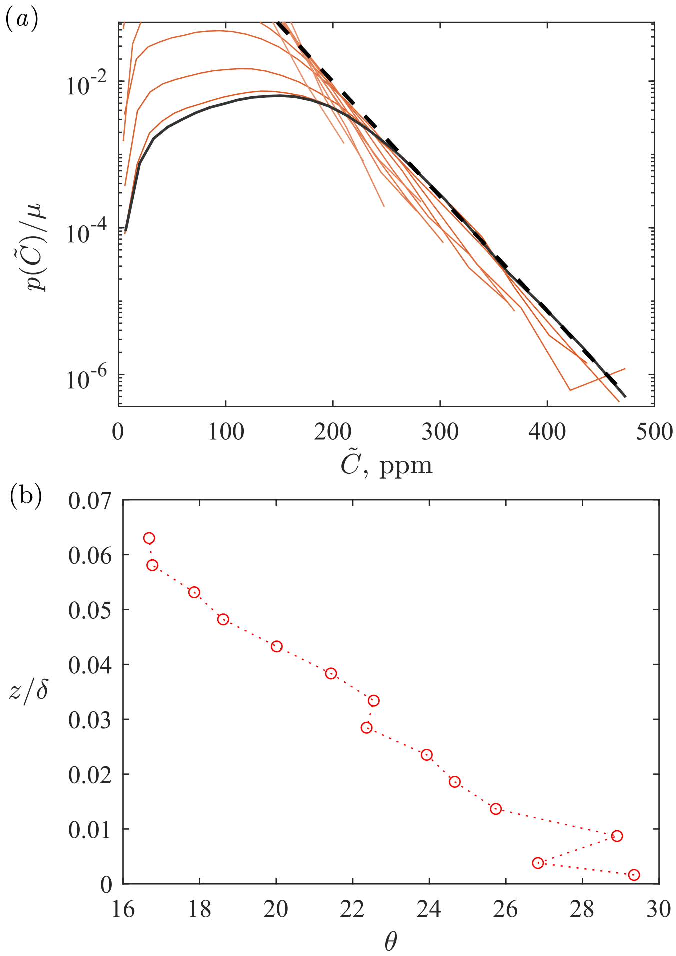


FIGURE 6.8: ($a$) Collapsed PDFs of $\tilde{C}$ for a GLS, $S_x = 0.5\delta$, $S_z/\delta = 32/\delta^+$. ($a$)$\theta$ calculated for each PDF in the cross-plume direction.

### 6.4.1 Peak over threshold

The local maxima (see figure 6.9$a$) is determined in the instantaneous signal at a height $z$ in the boundary layer such that the peak values ($\tilde{C}_{p,1}$) are larger than the local mean. Only these maxima are collected to calculate a PDF, which is distinguished from PDFs of all concentrations above a threshold that is a truncated PDF of the full-time series. The PDFs for these peak values are plotted in figure 6.9($b$) and similar to the full-signal PDFs, the PDFs for the peaks also exhibit exponential behaviour at high concentrations. The decay exponent is evaluated for these PDFs, plotted as hollow symbols in figure 6.3($a$), and is close to the values for the full-signal PDFs (solid symbols in figure 6.3($a$)). It is also found that the decay

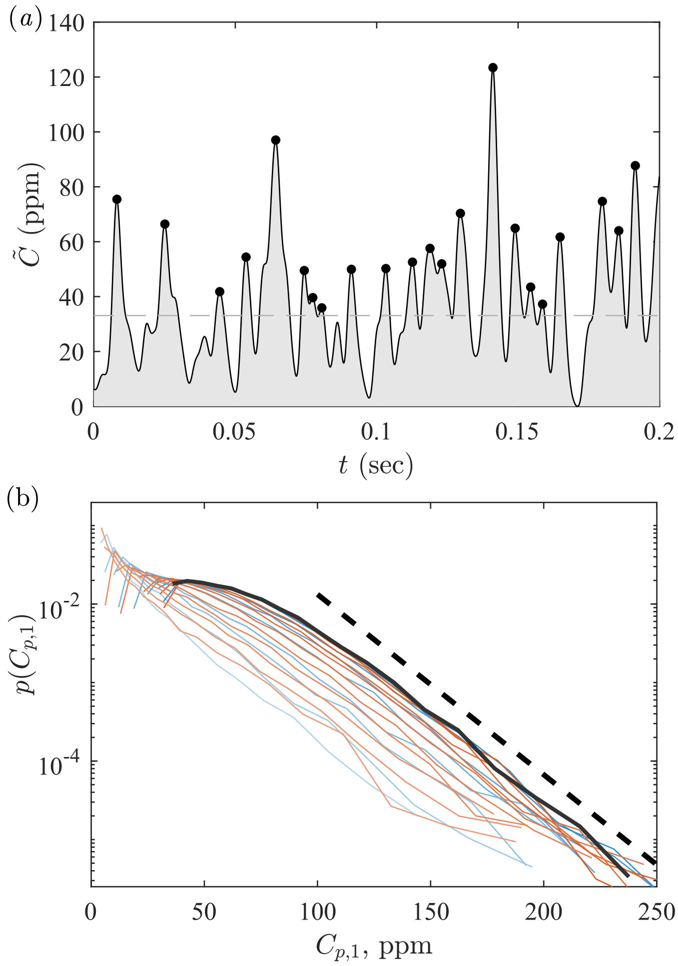


FIGURE 6.9: (*a*) Instantaneous concentration measured for a 0.2-sec period with identified peaks, $\tilde{C}_{p,1}$. The grey dashed line is the local mean concentration. (*b*) Probability density functions for peak values only for $S_x = 1\delta$, $S_z = 0.1\delta$. The solid black line represents the PDF on the plume centreline, the red lines are above the centreline, and the blue lines are the PDFs below the centreline. The dashed black line indicates the exponential behaviour.

exponent for the PDFs of the peaks is nearly constant, indicating self-similarity of these statistics.

### 6.4.2 Maxima over a period

The probability of maxima in a fixed time period is commonly studied in meteorology and hydrology, e.g. monthly maxima and annual maxima. Typically, Generalised Extreme Value (GEV) distributions are then fitted for the prediction of extreme events when limited data are available. For example, in the field of wind engineering, the Weibull distribution is more appropriate for the probability distribution of annual maximum wind speed (Holmes and Bekele 2021). A similar approach is applied to the concentration measurements, where the signal at any location is acquired for 300 seconds and thereafter this sampling time is divided into segments of pre-defined duration. The pre-defined duration is the integral time scale for concentration, $\tau_c$, which is found from the auto-correlation function as defined by Talluru et al. (2018, equation 3.4 in). The signal is then divided into segments, each of duration $\tau_c$, and the maximum concentration from each segment is collected. This method is demonstrated in figure 6.10($a$), where the vertical dotted lines represent the time-intervals and the local maxima, $\tilde{C}_{p,2}$, in the respective intervals are indicated using red dots. The corresponding PDFs of $\tilde{C}_{p,2}$ are plotted in figure 6.10($b$). As anticipated, these PDFs also have an exponential tail, with a decay exponent similar to that for $p(\tilde{C})$ and $p(\tilde{C}_{p,1})$ in figures 6.2($a$,$b$) and 6.9($b$), respectively.

The PDFs of $\tilde{C}_{p,2}$ in figure 6.10($b$) have the same shape but appear to be shifted. The PDFs in figure 6.10($c$) are shifted to the left compared to the relative to those of $p(\tilde{C}_{p,2})$ in 6.10($b$) by the corresponding mean values, $\overline{\tilde{C}_{p,2}}$. The PDFs plotted in figure 6.10($c$) now show a good collapse. Although the results presented in figure 6.10($b$) and 6.10($c$) only show the PDFs of $\tilde{C}_{p,2}$ for one source location, the PDFs for other source heights and source distances also exhibit this behaviour.

Since the shape of the PDFs is the same, there are two ways to parameterise the PDF. The first method is to only characterise the $p(\tilde{C}_{p,2})$ at the centreline using the parameters of a gamma distribution and use the horizontal shifts $\overline{\tilde{C}_{p,2}}$. This enables the characterisation of the $p(\tilde{C}_{p,2})$ away from the centreline as a function of the distribution of $p(\tilde{C}_{p,2})$ on the plume centreline. The second approach is to obtain the gamma parameters for the PDFs at each wall-normal distance and relate the parameters to the wall distance. Both methods require three parameters. Here, the parameters obtained via the second method are presented since the measurement of $\overline{\tilde{C}_{p,2}}$ is difficult in practice.

The entire range of the PDFs can be described well by a gamma distribution (the coefficient of determination of the fit, R-square, is mostly larger than 0.98). In contrast, for $p(\tilde{C})$, a peak

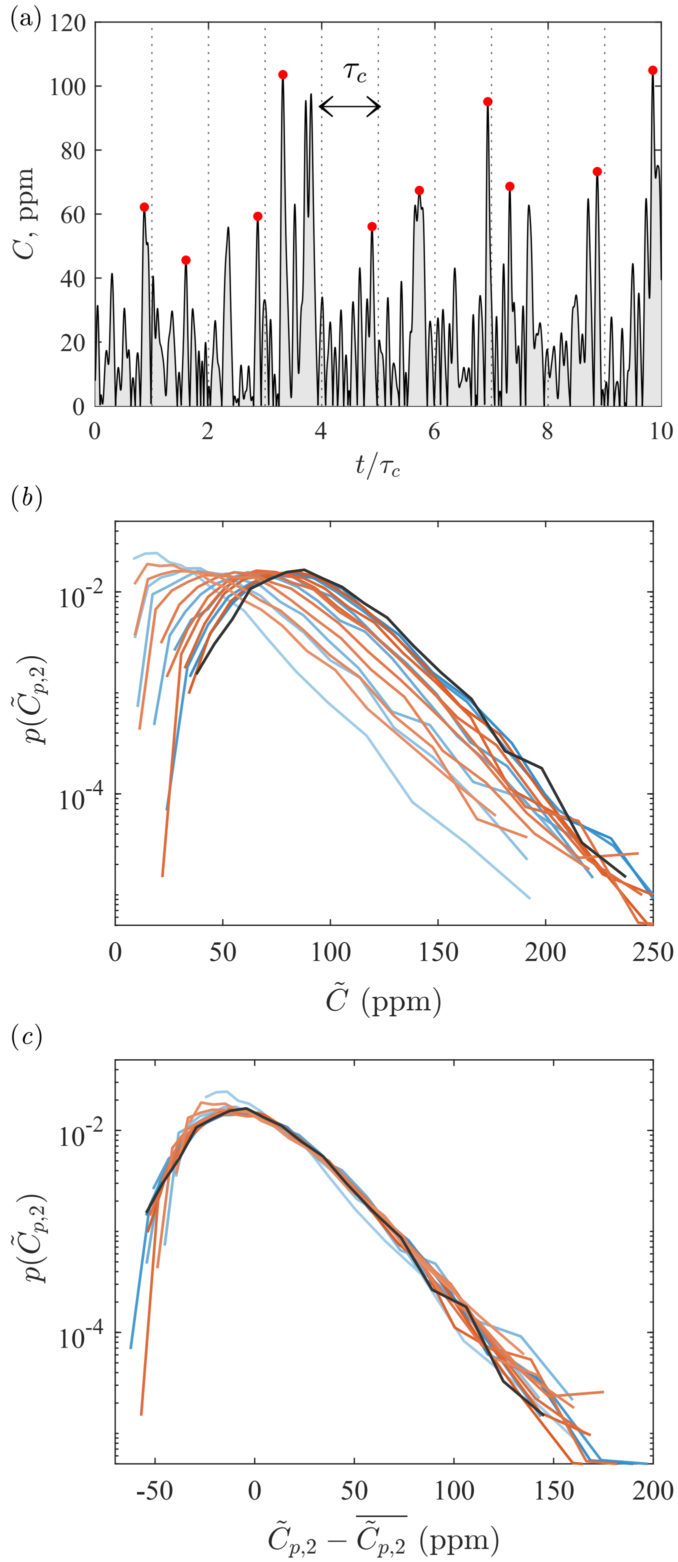


FIGURE 6.10: (*a*) Instantaneous concentration measured for a period of 10 $\times$ time scale for concentration, $\tau_c$, with identified peaks over each segment of $\tau_c$, $\tilde{C}_{p,2}$. (*b*) Probability density functions for peak values in each bin for $S_x = 1\delta$, $S_z = 0.1\delta$. The dashed line represents the decay exponent calculated from $p(\tilde{C})$, in this case, the green triangle in figure 6.6. (*c*) Shifted probability density function in (*b*) where the shift equals the mean of peaks. For both (*b*) and (*c*), the meaning of curves of different colours is the same as figure 6.9 (*b*).

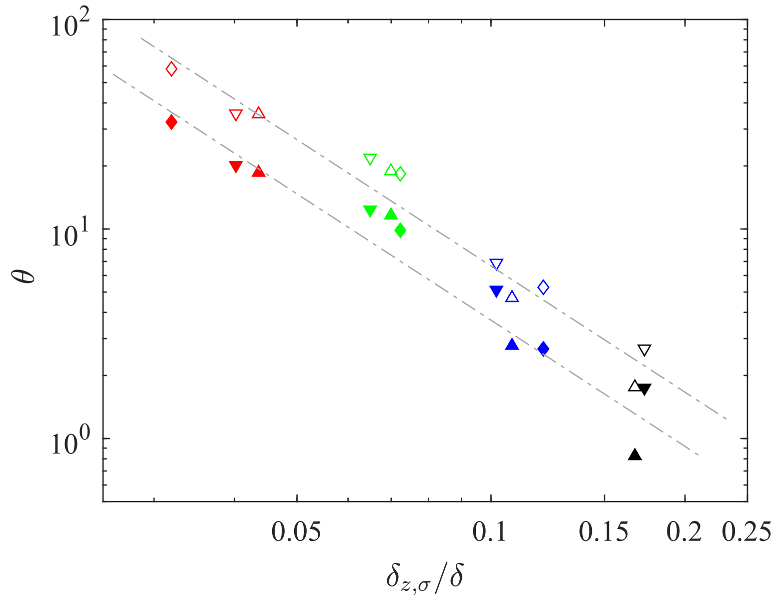


FIGURE 6.11: Decay exponent of the tail of the PDF vs plume half-width. Hollow symbols are for $p(\tilde{C})$ and solid symbols are for $p(\tilde{C}_{p,2})$.

is observed close to $\tilde{C} = 0$ and only the tail can be described by an exponential equation. The parameters of the gamma distribution of $p(\tilde{C}_{p,2})$ exhibit similar behaviours as that of the tail of $p(\tilde{C})$. The profiles of the shape factor, $k_{p,2}$, exhibit a Gaussian behaviour and hence are plotted similarly in figure 6.12 as $\mu$ in figure 6.7. Similarly $k \propto (C/C_{\text{max}})^{D'}$, where $D'$ is some exponent. However, $k$ does not collapse onto the same curve as for $(\tilde{C})$ in figure 6.7 because $\mu$ is a quantity defined relative to the centreline $p(\tilde{C})$ while $k$ is the absolute shape parameter of $p(\tilde{C}_{p,2})$. The decay exponent, $\theta_{p,2}$, is also constant across the plume. Therefore the average $\theta_{p,2}$ for each source condition is plotted in figure 6.11 to compare with $\theta$ of $p(\tilde{C})$. It can be observed that $\theta_{p,2}$ also is also proportional to $\delta_{z,\sigma}^{B_2}$, the value of which is very close to $B_2$. Furthermore, $\theta_{p,2}$ is approximately 1.5 to 2 times smaller than $\theta$ of the full signal PDF. This is due to the fact that the input of $p(\tilde{C}_{p,2})$ consists of mainly larger values and concentration values close to 0 are excluded.

## 6.5 Summary

The results presented here arise from extensive measurements and thus bring new information to the already extensive literature on PDFs for scalar concentration. The PDFs of concentration

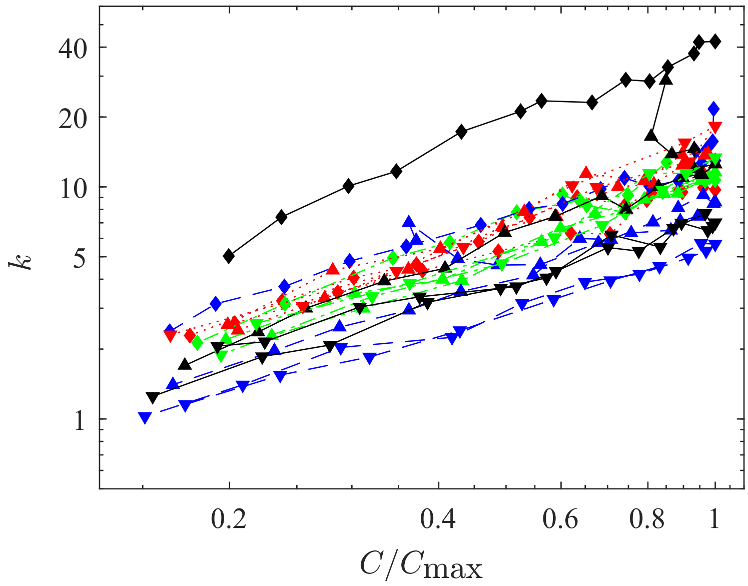


FIGURE 6.12: Scale parameter of the PDF of $\tilde{C}_{p,2}$ vs $C/C_{\max}$. Legend same as figure 6.6.

measured for varying source heights and source distances exhibit statistical similarity across the plume. Evidence is presented for the decay exponents to be invariant across the plume through the PDFs for $p(\tilde{C})$, $p(\tilde{C}_{p,1})$, and $p(\tilde{C}_{p,2})$. A novel finding is in the fact that the decay exponent is related to the plume half-width.

The spread of passive scalar is dominated by two mechanisms: turbulent mixing and molecular diffusion (Gifford 1959). Large concentration events in the plume are thought to reside on thin *strands* or *sheets* and are caused by local turbulence (Yee and Chan 1997). Molecular diffusion is also significant for these high-concentration patches due to local high spatial gradients. Given that the plume width relative to the boundary layer thickness is small, the influence of the local turbulence would be for the whole plume. Thus the two mechanisms for the spread of concentration are persistent across the plume resulting in high-concentration events having the same decay exponent in the corresponding PDFs.

Here only the high-concentration tail of the PDFs is studied, and thus the behaviour of low-level concentration is not examined. The analysis is not aimed towards describing the full range of concentration fluctuations, as typically done in past studies. The exponential tail of the PDFs is undoubtedly evident in these measurements due to the long sampling times.

This behaviour suggests that the appropriate functional form for the full-scale PDF, e.g. the gamma distribution asymptotes to an exponential behaviour for large concentrations and thus simplifies the prediction of high-concentration events. Similar observations have been made by Schopflocher (2001). However, it should be noted that the exponential distribution also results in finite probability, no matter how small, for concentration magnitudes that are above the source concentration. This is unrealistic due to the ever-present molecular diffusion(Chatwin and Sullivan 1990; Munro et al. 2001; Mole et al. 2008). When concentration is released, the velocity field transports the concentration in the forms of sheets and strands, in which the concentration is the same as the source concentration without molecular diffusion. However, due to molecular diffusion, matter spreads from high to lower concentration hence the concentration within strands and sheets is less than the source concentration. Another practical interest is to model the 90$^{\text{th}}$ and 99$^{\text{th}}$ percentile, $C_{90}$ and $C_{99}$, which are studied in Fackrell and Robins (1982) and Efthimiou et al. (2016). The exponential tail alone cannot be used to predict $C_{90}$ or $C_{99}$ since it does not describe the possibility of low concentrations. However, the Gamma distribution can be used to predict $C_{99}/\sigma_c$. The Gamma distribution requires two parameters to describe the full PDF, which can be calculated from $C$ and $\sigma_c$. With the full PDF, one can calculate the Cumulative Density Function (CDF). The calculation is numerical since the CDF contains a Gamma function. $C_{99}/\sigma_c$ is relatively constant for $-1 < \xi < 1$, ranging between 4.6 and 4.9 experimentally, and the prediction differs by less than $6\%$. The values are slightly higher than Csanady (1967)'s prediction of 4.3 to 4.6 using Poisson distribution.

Efforts are also ongoing to reconcile the observations made for concentration PDFs in this paper with the results for the concentration spectra by Talluru et al. (2019b) and the phenomenological model for the role of large-scale velocity structures by Talluru et al. (2018). As such, these statistical variations (particularly for figures 6.6 and 6.7) are not yet parameterised to model the probability or for predictions.

CHAPTER 7

# Scalar fluxes

---

Studying the behaviour of scalar fluxes is important for two reasons. Firstly, they are the unknown terms in the Reynolds-averaged transport equation. the behaviour of scalar fluxes might shed light on how the equation can be closed. Secondly, from a physical point of view, scalar fluxes tell us how velocity fluctuations transport the scalar.

This chapter focuses on the vertical scalar fluxes, $\overline{wc}$. Its downstream evolution and self-similarity are studied. A novel non-dimensional eddy diffusivity is proposed. The advantages and drawbacks of this model are discussed. The second section briefly documents the behaviour of the streamwise scalar fluxes, $\overline{uc}$.

## 7.1 Vertical scalar fluxes

### 7.1.1 The theoretical shape of $\overline{wc}$

The theoretical shape of $\overline{wc}$ of an elevated source is examined first. At the plume centreline, $\overline{wc} = 0$ due to symmetry. Far away from the centreline, outside the plume, $\overline{wc} = 0$ as concentration vanishes (Wyngaard 2013). The location of the plume centreline, $z_{\mathrm{CL}}$, is defined as the height of the maximum concentration variance, $\sigma_{c,\ \mathrm{max}}$. Positive effluent of concentration ($+c$) moving upwards ($+w$) and negative concentration fluctuations ($-c$) from above ($-w$) result in $\overline{wc} > 0$ above $z_{\mathrm{CL}}$ (Wyngaard 2013). Similarly, $\overline{wc} < 0$ below $z_{\mathrm{CL}}$. Overall, the profiles have a reverse S-shape. In a turbulent boundary layer, the reverse S-shape is not symmetric about the plume centreline since the lower half of the plume generally experiences more shear. This is because $\overline{w^2}$ is responsible for spreading the plume in the vertical direction and is more prominent at low $z$ in the turbulent boundary layer.

The reverse S-shape is confirmed experimentally by (Fackrell and Robins 1982; Legg et al. 1986; Talluru et al. 2017). In the case of a ground-level source, only the upper half of $\overline{wc} > 0$ of the S-shape is observed. Fackrell and Robins (1982) observed experimentally the maxima and zeros of $\partial C/\partial z$ is roughly corresponding to those of $\overline{wc}$. Furthermore, the $\overline{wc}$ of an elevated source evolves to a shape similar to that of a ground-level source (Fackrell and Robins 1982), similar to the behaviour of $C$ and $\sigma_c$.

Typically, the gradient-diffusion hypothesis is used to model the flux term, *i.e.* $\overline{wc} = \kappa_z(\partial C/\partial z)$, analogous to the turbulent-viscosity hypothesis of Reynolds-averaged Navier-Stokes equation. It is well-known that the plume spread is different if the source is placed in different regions of the boundary layer. Fackrell and Robins (1982) observed that $\kappa_i$ increases with downstream distance for elevated sources. Hence it is not straightforward to specify distinct $\kappa_z$ for each source location. Nonetheless, they highlighted the possibility of the gradient-diffusion hypothesis being relevant due to the consistency between the locations of maximum and zero values in the vertical velocity $\overline{wc}$ and the vertical concentration gradient $\partial C/\partial z$.

The present study aims to undertake a systematic study of the behaviour of $\overline{wc}$ from experimental data to model eddy-diffusivity in different regions of the flow to close the approximate transport equation.

### 7.1.2 Evolution of dimensional $\overline{wc}$

Figures 7.1($a$) and 7.1($b$) plot the dimensional magnitude of $\overline{wc}$ for a ground-level source and an elevated source. The magnitude of $\overline{wc}$ decreases with downstream distance as the plume spreads and concentration disperses. The overall trend for the three density ratios and all $S_z$ (though $S_z = 40$ mm is not shown in figure 7.1($b$) is similar to the theoretical shape discussed in the previous section and that observed experimentally by Fackrell and Robins (1982). For both GLS and ES, before fully mixed ($x/\delta \leq 2$), $\overline{wc}$ is more negative for the heavy case than for the neutral and light case. In figure 7.1($a$), $\overline{wc}$ of the ground-level source varies in magnitude for each $S_x$, but the overall shape is similar to the upper half of

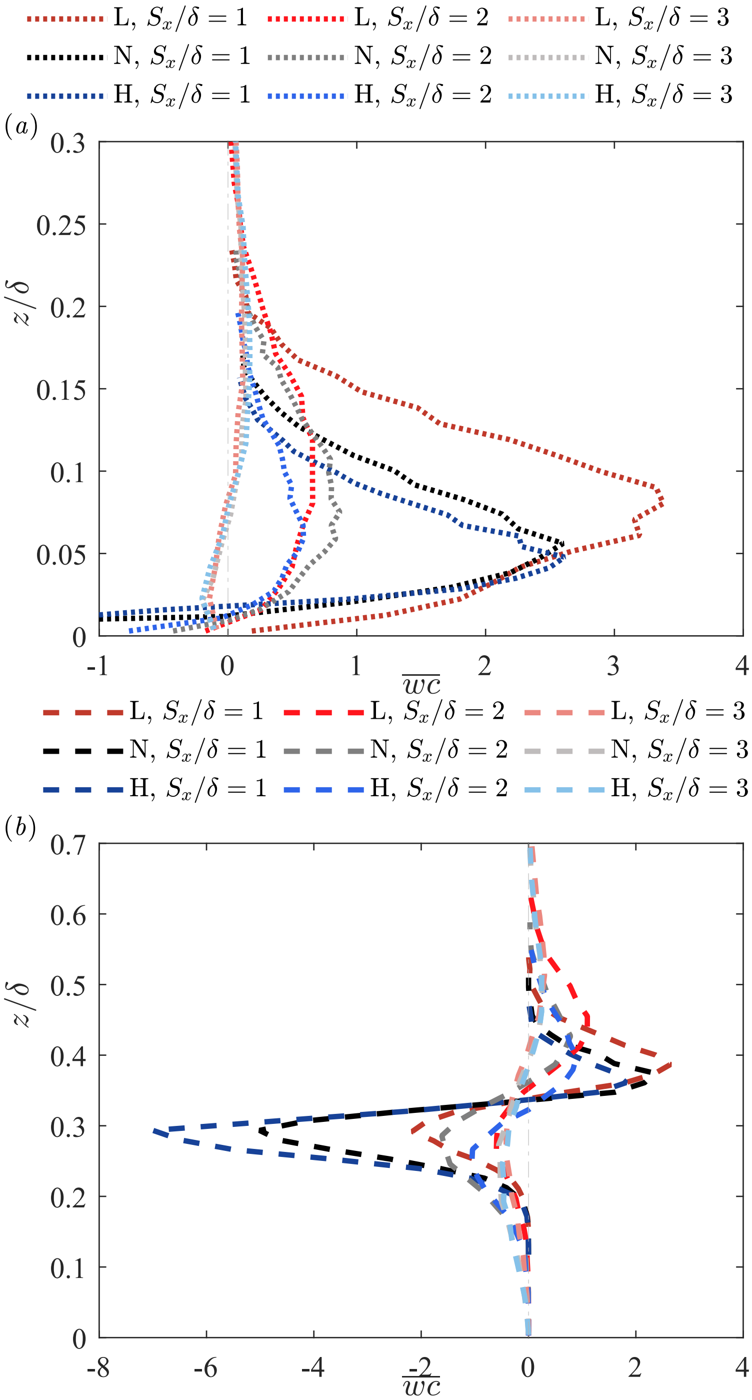


FIGURE 7.1: Vertical fluxes $\overline{wc}$ at three downstream locations, $S_x$, for (*a*) ground level source (*b*) $S_z = 80$ mm.

the reverse S-shape described earlier. Closer to the wall, $\overline{wc}$ approaches near-zero for $S_x = \delta$ and $2\delta$ but not for $S_x = 4\delta$. However, at $S_x = 4\delta$, $\overline{wc}(z = 0) \neq 0$, which is not possible due to the no-slip condition. This is likely due to the detection limit of the concentration sensor (Photo-ionisation detector) at small concentrations and the finite probe size that limits measurements at $z = 0$. In figure 7.1($b$), the profile of $\overline{wc}$ corresponds to the reverse S-shape. The height where $\overline{wc} = 0$ for each density ratio and downstream location differs since the lighter plume tends to rise and the heavier plume plunges relative to the source height.

### 7.1.3 Self-similarity of $\overline{wc}$

Since the profile exhibits symmetrical behaviour about the plume centreline, the vertical distance relative to the location of the plume centreline, $z_{\mathrm{CL}}$, is normalised using plume half-width calculated from $\sigma_c$, $\delta_z$: $\xi_\sigma = (z - z_{\mathrm{CL}})/\delta_{z,\sigma}$. The horizontal axis is normalised using local standard deviation, $\sigma_w$ and $\sigma_c$ since $\overline{wc}$ is a second-order statistic. Upon normalisation, there is a reasonable collapse of $\overline{wc}$ profiles in figure 7.2($a$) and 7.2($b$). The overall trend of the aforementioned reverse S-shape can be observed for the elevated sources in figure 7.2($b$). The heights where $\overline{wc} = 0$ for each profile are close to the centreline ($\xi_\sigma = 0$). Normalising $\overline{wc}$ using local $\sigma_w$ and $\sigma_c$ eliminates asymmetry observed in figure 7.1($b$) due to shearing of velocity field and varying mean concentration.

The normalised $\overline{wc}$ for the ground-level sources resembles the upper half of the elevated sources ($\xi_\sigma > 0$), consistent with the theoretical shape and past studies. For both ES and GLS, the $y$-axis intercept is not always zero, which contradicts the theory that $\overline{wc} = 0$ at the centreline, which will be discussed later.

In the original gradient model as equation 2.7, the dimensional $\overline{wc}$ is related to the gradient of the mean concentration profile. Naturally, the normalised $\overline{wc}$ plotted in figure 7.4 can also be related to the gradient of the normalised profile of $\sigma_c$. The reason why the gradient of $C$ is not used will be explained in the next section. The normalised profiles of $\sigma_c$ are plotted in figure 7.3($a$), and the derivative of standard Gaussian is plotted in figure 7.3($b$). The derivative is an S-shape, symmetrical about the vertical axis with the normalised $\overline{wc}$, though the magnitude is different. Hence a new model of scalar flux is proposed,

$$\frac{\overline{wc}}{\sigma_w \sigma_c} = \kappa_\sigma \frac{\partial(\sigma_c/\sigma_{c,\,\mathrm{max}})}{\partial \xi_\sigma} \tag{7.1}$$

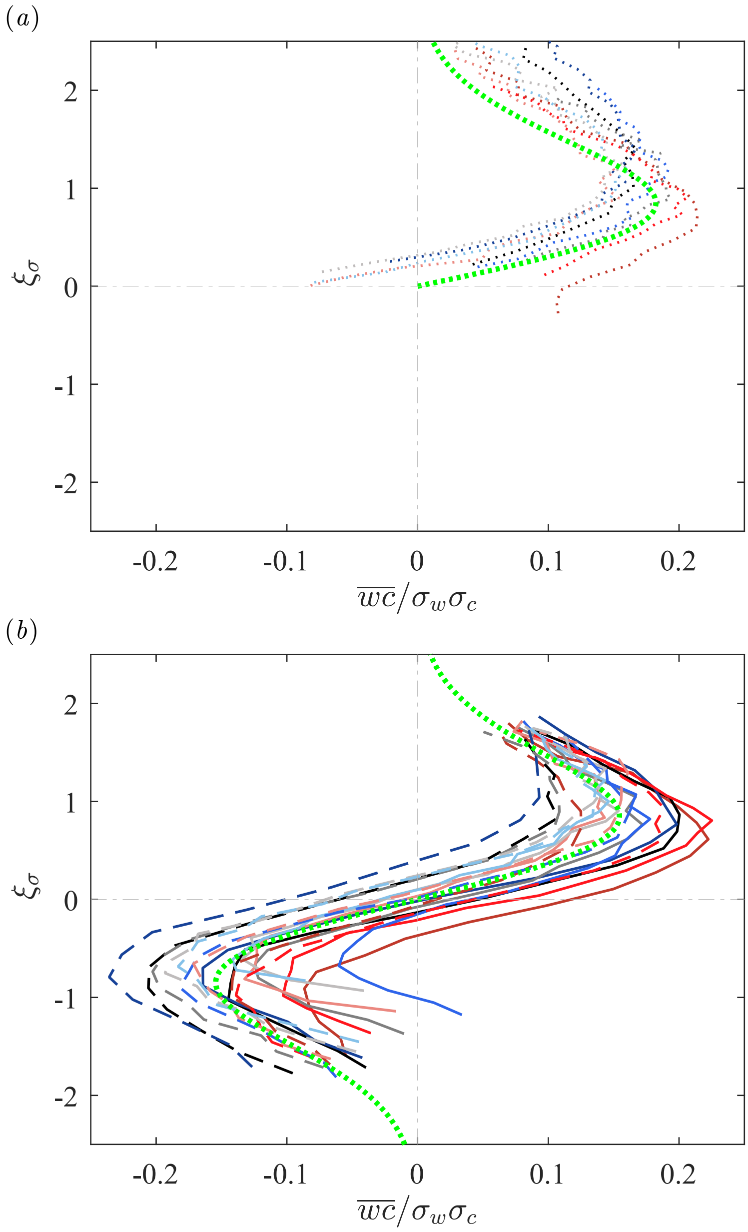


FIGURE 7.2: Normalised vertical fluxes, $\overline{wc}/\sigma_w\sigma_c$, at three downstream locations, $S_x$, for (*a*) the ground level source (*b*) $S_z = 40$ mm and 80 mm. The green dotted lines are $\kappa_\sigma \dfrac{\partial(\sigma_c/\sigma_{c,\,\mathrm{max}})}{\partial \xi_c}$ in equation 7.1. Legend same as figure 4.1.

Note that $\kappa_\sigma$ is a non-dimensional parameter and not eddy-diffusivity. In the current study, $\kappa_\sigma \approx -0.18$. The green dashed lines in figure 7.2 are the right-hand side of equation 7.1. They describe the trend for $\overline{wc}/\sigma_w\sigma_c$ well for both elevated source and ground level source, though some scatter is observed. Notably, the dotted lines capture several important characteristics

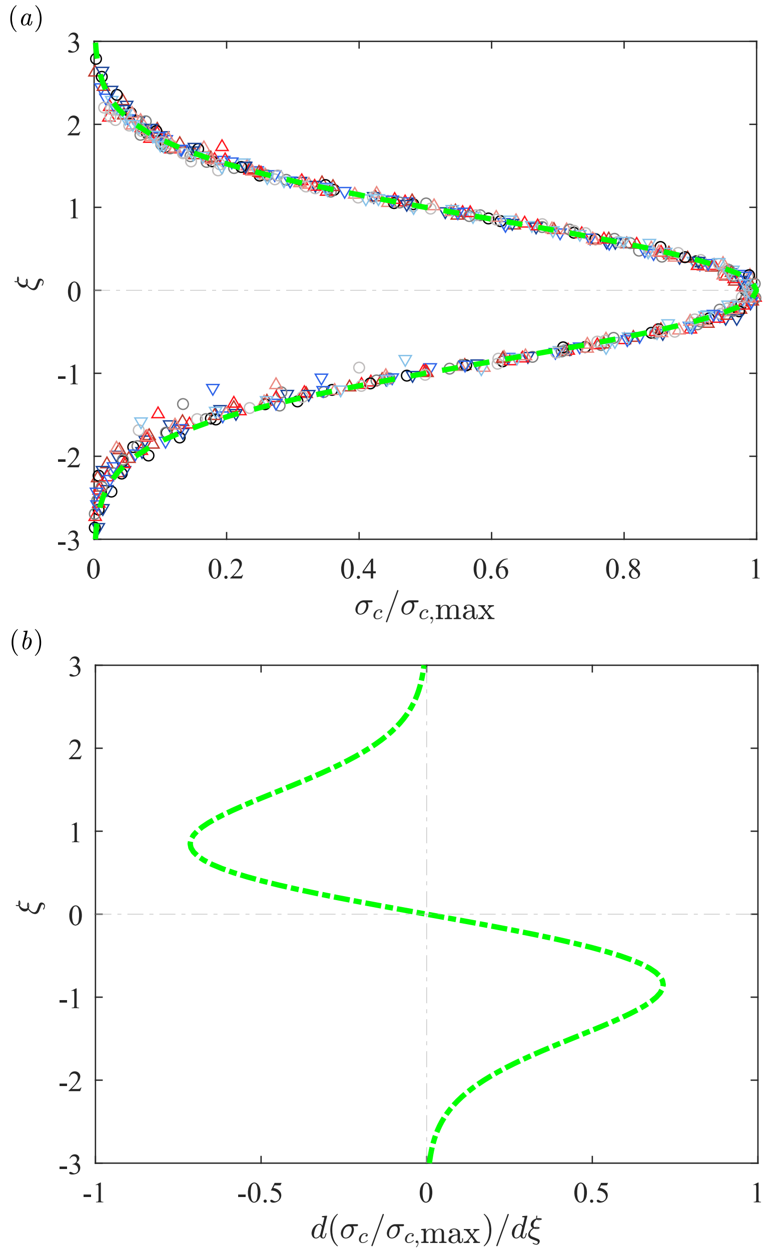


FIGURE 7.3: (*a*) Normalised standard deviation $\sigma_c$ for ES. (*b*) Derivative of a standard Gaussian distribution. Legend same as figure 7.1. The solid lines are for $S_z = 40$ mm.

of the normalised $\overline{wc}$ profile. Firstly, at the plume centreline ($\xi_\sigma = 0$) and at the plume edge($|\xi_\sigma| \gg 0$), $\overline{wc} = 0$ theoretically. Secondly, the maximum and minimum values of $\overline{wc}/\sigma_w\sigma_c$ are at similar $\xi_\sigma$ locations as the local extreme values of $\dfrac{\partial(\sigma_c/\sigma_{c,\,\mathrm{max}})}{\partial\xi_\sigma}$, which are the inflection points of the $\sigma_c$ profiles.

As noted earlier, the $y$-axis intercept of $\overline{wc}/\sigma_w\sigma_c$ is not always zero. When the $y$-axis intercept is either positive or negative, within the intercept, $\overline{wc}/\sigma_w\sigma_c$ have the same sign as $\dfrac{\partial(\sigma_c/\sigma_{c,\,\max})}{\partial\xi_\sigma}$, which means $\kappa_\sigma > 0$. This region of positive $\kappa_\sigma$ is referred to as the "displacement zone". This term was first introduced in the context of a traditional gradient diffusion model as equation 2.7, where the gradient of $C$ and a dimensional eddy diffusivity are considered. Though in equation 7.1 the gradient of $\sigma_c$ is considered, the same terminology of "displacement zone" is adopted here. In past literature, there are two contradictory explanations. Kurbatskii and Yanenko (1983) argued that the displacement zone is a zone of negative production of scalar fluctuation intensity caused by large-scale eddy transport, whereas Legg et al. (1986) believe it is more likely an experimental error. In the current study, density differences between the plume and the ambient are more likely to cause the displacement zone since $\overline{wc}$ for heavy plumes appears to be lower generally compared to that for light cases (i.e. more blue curves on the left of the green curve and more red curves on the right in figure 7.2). However, more data is required to confirm whether this is an error.

In figure 7.4, normalised $\overline{wc}$ is plotted against the derivative of standard Gaussian. For both elevated source and ground level source, all data congregate near the line of best fit (green dotted line) and display a similar trend. The vertical spread of the various profiles corresponds to the difference in the value of normalised $\overline{wc}$ at the same $\xi_\sigma$.

### 7.1.4 Comparison with the gradient-diffusion model

The advantage of equation 7.1 is that $\kappa_\sigma$ is non-dimensional. It does not change with downstream distance as the dimensional eddy-diffusivity in the traditional model. It is likely only dependent on the source property and the background flow; however, further investigation is needed to verify this. The purpose of the Reynolds-averaged transport equation is to calculate the mean concentration field, and they provide no information on the fluctuations. Nevertheless, $\kappa_\sigma$ is calculated from $\dfrac{\partial(\sigma_c/\sigma_{c,\max})}{\partial\xi_\sigma}$, which relies on the profiles of $\sigma_c$ and the usage of the non-dimensional $\kappa_\sigma$ proposed here introduces second-order statistics into the

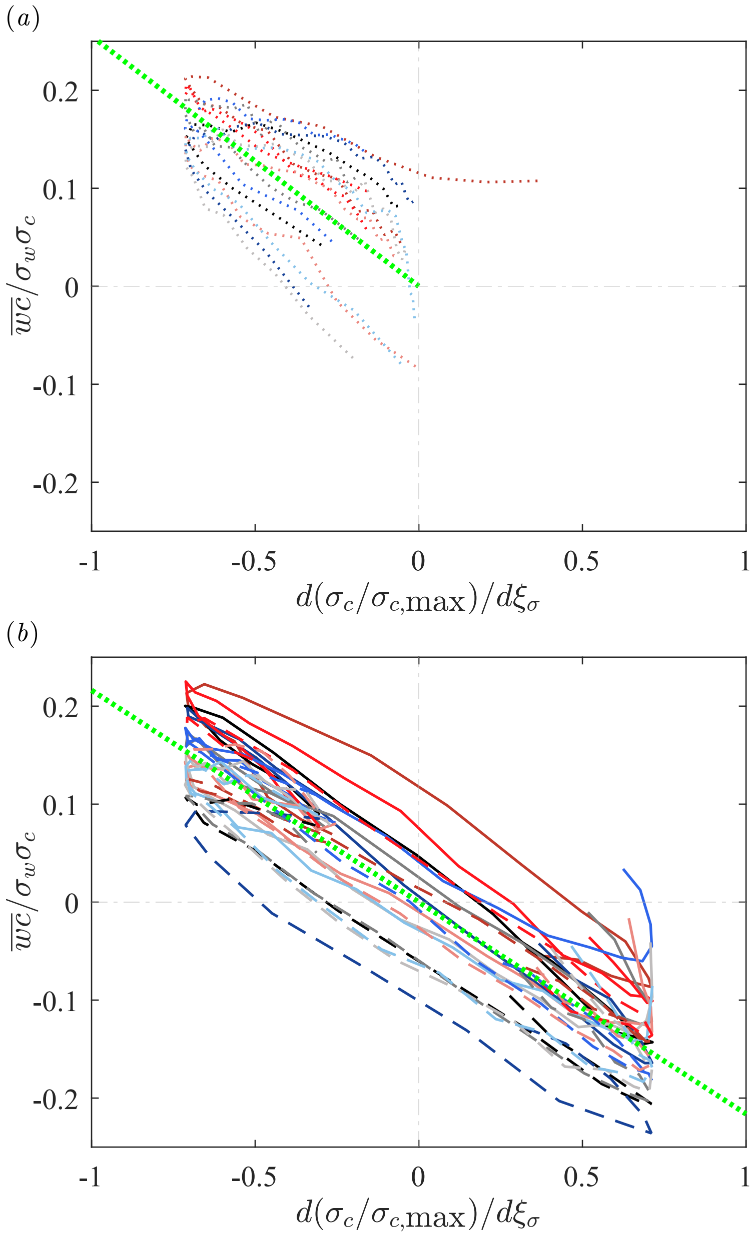


FIGURE 7.4: Normalised $\overline{wc}$ vs derivative of the standard deviation for (*a*) ground level source (*b*) $S_z = 80$ mm.The green dotted lines are the best fit of all the points. The slopes are approximately -0.09. Legend same as figure 7.1. The solid lines are for $S_z = 40$ mm.

equation. This means $\kappa_\sigma$, which aims to simplify the Reynolds-averaged transport equation, is not able to close the equation.

In the traditional gradient-diffusion model, $\overline{wc}$ is related to $\partial C/\partial z$ by a dimensional eddy diffusivity. Its advantage is that the second-order statistic, $\overline{wc}$, is eliminated from the Reynolds-averaged transport equation. The profile of the $C$ is also Gaussian, and its derivative is also an S-shape. It might seem that one can relate $\dfrac{\partial(C/C_{\max})}{\partial\xi}$ linearly with $\dfrac{\overline{wc}}{\sigma_w\sigma_c}$ like in equation 7.1

$$\frac{\overline{wc}}{\sigma_w\sigma_c} = \kappa_C\frac{\partial(C/C_{\max})}{\partial\xi} \tag{7.2}$$

However, the derivative of $C$ does not capture certain characteristics of $\overline{wc}$ as the derivative of $\sigma_c$ does. The normalised $\overline{wc}$ is plotted against the derivative of $C$ in figure 7.5. The maximum normalised $\overline{wc}$ in the upper half of the plume is highlighted by the black dots, while the red dot represents the inflection point of the mean profile. The average position $\xi_C$ of the black dots is not at the same $\xi_C$ as the red dot. So it is with the minimum of $\overline{wc}$. Moreover, the derivative approaches zero faster than $\overline{wc}$ at $\xi > 0$. Both these characteristics are due to the plume half-width calculated from $C$ being larger than that of $\sigma_c$, which is discussed in chapter 5. Therefore, in the present study, the gradient of $\sigma_c$ has better similarity with $\overline{wc}/\sigma_w\sigma_c$ better than the gradient of $C$.

## 7.2 Streamwise scalar fluxes

The Reynolds-averaged transport equation includes three scalar flux terms, namely $\dfrac{\partial\overline{u_i c}}{\partial x_i}$. To simplify practical calculations, the thin plume assumption is often adopted, where the plume width grows significantly slower than the downstream distance. Mathematically, this assumption allows us to neglect the term $\dfrac{\partial\overline{uc}}{\partial x}$ by assuming that $\dfrac{\partial\overline{uc}}{\partial x} \ll \dfrac{\partial\overline{wc}}{\partial z}$ and $\dfrac{\partial\overline{uc}}{\partial x} \ll \dfrac{\partial\overline{vc}}{\partial y}$.

Nonetheless, the behaviour of $\overline{uc}$ is presented in this section. In the boundary layer, many studies have demonstrated that $\overline{uw} < 0$ (e.g. Baidya 2016). Consequently, when $\overline{wc}$ is positive above the plume centreline, $\overline{uc}$ is negative, and vice versa. Therefore, while the shape of $\overline{wc}$ exhibits a reverse S-shape, the overall shape of $\overline{uc}$ takes the opposite form of an S-shape. The opposite signs of $\overline{uc}$ and $\overline{wc}$ above and below the centreline have been observed in several experimental studies (Karnik and Tavoularis 1989; Lavertu and Mydlarski 2005). Given

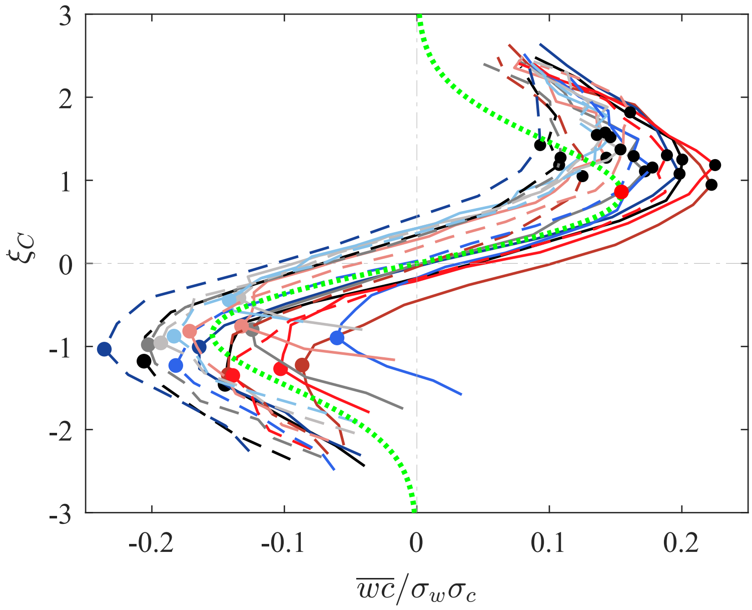


FIGURE 7.5: Normalised $\overline{wc}$ vs a normalised distance from the centreline based on the mean concentration profiles for $S_z = 40$ and 80 mm. The green dotted line is an arbitrary constant multiplied by $\dfrac{\partial(C/C_{\max})}{\partial \xi_C}$. Legend same as figure 7.1.

the similar behaviour between $\overline{wc}$ and $\overline{uc}$ described, a model analogous to equation 7.1 is not available for $\overline{uc}$ since the contribution from $dC/dx$ is of the same magnitude as $dC/dy$ (Vanderwel and Tavoularis 2014) and neither is measured in the current study.

### 7.2.1 Evolution and self-similarity of $\overline{uc}$

Figure 7.6($a$) illustrates the dimensional profile of $\overline{uc}$ for $S_z = 40$ mm at three downstream distances. All profiles exhibit an S-shape, with a decrease in magnitude downstream. The shape of the profile is consistent with the theoretical shape and the experimental observation by Legg et al. (1986) and Talluru et al. (2018). This reduction in magnitude follows the same trend observed for $\overline{wc}$ due to the smaller downstream value of $C$ and $\sigma_c$.

To normalise $\overline{uc}$, a similar approach as used for $\overline{wc}$ is applied, but with the adoption of $\sigma_u$ instead of $\sigma_w$. Figure 7.6($b$) presents the $\overline{uc}/\sigma_u\sigma_c$ for $S_z = 40$ mm. The theoretical S-shape of $\overline{uc}$ is discernible, with a less pronounced difference in magnitude upon normalisation.

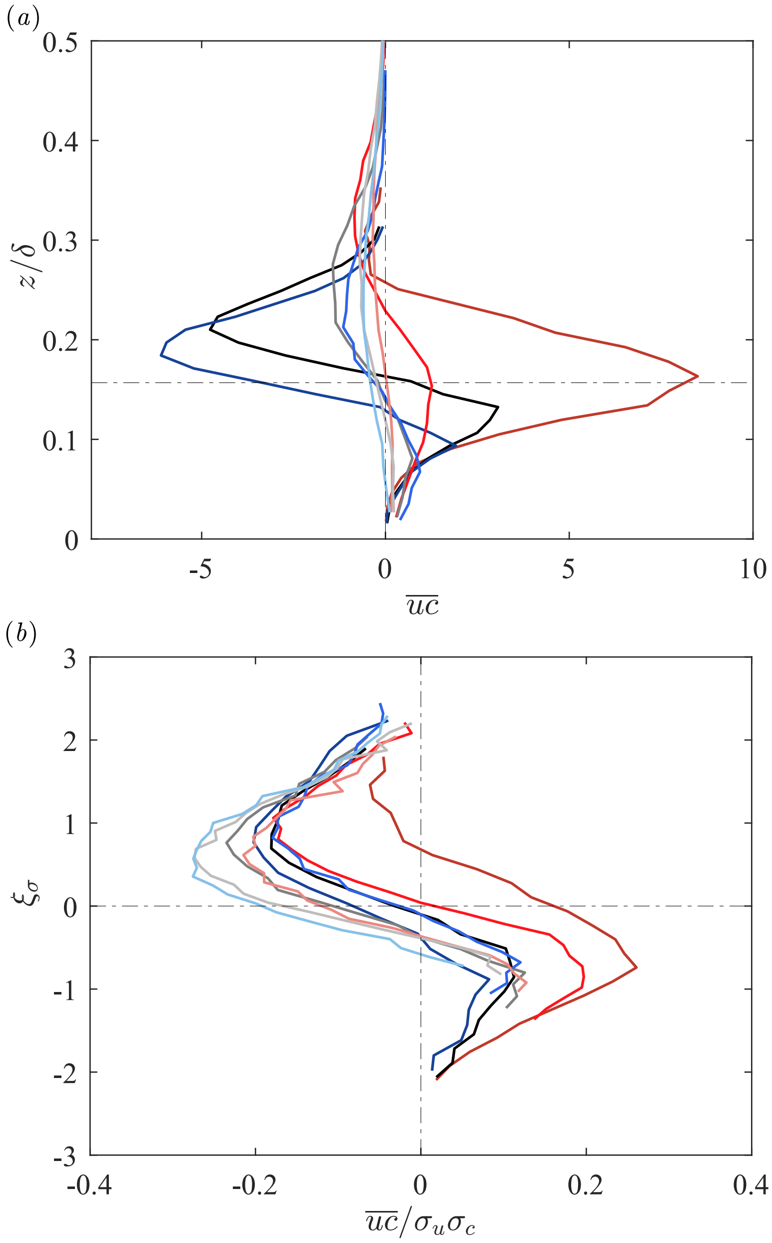


FIGURE 7.6: $\overline{uc}$ for $S_z = 40$ mm for $S_z/\delta = 1$, 2, and 4. Legend same as figure 7.1. (*a*) Dimensional $\overline{uc}$. The horizontal dash-dotted line is $S_z$. (*b*) Normalised $\overline{uc}$ vs normalised distance from the plume centreline. The horizontal dash-dotted line is at the plume centreline.

However, the agreement of the normalised $\overline{uc}$ to theory is not as good as for normalised $\overline{wc}$ in figure 7.2. The displacement zone appears more prominent in the normalised $\overline{uc}$ profile. For normalised $\overline{wc}/\sigma_w\sigma_c$, the displacement magnitude is within $\pm0.5$ of $z/\delta$ for all the profiles, but the $y$-intercept of normalised $\overline{uc}/\sigma_u\sigma_c$ is as high as 1.

### 7.2.2 The magnitude of $\overline{uc}$ and $\overline{wc}$

Since the trends of $\overline{uc}$ and $\overline{wc}$ are opposite above and below the plume centreline ($\overline{uc}$ exhibits an S-shape, and $\overline{wc}$ shows a reverse S-shape), their values may be related. Therefore, it is worth comparing the magnitudes of $\overline{uc}$ and $\overline{wc}$.

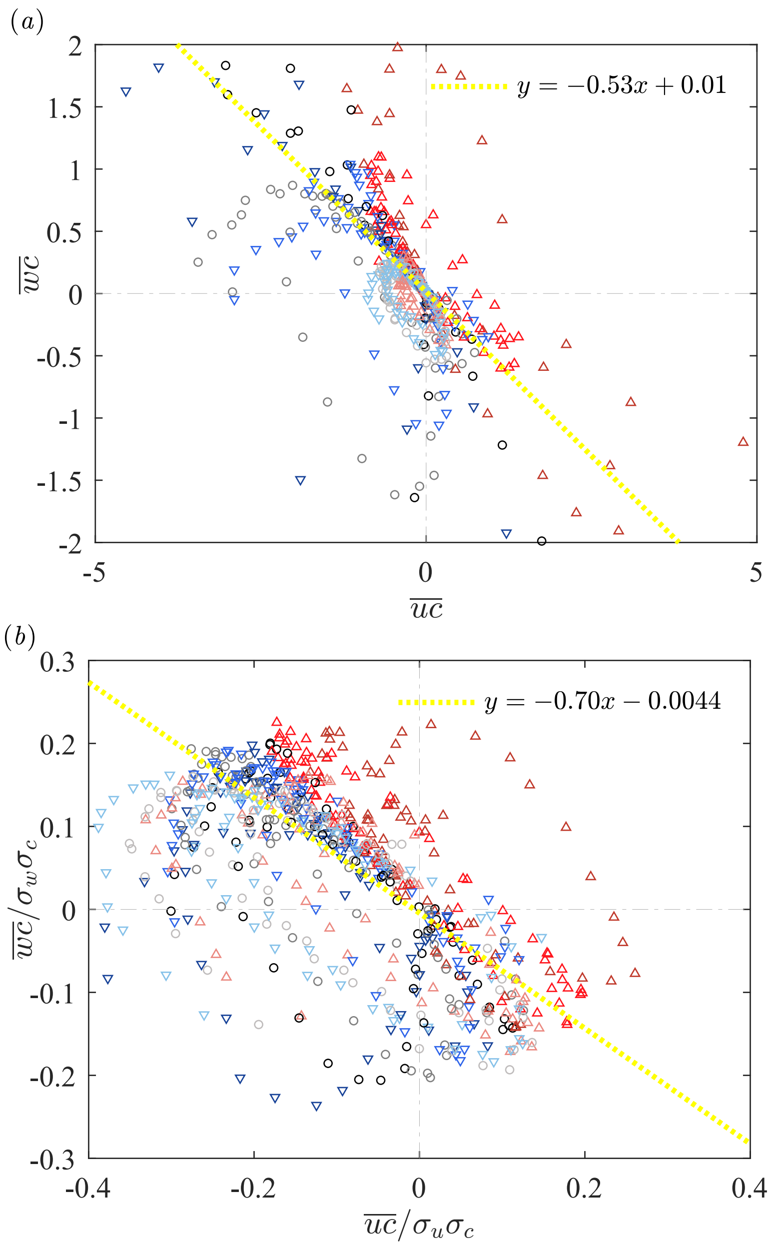


FIGURE 7.7: (*a*) Dimensional $\overline{wc}$ vs $\overline{uc}$. (*b*) Normalised $\overline{uc}$ vs $\overline{uc}$. The yellow dotted lines are lines of best fit. Legend same as figure 7.1.

Figure 7.7 compares the dimensional and normalised scalar fluxes with lines of best fit. The peak magnitude of normalised $\overline{wc}$ is less than 0.3, and normalised $\overline{uc}$ is between -0.4 and 0.4. The range observed here is slightly less than the range reported by Karnik and Tavoularis (1989) and Lavertu and Mydlarski (2005), where the peak normalised fluxes values are between 0.4 and 0.5. A lag between $\overline{uc}$ and $\overline{wc}$ is reported by Talluru et al. (2018); however, figure 7.7 is plotted without the lag. The general trend between $\overline{wc}$ and $\overline{uc}$ appears to be linear. Further investigation is needed to elucidate their relationship.

## 7.3 Summary

In this chapter, the behaviour of scalar fluxes is studied since they contain information to close the Reynolds-averaged transport equation with an emphasis on the vertical scalar fluxes, $\overline{wc}$.

A novel method is employed to non-dimensionalise $\overline{wc}$, where $\overline{wc}$ is divided by the local RMS of vertical velocity and RMS of concentration. The resulting normalised $\overline{wc}$ data collapse onto a single curve when plotted against the normalised distance to the plume centreline, in line with theoretical expectations. The normalised $\overline{wc}$ is then used to modify the traditional gradient diffusion model. A new non-dimensional parameter, $\kappa_\sigma$, is proposed to the linearly relate normalised $\overline{wc}$ and the gradient of normalised RMS of concentration. The model captures well the shape of normalised $\overline{wc}$ and shows good agreement with data. Unlike the traditional gradient-diffusion model, $\kappa_\sigma$ remains constant with downstream distance, introducing an advantage. However, including second-order statistics in the Reynolds-averaged transport equation adds complexity.

The streamwise scalar fluxes are also studied. It is found that they, too, collapse onto a curve upon normalisation. The sign of normalised $\overline{uc}$ is opposite to that of normalised $\overline{wc}$, i.e., $\overline{uc}$ is negative and positive above and below the plume centreline, respectively. In typical measurements, $\overline{uc}$ is the quantity measured, especially in outdoor field measurements. It might be possible to estimate $\overline{wc}$ indirectly via $\overline{uc}$ measurements using the correlation functions. However, a more focused assessment is required to reveal any dependency between $\overline{wc}$ and $\overline{uc}$, taking into account the relative lead and lag as discussed in Talluru et al. (2018).

CHAPTER 8

# Effect of roughness on the near-field plume characteristics

---

Chapters 4 to 6 focus on the dispersion of buoyant plumes over smooth wall boundary layers. However, understanding plume dispersion over rough surfaces is also of significant practical interest, such as scenarios involving chimney stacks near urban terrain. The presence of roughness introduces additional turbulence and large-scale motions into the flow. In urban environments, street canyons often exhibit recirculation flows, which can trap pollutants and result in high pollutant concentrations at the pedestrian level. Consequently, studying the dispersion of buoyant plumes in rough wall boundary layers is also essential.

Within this thesis, wind tunnel experiments are conducted to investigate two roughness setups utilising 40 mm cubes as roughness elements. The height of the roughness is denoted as $h$, while the spanwise spacing between the cubes is also $h$. The streamwise spacing, $\Delta s$, is either $h$ or $2h$. Detailed information regarding the experimental setup can be found in chapter 3. Additionally, a summary of the background flow is provided in table 8.1.

This chapter compares plume dispersion between smooth- and rough-wall cases, specifically emphasising mean concentration, $C$, and root-mean-square concentration, $\sigma_c$. Measurements are taken at two streamwise locations ($S_x/\delta = 1$ and 2). Due to the limited $S_x$, the analysis primarily focuses on the qualitative aspects rather than providing quantitative observations.

| | $U_\infty$, m/s | $\delta$, m | $Re_\delta$ | $u_\tau$, m/s | $Re_\tau$ |
|---|---|---|---|---|---|
| Smooth | 2.5 | 0.255 | 43100 | 0.0938 | 1580 |
| $\Delta s/h = 1$ | 2.5 | 0.34 | 56667 | 0.207 | 4710 |
| $\Delta s/h = 2$ | 2.5 | 0.34 | 56667 | 0.206 | 4670 |

TABLE 8.1: Summary of key parameters of the background flows, one smooth case and two roughness cases.

## 8.1 Characteristics of mean and standard deviation of concentration

The analysis of the profiles of $C$ and $\sigma_c$ reveals interesting characteristics both above and below the canopy of roughness.

### 8.1.1 Mean concentration

The normalised mean concentration profiles over roughness are presented in figure 8.1. These profiles exhibit asymmetry around the height of maximum concentration, $z_{\text{max}}$. Above the canopy, the profiles are relatively smooth and can be described by a truncated Gaussian distribution.

$$C(z) = C_{\text{max}} \exp\left[-\left(\frac{z - z_{\text{max}}}{\delta_z}\right)^2\right], z > h \tag{8.1}$$

The above equation is similar to equation 2.24, with $z_{\text{max}}$ replacing $z_{\text{CL}}$. The fitted equation captures the profile above the roughness remarkably well (all R-square $> 0.98$). This can be explained by extending the wall similarity theory discussed in section 2.3.2. In the outer region of high Reynolds number ($Re$) rough wall boundary layers, the scales responsible for mixing are self-similar. Thus, the concentration profile in the outer region of a rough wall boundary layer follows the same scaling law (Gaussian) as that in a smooth wall boundary layer because the dispersion mechanisms are similar, and the background flow can be described by the same similarity law, i.e. equation 2.13. Note that the fitted truncated Gaussian models are plotted only above the roughness height in figure 8.1. However, caution is advised when interpreting results for the ground-level source, as the location of the maximum concentration, an essential parameter for defining the Gaussian fit, often falls below the roughness, reducing the reliability of the parameters extracted from the fitted curves (e.g. half-width, maximum).

Below the canopy, the profiles cannot be described by a Gaussian distribution, but not the same Gaussian equation, due to pollutant trapping within the canopy. For instance, in figure 8.1($c$), for $S_x/\delta = 1$, $\dfrac{\partial C}{\partial z}$ approaches 0 on both sides of the plume, but only the upper half of the plume exhibits $C \to 0$.

The same asymmetrical pattern is also observed in data from DNS simulation (Branford et al. 2011). To emphasise the asymmetry of the mean concentration profiles over roughness, the normalised mean profiles are compared in figure 8.2. The plume spread in the roughness cases is significantly larger than in the smooth cases, owing to increased turbulence intensity. While the upper halves of the profiles over the two roughness cases are nearly indistinguishable, the lower halves exhibit different behaviours.

Studies by Wong and Liu (2013) and Salizzoni et al. (2009) fitted the profile above the roughness using a truncated Gaussian, while Macdonald et al. (1998) and Pascheke et al. (2008) fitted the entire profile to a reflected-Gaussian. There are two possible reasons for the disparity. Firstly, the $h/\delta$ ratio in their studies is smaller, resulting in a smaller portion of the plume deviating from the standard Gaussian. Additionally, their studies featured fewer data points in each half and failed to capture the complex shape of the profile within the roughness. Although neither Gaussian nor reflected Gaussian fits are employed for the entire profiles in figure 8.1, it is possible that further downstream, the entire profile can be described by a single equation. Further investigation is necessary for this.

The influence of the density ratio on dispersion characteristics can also be observed in figure 8.2. In each group of three profiles (heavy, neutral, and light gas released at the same $S_z$ and $S_x$), the heavy gas profiles consistently remain below, while the light gas profiles remain above. One exception is noted: the mean profiles of the ground-level source released over $\Delta s = h$ roughness are barely distinguishable in figure 8.1($d$). This indicates that when the source is released with the roughness where turbulence intensity is high, the buoyancy effects vanish within $1\delta$ downstream from the source.

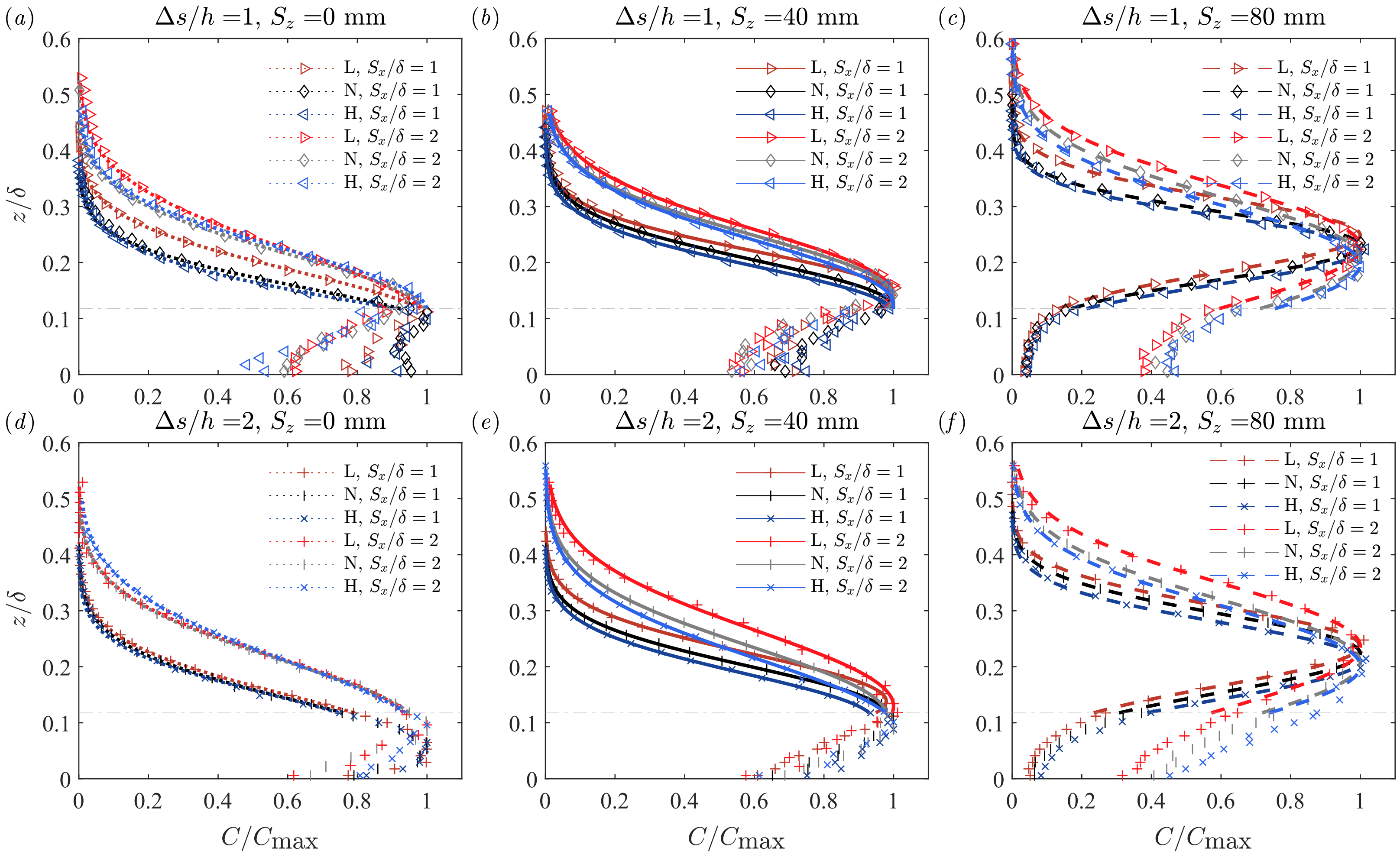


FIGURE 8.1: Vertical profile of normalised mean concentration for $S_x/\delta = 1$ and 2, three source heights, and three density ratios in rough wall boundary layers. The profiles are normalised by the maximum of each profile. The dotted lines, solid lines and dashed lines are truncated-Gaussian equations fitted for the profile above the roughness.

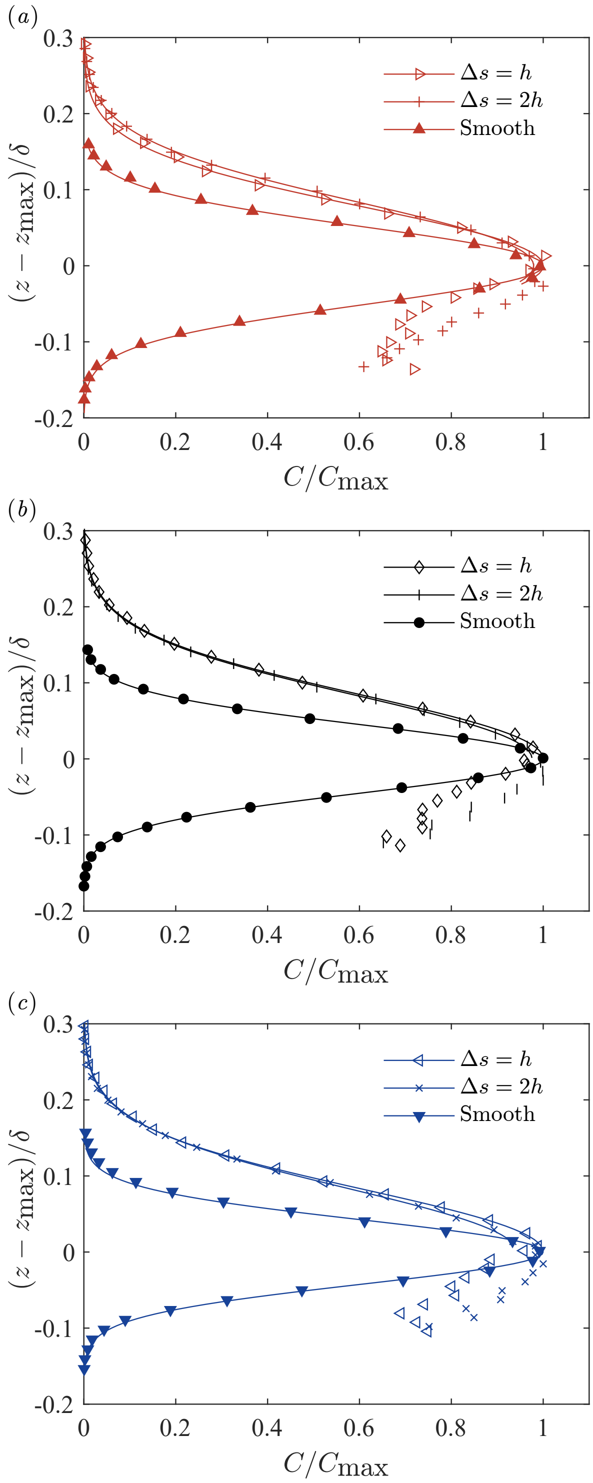


FIGURE 8.2: Dimensional mean concentration profile for $S_z = 40$ mm measured at $S_z/\delta = 1$ downstream for the smooth and two roughness cases to highlight the effect of roughness on the mean concentration field. The solid lines are Gaussian fit for the smooth case and truncated Gaussian fit for the roughness cases. (*a*) Light; (*b*) Neutral; (*c*) Heavy.

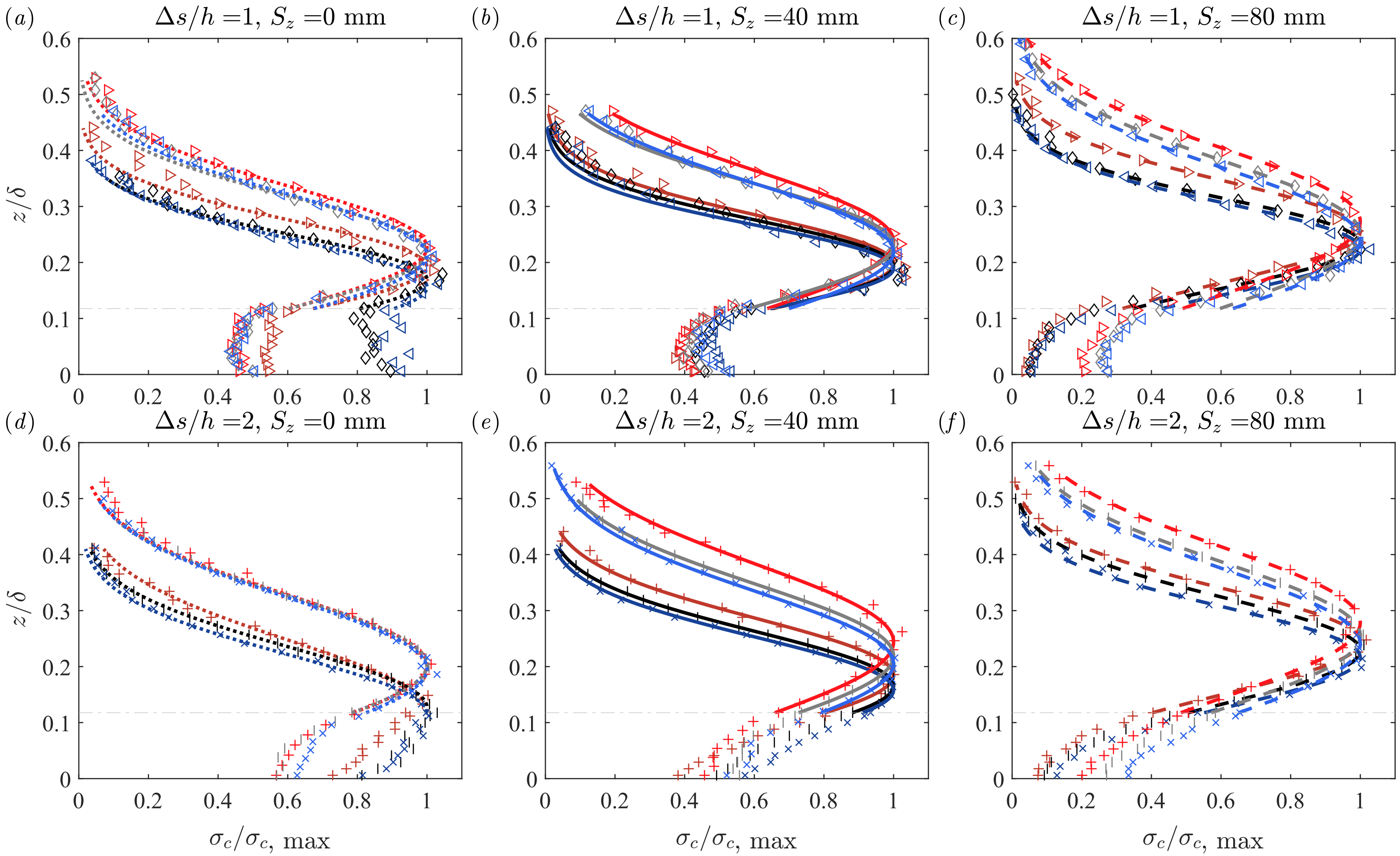


FIGURE 8.3: Vertical profile of normalised standard deviation of concentration for $S_x/\delta = 1$ and 2, three source heights, and three density ratios in rough wall boundary layers. The profiles are normalised by the maximum of each profile. The dotted lines, solid lines and dashed lines are truncated-Gaussian equations fitted for the profile above the roughness. Legend same as figure 8.1.

### 8.1.2 Standard deviation of concentration

The profiles of the standard deviation of concentration, $\sigma_c$, normalised by the maximum value, $\sigma_{c,\,\mathrm{max}}$, are presented in figure 8.3.

Similar to the normalised mean concentration profiles in figure 8.1, the profiles of concentration RMS exhibit a non-symmetric shape. The upper half of the profiles follow a truncated Gaussian distribution, and the fitted results are plotted accordingly. However, the lower half of the profiles do not exhibit a Gaussian shape. Another notable similarity between the profiles of $C/C_{\mathrm{max}}$ and $\sigma_c/\sigma_{c,\,\mathrm{max}}$ is the effect of density ratio. In both cases, the profiles of lighter gases are above, while those of heavier gases are below. An exception to this behaviour is observed in the ground-level profiles at $S_x/\delta = 2$ released in $\Delta s = 2h$, where the normalised profiles for all density ratios collapse. It is worth recalling that the normalised mean concentration profiles agree with each other at both measured $S_x$ locations. This suggests that the effect of density ratio is not observable in the mean profile at $S_x = \delta$, but it is clearly evident in the distribution of $\sigma_c$. The reason for this observation is not clear yet; however, it would be worthwhile to examine the behaviour of higher-order moments from measurements of the buoyant plume over roughness in the future.

A notable difference between the mean and the r.m.s. concentration profiles is the height at which they attain their maximum values, denoted as $z_{\mathrm{max}}$ and $z_{\sigma,\,\mathrm{max}}$, respectively. The interpretation of this discrepancy is later discussed in section 8.3.

Another distinction between the general shapes of $C$ and $\sigma_c$ profiles lies in the location of the minimum in the lower half of the profile. For $S_z = 0$ mm and 40 mm released in $\Delta s = h$, the minimum $\sigma_c$ in the lower part of the profile is not located at the wall, unlike other $\sigma_c$ profiles or any $C$ profiles. Within the roughness region, $\sigma_c$ exhibits a minimum at approximately the mid-height of the roughness, while its magnitude is larger at the wall and at the height of the roughness. These local minima are unlikely to be errors, as their magnitudes exceed the error range of the concentration sensor ($\pm 5\%$). This behaviour is closely related to a local minimum of the standard deviation of vertical velocity, $\sigma_w$, at this height, as shown in figure

8.4. Hence the likely cause of the local minima is that the slightly higher vertical velocity above and below this location transports the effluent away from this location.

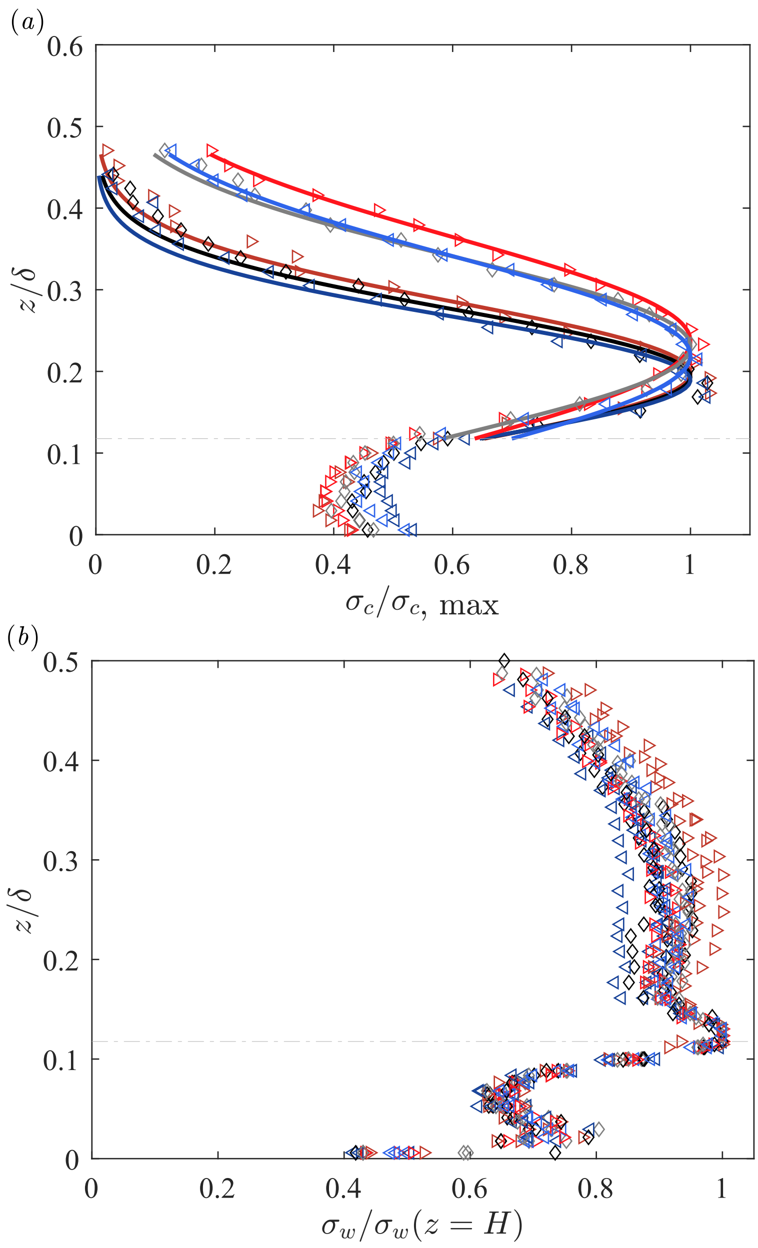


FIGURE 8.4: (*a*) Vertical profile of normalised standard deviation of concentration for $S_z = 40$ mm over roughness $\Delta s = h$, repeated from figure 8.3 (*b*). (*b*) Standard deviation of the vertical velocity for roughness $\Delta s = h$. The grey dash-dotted line is the height of the roughness. Legend same as figure 8.1.

### 8.1.3 Normalised profiles using Gaussian parameters

Using the parameters from the truncated Gaussian fit, the upper parts of each profile collapse onto a standard Gaussian equation, as shown in figure 8.5. The asymmetry of the profiles due to roughness is more observable in these two figures. The lower parts of ground-level source profiles (solid symbols) deviate more from the standard Gaussian equation than elevated sources. A more detailed discussion of the variation of the three parameters is included in the following sections of this chapter.

## 8.2 Maximum of mean and standard deviation of concentration

It is observed that $C_{\max}$ is the largest for the smooth case and smallest for the R2 case, which aligns with the expected behaviour. This trend corresponds to the lowest turbulence intensity for the smooth wall boundary layer and the highest turbulence intensity for R2, as demonstrated in figure 3.14($b$). However, it should be noted that using $C_{\max}$ as a normalising parameter for each profile is still subject to two further considerations. First, the entire profile of $C$ over roughness cannot be accurately described by a single equation. While $C_{\max}$ holds value as a parameter for dispersion in a smooth wall boundary layer, where it is utilised in the reflected-Gaussian equation for elevated sources and the exponential equation for ground-level sources, its relevance becomes uncertain in cases where the location of $C_{\max}$ falls below the roughness. In such situations, the relation between $C_{\max}$ and the parameters of the Gaussian upper part is unknown. However, it is preferable to establish a correlation between the upper and lower parts of the profile, as predicting the concentration below the roughness is often of practical interest, especially concerning exposure to pedestrians.

Furthermore, it should be emphasised that $C_{\max}$ for ground-level sources does not coincide with the first parameter of the Gaussian fit for the upper part of the plume.

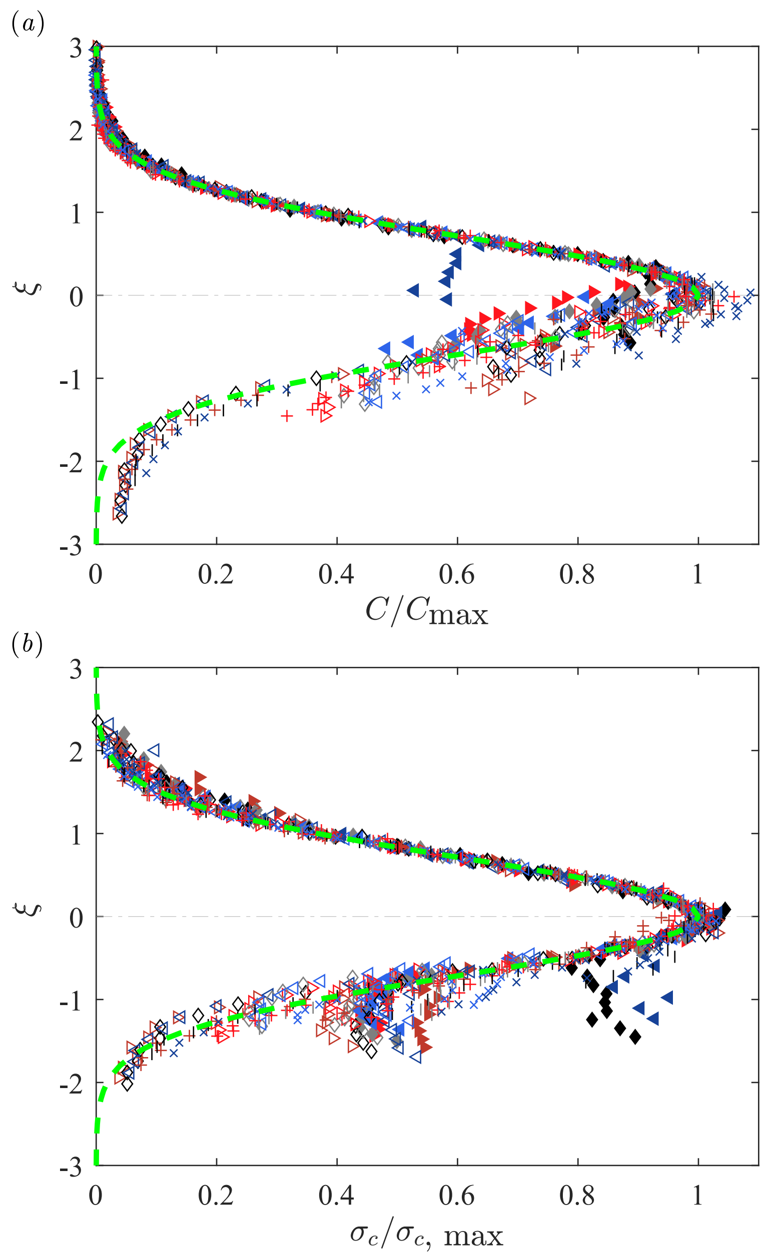


FIGURE 8.5: (*a*) Vertical profile of normalised mean concentration vs normalised distance from the location of maximum. (*b*) Vertical profile of normalised r.m.s. of concentration vs normalised distance from the location of maximum. The green dash-dotted line is the standard Gaussian, and the grey dash-dotted line is at $\xi = 0$. Other legends as figure 8.1. The solid symbols are ground-level sources and represent the same data as the hollow symbols of the same shape in figure 8.1

## 8.3 Location of maxima

The positions of the maximum mean concentration, $z_{\text{max}}$, and the maximum standard deviation, $z_{\sigma,\text{ max}}$, are depicted in figure 8.6. The impact of roughness on the location of these maxima in the concentration profiles is examined. For both roughness configurations at $S_z = 80$ mm, $z_{\text{max}}$ and $z_{\sigma,\text{ max}}$ exhibit deviation from the source height. On the other hand, for $S_z = 40$ mm, different behaviours are observed. When $\Delta s = h$, $z_{\text{max}}$ is slightly above the height of the roughness. This may be attributed to the highest turbulence levels around this height, causing the flow to skim over the roughness (referred to as the "$d$-type" flow regime). However, this trend does not hold for $\Delta s = 2h$, as its $z_{\text{max}}$ is below the roughness. This discrepancy can be attributed to a larger spacing between each row of blocks (known as the "$k$-type" roughness). Hence, dispersion models should not only consider the velocity profile but also account for near-wall flow characteristics and roughness type ($k$-type or $d$-type), as also highlighted by Wong and Liu (2013). On the other hand, $z_{\sigma,\text{ max}}$ is significantly higher for both roughness configurations, reaching nearly twice the source height. For ground-level sources, the influence of roughness on the location of $C_{\text{max}}$ becomes more apparent. In the smooth case, $C_{\text{max}}$ consistently resides at $z = 0$. However, for both roughness cases, $z_{\text{max}}$ rises to approximately the height of the roughness, with the case $\Delta s = h$ exhibiting a slightly higher $z_{\text{max}}$. $z_{\sigma,\text{ max}}$ for ground-level sources is not at the wall or close to the roughness height. It undergoes a considerable rise, surpassing the rise in $z_{\text{max}}$. The roughness type alone is insufficient to explain this phenomenon, suggesting the presence of additional contributing 3D flow mechanisms that are not investigated in this thesis.

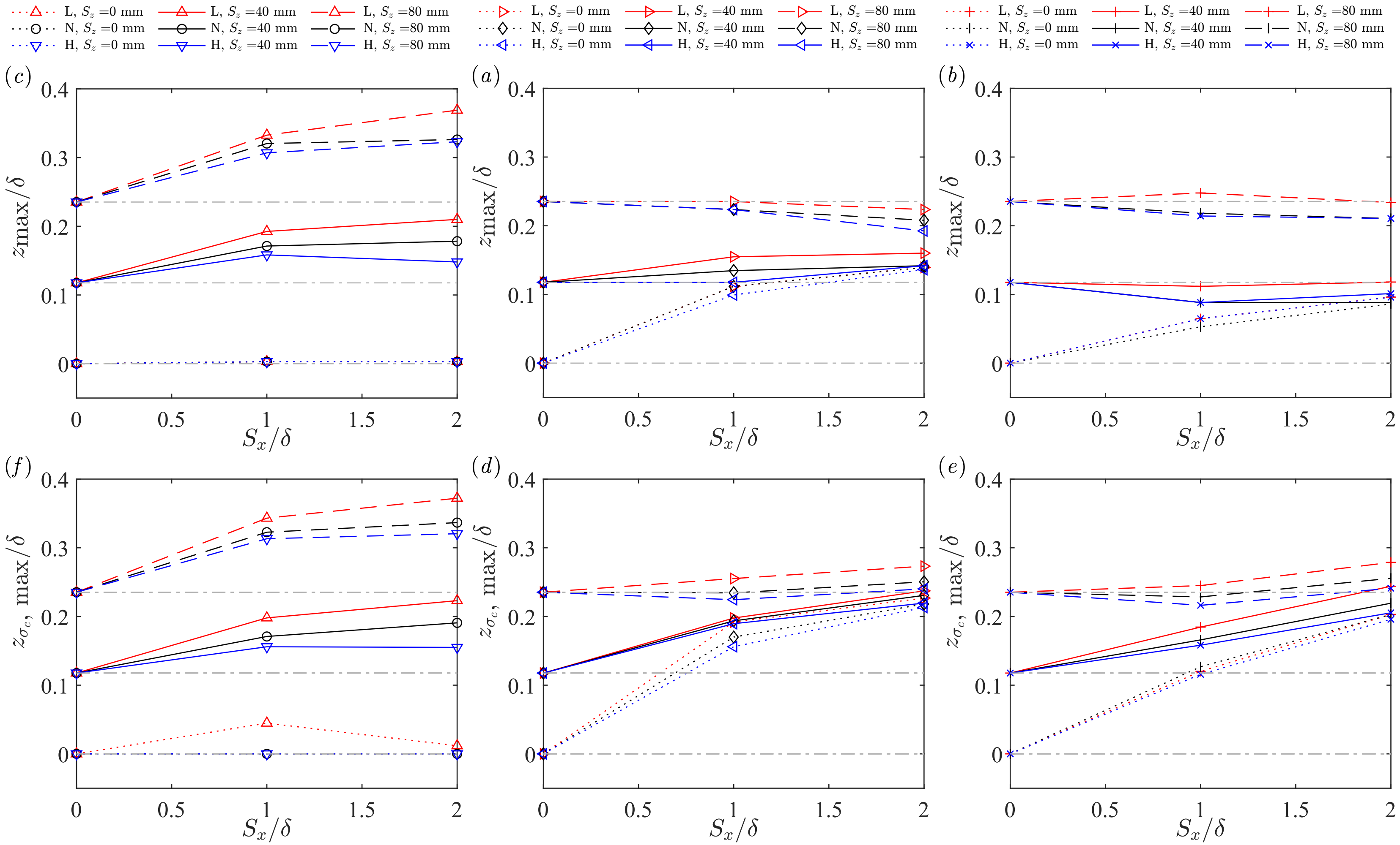


FIGURE 8.6: Location of maxima of each profile released at each source height. (*a,b,c*): Location of maxima of mean concentration; (*d,e,f*): Location of maxima of the standard deviation of concentration. (*a,d*): Smooth wall; (*b,e*): $\Delta z = h$; (*c,f*): $\Delta z = 2h$. The legend on top of each row applies to both figures in the row. The grey dashed-dotted lines are the source height.

## 8.4 Plume half-width

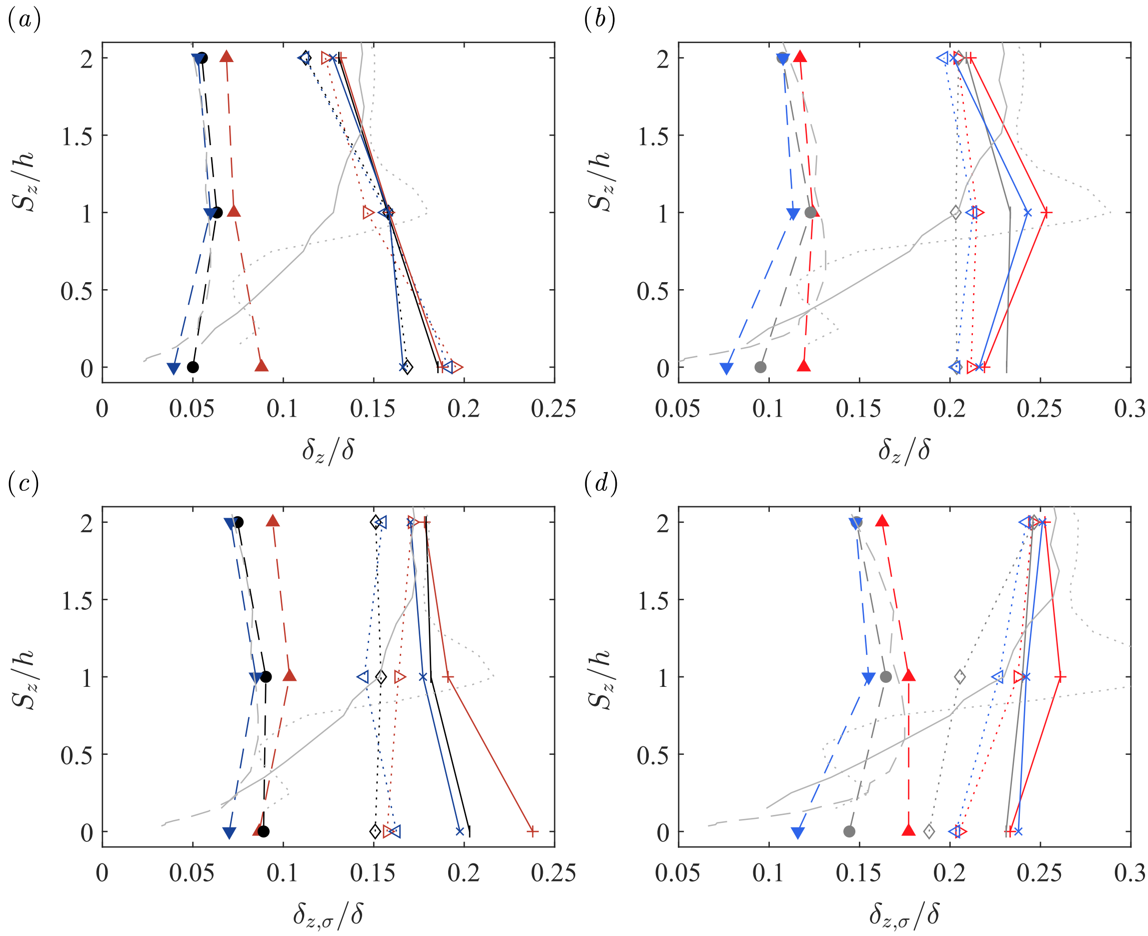


FIGURE 8.7: Plume half-width of the mean and standard deviation of concentration for the smooth case and two roughness cases. The half-width is calculated from the truncated Gaussian fit above the roughness height for the two roughness cases. (*a*) $S_x/\delta = 1$; (*b*) $S_x/\delta = 2$. The grey lines are arbitrary factors times the variance of vertical velocity. Legend same as figure 8.1.

s The plume half-widths for the upper part of the plume, denoted as $\delta_{z,\,\mathrm{R1}}$ and $\delta_{z,\,\mathrm{R2}}$ for roughness $\Delta s = h$ and $\Delta s = 2h$ respectively, are presented in figure 8.7. These values are distinct from $\delta_z$, which corresponds plume half-width of the entire profile for the smooth wall case. The half-widths are determined from the fitted truncated-Gaussian function applied to the upper part of the plume, as equation 8.1. In general, the half-widths follow the trend $\delta_z < \delta_{z,\,\mathrm{R1}} < \delta_{z,\,\mathrm{R2}}$. It is expected that $\delta_z$ is the smallest since the velocity fluctuation in the lower part of the smooth-wall boundary layer is smaller and hence less thorough turbulent

| | $S_x/h \approx 8.5$ | $S_x/h \approx 17$ | Roughness type | Spacing |
|---|---|---|---|---|
| | $\downarrow \delta_z/h$ | $\downarrow \delta_z/h$ | | |
| Macdonald et al. (1998) | 1 | 1.1 | 3-dimensional | $2h$ |
| Pascheke et al. (2008) | 1.2 | 1.7 | 3-dimensional | $3h$ |
| Wong and Liu (2013) | 0.5 | 1 | 2-dimensional | $2h$ |
| This thesis | 1.5 | 1.9 | 3-dimensional | $2h$ |

TABLE 8.2: Mean plume half-width of ground-level sources ($S_z/h = 0$) for the neutral plume case. The data from other studies are estimated from their plots. $S_x/h \approx 8.5$ and $S_x/h \approx 17$ correspond to $S_x/\delta = 1$ and $S_x/\delta = 2$ respectively in this thesis. Legend same as figure 8.6.

| | $S_x/h \approx 8.5$ | $S_x/h \approx 17$ | Roughness type |
|---|---|---|---|
| | $\downarrow \delta_z/h$ | $\downarrow \delta_z/h$ | |
| Salizzoni et al. (2009) | 0.5 | 0.7 | 2-dimensional |
| This thesis | 1 | 1.9 | 3-dimensional |

TABLE 8.3: Mean plume half-width of $S_z/h = 2$ for the neutral plume case. $\Delta s/h = 1$ for both studies tabulated. The data from other studies are estimated from their plots. $S_x/h \approx 8.5$ and $S_x/h \approx 17$ correspond to $S_x/\delta = 1$ and $S_x/\delta = 2$ respectively.

mixing, while $\delta_{z,\,\mathrm{R1}} < \delta_{z,\,\mathrm{R2}}$ aligns with previous research indicating that larger $\Delta s$ leads to a re-circulation zone and wider plume spread (Salizzoni et al. 2009; Wong and Liu 2013). This suggests that plumes in flows with wake interference are broader than those in skimming flows. The relationship $\delta_z < \delta_{z,\,\mathrm{R1}} < \delta_{z,\,\mathrm{R2}}$ also corresponds to the magnitude of $C_{\mathrm{max}}$ for each case, although this is not depicted in the current figure. The average ratio of $\delta_{z,\,\mathrm{R1}}/\delta_z$ and $\delta_{z,\,\mathrm{R2}}/\delta_z$ ranges between 1.5 to 1.9 times. The mean plume half-width relative to roughness height reported in other studies is compared with the current study in tables 8.2 and 8.3. The half-widths observed are of the order of the roughness height mostly, though the values reported in this thesis are higher than in other studies for source heights compared. Another observation is that the plume width over 3-dimensional roughness is higher than that over 2-dimensional roughness.

Regarding the density ratio of the source gas, it is observed that light gases exhibit the widest plume width. In contrast, heavy gases display the narrowest plume width for smooth and rough wall flows, except at $S_x = 1\delta$ downstream, where the profiles collapse, as shown in figure 8.1($b$) and 8.3($b$). However, the difference in half-widths for different $\rho_s/\rho_\infty$ is reduced in rough-wall boundary layers compared to the smooth-wall case due to enhanced turbulent mixing. This finding supports the notion that roughness enhances turbulent mixing, diminishing the influence of density variations on plume dispersion.

For the plume behaviour at different heights, the plume half-width for $S_z = 40$ mm is larger than that for $S_z = 0$ mm and $S_z = 80$ mm, due to higher standard deviation of vertical velocity, $\sigma_w$, for $S_z = 40$ mm. This observation is not limited to flows dominated by roughness and also applies to plume dispersion in smooth-wall boundary layers (Talluru et al. 2019b). Talluru et al. (2019b) also proposed a simple model to predict the plume half-width using the scaled variances of spanwise and wall-normal velocities, $\sigma_v^2$ and $\sigma_w^2$. Their model agrees well with our smooth wall data, suggesting that local turbulence levels at the plume centreline govern the plume spread. However, adjustments are necessary for the scaling coefficient for different density ratios. Further, the plume spread over roughness does not exhibit the same trend as $\sigma_w^2$.

## 8.5 Summary

Including roughness in the flow introduces asymmetrical wall-normal profiles for the mean and standard deviation of concentration. The upper part of the profile follows a truncated Gaussian, while a different equation is needed to describe the lower part. The roughness leads to higher locations of local maxima in the mean and standard deviation compared to smooth wall conditions, with the effect being more pronounced for the standard deviation. Although the density effects are still observable, the differences between each density ratio are less significant compared to the smooth-wall case.

These findings emphasise the complexities of characterising concentration and root-mean-square concentration profiles in rough canopy environments. The non-Gaussian nature of the lower portion of the profiles presents challenges in accurately predicting and modelling pollutant dispersion in such settings. The results also highlight the intricate interplay among flow regime, roughness type, and the density effect in pollutant dispersion. Understanding and incorporating these factors into dispersion models are crucial for achieving precise predictions in rough canopy environments.

CHAPTER 9

# Conclusion

---

The research conducted in this PhD thesis investigates the behaviour of buoyant plumes in a turbulent boundary layer. The experimental phase of the study involves the development of a novel setup enabling the release of gases with varying densities into a boundary layer wind tunnel. Concurrent measurements of concentration and velocity components are conducted using a highly accurate Photo-ionisation device and an $\times$-wire, respectively. The data obtained from these sensors prove suitable for analysing high-order statistics and the joint behaviour of concentration and velocity.

The analysis of plume evolution demonstrates that the profile of mean and root-mean-square (RMS) concentrations of heavy and light gases exhibit Gaussian characteristics akin to those observed in a neutral plume. However, distinct differences are observed concerning the location of the plume centreline and its half-width. Specifically, the centreline of the lighter gas is at a higher elevation with a wider plume width compared to the heavier gases. This variation should be accompanied by a corresponding decrease in the plume width in the lateral direction. Similar Gaussian characteristics around the same centreline are observed for higher central moments of concentration ranging from the $2^{\text{nd}}$ to the $6^{\text{th}}$ order while observing a decrease in half-width with increasing order.

The self-similarity observed in the higher moments hints at the possible self-similarity of the probability density function (PDF), which encapsulates information about all moments. The examination of PDFs highlights the impact of intermittency on their shape, indicating that a single function is inadequate to describe their behaviour. However, it is observed that high-concentration tails exhibit exponential decay, and the PDFs of extreme events follow a gamma distribution, which also asymptotes to an exponential tail. For both PDF models, the shape parameter itself has a Gaussian distribution in the wall-normal direction about the plume centreline, while the decay exponent of the high-concentration tail remains constant within the plume.

The investigation into scalar fluxes yields novel findings regarding their self-similarity. The profile of the vertical scalar flux ($\overline{wc}$) exhibits a reverse S-shape. In contrast, the profile of the horizontal scalar flux ($\overline{uc}$) displays an S-shape due to negative Reynolds shear stress ($\overline{uw}$) in the turbulent boundary layer. Remarkably, when normalised using plume parameters and local vertical velocity fluctuations, the profiles of $\overline{wc}$ and $\overline{uc}$ at different downstream locations and source heights collapse onto the same curve. This discovery leads to identifying a new non-dimensional parameter relating the scalar fluxes to the gradient of concentration RMS.

Furthermore, the impact of large-scale surface roughness (the size of $0.16\delta$) is explored, revealing that higher turbulence levels mitigated the disparities in the behaviour of buoyant plumes with varying densities. Wall-similarity of the concentration profiles is observed above the roughness, while below the roughness, the concentration profiles exhibit complexity due to roughness-induced different flow behaviour. Consequently, these findings imply that the upper portion of the plume can be modelled using traditional methods by modifying turbulence statistics, while the lower part within the roughness requires an alternative approach.

## 9.1 Discussion

Cassiani et al. (2020) highlighted the need to study "moments higher than the second and even the full PDF shape". The analysis of higher central moments in chapter 5 reveals that these moments could be described by the same scaling law as the first and second moments. Although the full profiles of dimensional higher moments are not explicitly shown in chapter 5, a comparison of the parameters of the Gaussian equation suggests that the evolution of higher central moments follows a similar trend as the mean and RMS values (see figure 2.9). This similarity is twofold: firstly, a half-Gaussian profile for ground-level sources and a Gaussian profile for isolated (away from wall effects) elevated sources; secondly, the plume spread (based on the half-width) of each moment increases downstream while the magnitude decreases. Since the ratio of the half-width of the mean and the half-width of the higher moments ($\delta_z/\delta_{z,n}$) remains relatively unchanged, it can be inferred that $\delta_{z,n}$ follows a similar growth rate downstream as $\delta_z$.

Previous studies have primarily established symmetry about the plume centreline for mean and RMS profiles. However, in this thesis, symmetry is observed about the plume centreline for moments, PDF parameters, and fluxes, providing valuable insights for the modelling of buoyant plumes. It is important to note that the thin plume assumption and the consistent scale of turbulent events across the plume are necessary for this symmetry to hold. Examples of exceptions include plumes in a stratified BL, combined effects of buoyant plumes and urban heat islands, or the case where the velocity shear varies greatly inside the plume. Furthermore, this study integrates observations of heavier and lighter plumes in the same set-up, which has not been done before. Considering that the same mechanism, gravity, influences both these cases of buoyant plumes, the research provides insights into their commonalities and differences. This integration allows for a more robust comparison and the ability to apply the findings to a wider range of real-world situations. The study demonstrates that for density ratios between 0.2 and 1.48, the same scaling laws that describe neutral plumes can be applied to both heavy and light plumes when accounting for the changes in plume spread and centreline due to the density effect.

In regards to applied relevance, existing models such as RANS and Lagrangian methods can only predict the first and second moments. On the other hand, models that provide a full resolution of the flow, such as Direct Numerical Simulation, require significant computing power and time. This thesis addresses this limitation by exploring the relationships between the parameters of higher moments and PDFs with the first and second moments. These parametric relations can be used to verify the reliability of an engineering model for plume dispersion. A model's prediction would provide more confidence when it accurately predicts the higher-order moments in addition to the mean and the RMS.

## 9.2 Future outlook

This research opens up several potential avenues for further investigation and exploration.

In chapter 6, the parameters of the concentration probability density function (PDF) are confined to neutral plumes only. The behaviour of the PDF parameters for buoyant plumes is expected to exhibit similar characteristics (e.g. a constant exponential decay of the PDF tail and a Gaussian profile of the shape parameter). Determining the precise values of these parameters for buoyant plumes would be valuable for modelling purposes.

While the acquired data is of high quality, only chapter 7 explores the interactive behaviour between the concentration and velocity fields. Further research could utilise this data to investigate the joint probability density function and co-spectra of these variables, shedding light on the interaction between buoyancy, turbulent mixing, and coherent structures. The phenomenological model proposed by Talluru et al. (2018) for neutral plume dispersion, which considers the influence of large-scale structures, could serve as a basis for extending the model to buoyant plumes.

An interesting extension of the current work involves studying non-dispersing plumes like liquid nitrogen or plumes with larger density differences that do not satisfy the Boussinesq assumption. The buoyant plumes studied in this research exhibit symmetrical behaviour about the plume centreline. However, for plumes significantly heavier or lighter than the ambient, asymmetric plume behaviour might be expected, resulting in non-Gaussian profiles of concentration moments (compared with the Gaussian profiles in chapter 5) and asymmetric shapes of normalised $\overline{wc}$ and $\overline{uc}$. The influence of Richardson numbers and Schmidt numbers is challenging to study experimentally; however, numerical approaches can be used for such.

Additionally, it is important to consider lateral measurements of plume spread to obtain a more comprehensive understanding of plume behaviour. Hoot et al. (1973) measured the vertical and lateral profiles of heavy plumes and found that the lateral spread is wider than the vertical spread. Exploring this aspect using appropriate measurement techniques and analysis methods would accurately capture the lateral dynamics of plumes.

The scope of this research can be extended by expanding the experimental campaign in the following ways. In the current study, the background flow consists of a turbulent boundary layer with $U_\infty = 2.5$ m/s and $Re_\tau \approx 1570$. Qualitatively, it has been observed that the Gaussian nature of the plume remains unaffected by variations in Reynolds number. However, quantitatively, several parameters, such as plume growth, the decay rate of maximum concentration, and the decay rate of the probability density function (PDF) tail, are influenced by the characteristics of the background flow. Moreover, the normalised scalar fluxes may experience qualitative changes, as they depend on Reynolds stresses. An increase in Reynolds number can lead to different profiles of Reynolds stresses, potentially affecting the behaviour of the fluxes. As noted in section 3.5, the logarithmic region of the turbulent boundary layer extends less than two decades. The current background flow is chosen for this study since the density difference between the source gases and the ambient disappears quickly downstream. However, the inertial sub-range is not fully developed. There is a need to investigate the dispersion in a flow with a fully developed inertial range of scales that exists in a high-$Re$ turbulent boundary layer. Such dispersion experiments require a larger density difference between the plume and the background flow, e.g., releasing liquid nitrogen in the air. The outcomes of such experiments would likely find more direct applications in meteorological models, given their potential to capture the behaviour of buoyant plumes in high Reynolds number atmospheric boundary layers. Another potential modification to the experimental setup is investigating the effect of source geometry (i.e., line and area sources) and exit flow conditions. In this study, the exit velocity of the plume from the source is parallel and equal to the local mean flow. When the source is released in the vertical direction, which is the common exit condition of chimney stacks, bent over plume is expected (see figure 2.10). How the density difference impacts the deflection of the plume is also an interesting topic for future investigation.Furthermore, the current study only focuses on the overall concentration profile of plumes released in a regular roughness setup (chapter 8). As such, no functional relation could be developed to describe mean and RMS concentration profiles between the roughness elements, akin to street-level dispersion in an urban canyon, which is a problem of practical relevance.

# Bibliography

Abdelaziz, M. et al. (Apr. 2022). 'Outer turbulent boundary layer similarities for different 2D surface roughnesses at matched Reynolds number'. *International Journal of Heat and Fluid Flow* 94.February. ISSN: 0142727X. DOI: 10.1016/j.ijheatfluidflow.2022.108940.

Arya, S.P. and Arya, D.M.E.A.S.S.P. (1999). *Air Pollution Meteorology and Dispersion*. Oxford University Press. ISBN: 9780195073980. URL: https://books.google.com.au/books?id=YrTywAEACAAJ.

Baidya, R. et al. (June 2019a). 'Sensitivity of turbulent stresses in boundary layers to cross-wire probe uncertainties in the geometry and calibration procedure'. *Measurement Science and Technology* 30.8. ISSN: 13616501. DOI: 10.1088/1361-6501/ab1491.

— (2019b). 'Spatial averaging effects on the streamwise and wall-normal velocity measurements in a wall-bounded turbulence using a cross-wire probe'. *Measurement Science and Technology* 30.8. ISSN: 13616501. DOI: 10.1088/1361-6501/ab2587.

Baidya, Rio. (2016). 'Multi-component velocity measurements in turbulent boundary layers'. PhD thesis. Melbourne, Australia: University of Melbourne.

Branford, S. et al. (2011). 'Dispersion of a point-source release of a passive scalar through an urban-Like array for different wind directions'. *Boundary-Layer Meteorology* 139.3, pp. 367–394. ISSN: 00068314. DOI: 10.1007/s10546-011-9589-1.

Briggs, G. A. (1969). *Plume rise*. Tech. rep. Oak Ridge, Tennessee: Air Resource Atmospheric Turbulence and Diffusion Laboratory, Environmental Science Services Administration.

Briggs, G. A. et al. (2001). 'Dense gas vertical diffusion over rough surfaces: Results of wind-tunnel studies'. *Atmospheric Environment* 35.13, pp. 2265–2284. ISSN: 13522310. DOI: 10.1016/S1352-2310(00)00360-5.

Burattini, P. and Antonia, R. A. (2005). 'The effect of different $\times$-wire calibration schemes on some turbulence statistics'. *Experiments in Fluids* 38.1, pp. 80–89. ISSN: 07234864. DOI: 10.1007/s00348-004-0889-9.

Carpentieri, Matteo, Hayden, Paul and Robins, Alan G. (2012). 'Wind tunnel measurements of pollutant turbulent fluxes in urban intersections'. *Atmospheric Environment* 46, pp. 669–674. ISSN: 13522310. DOI: 10.1016/j.atmosenv.2011.09.083. URL: http://dx.doi.org/10.1016/j.atmosenv.2011.09.083.

Cassiani, M. et al. (2020). 'Concentration fluctuations from localized atmospheric releases'. *Boundary-Layer Meteorology* 177.2-3, pp. 461–510. ISSN: 15731472. DOI: 10.1007/s10546-020-00547-4. URL: https://doi.org/10.1007/s10546-020-00547-4.

Chakravarthy, R. V. K., Lesshafft, L. and Huerre, P. (Jan. 2018). 'Global stability of buoyant jets and plumes'. *Journal of Fluid Mechanics* 835, pp. 654–673. ISSN: 14697645. DOI: 10.1017/jfm.2017.764.

Chatwin, P. C. and Sullivan, P. J. (1990). 'A simple and unifying physical interpretation of scalar fluctuation measurements from many turbulent shear flows'. *Journal of Fluid Mechanics* 212, pp. 533–556. ISSN: 14697645. DOI: 10.1017/S0022112090002087.

Chatwin, P. C. and Sullivan, Paul J. (1989). 'The intermittency factor of scalars in turbulence'. *Physics of Fluids* 1.4, pp. 761–763. ISSN: 08998213. DOI: 10.1063/1.857372.

Chauhan, K. A., Monkewitz, P. A. and Nagib, H. M. (2009). 'Criteria for assessing experiments in zero pressure gradient boundary layers'. *Fluid Dynamics Research* 41.2. ISSN: 01695983. DOI: 10.1088/0169-5983/41/2/021404.

Coles, D. (1956). 'The law of the wake in the turbulent boundary layer'. *Journal of Fluid Mechanics* 1.2, pp. 191–226. ISSN: 14697645. DOI: 10.1017/S0022112056000135.

Connelly, J. S., Schultz, M. P. and Flack, K. A. (Feb. 2006). 'Velocity-defect scaling for turbulent boundary layers with a range of relative roughness'. *Experiments in Fluids* 40.2, pp. 188–195. ISSN: 0723-4864. DOI: 10.1007/s00348-005-0049-x.

Coppin, P. A., Raupach, R. and Legg, B. J. (1986). 'Experiments on scalar dispersion within a model plant canopy part II: an elevated plane source'. *Boundary-Layer Meteorology* 35, pp. 167–191.

Csanady, G. T. (1967). ‘Concentration fluctuations in turbulent diffusion’. *Journal of the Atmospheric Sciences* 24.21-28.

— (1973). *Turbulent diffusion in the environment*. Springer Science & Business Media.

Davidson, M J et al. (1995). ‘Plume dispersion through large groups of obstacles-A field investigation’. *Atmospheric Environment* 29.22, pp. 3245–3256. ISSN: 13522310. DOI: 10.1016/1352-2310(95)00254-V.

Dennekamp, M. and Abramson, M. J. (Feb. 2011). ‘The effects of bushfire smoke on respiratory health’. *Respirology* 16.2, pp. 198–209. ISSN: 13237799. DOI: 10.1111/j.1440-1843.2010.01868.x.

Djenidi, L., Talluru, K. M. and Antonia, R. A. (June 2019). ‘A velocity defect chart method for estimating the friction velocity in turbulent boundary layers’. *Fluid Dynamics Research* 51.4. ISSN: 01695983. DOI: 10.1088/1873-7005/ab225c.

Efthimiou, G. C. et al. (2016). ‘Prediction of the upper tail of concentration distributions of a continuous point source release in urban environments’. *Environmental Fluid Mechanics* 16.5, pp. 899–921. ISSN: 15731510. DOI: 10.1007/s10652-016-9455-2.

Fackrell, J. E. (1980). ‘A flame ionisation detector for measuring fluctuating concentration’. *Journal of Physics E: Scientific Instruments* 13.8, p. 888.

Fackrell, J. E. and Robins, A. G. (1982). ‘Concentration fluctuations and fluxes in plumes from point sources in a turbulent boundary layer’. *Journal of Fluid Mechanics* 117.1, pp. 1–26.

Flack, K. A., Schultz, M. P. and Shapiro, T. A. (Mar. 2005). ‘Experimental support for Townsend’s Reynolds number similarity hypothesis on rough walls’. *Physics of Fluids* 17.3, p. 035102. ISSN: 1070-6631. DOI: 10.1063/1.1843135.

George, W. K. and Castillo, L. (1997). ‘Zero-pressure-gradient turbulent boundary layer’. *Applied Mechanics Reviews* 50.12, pp. 689–729. ISSN: 0003-6900. DOI: 10.1115/1.3101858. URL: https://doi.org/10.1115/1.3101858.

Gifford, F. (1959). ‘Statistical properties of a fluctuating plume dispersion model’. *Advances in Geophysics* 6, pp. 117–137.

Gray, D. D. and Giorcini, A. (1976). *The validity of the Boussinesq approximation for liquids and gases*. Tech. rep., pp. 545–551.

Hamimid, S., Guellal, M. and Bouafia, M. (2021). ‘Limit of the buoyancy ratio in Boussinesq approximation for double-diffusive convection in binary mixture’. *Physics of Fluids* 33.3. ISSN: 10897666. DOI: 10.1063/5.0037320. URL: https://hal.archives-ouvertes.fr/hal-03169055.

Hanna, S. R., Chang, J. C. and Strimaitis, D. G. (1993). ‘Hazardous gas model evaluation with field observations’. *Atmospheric Environment* 27.15, pp. 2265–2285.

Havens, J., Walker, H. and Spicer, T. O. (2001). ‘Wind tunnel study of air entrainment into two-dimensional dense gas plumes at the Chemical Hazards Research Center’. *Atmospheric Environment* 35.13, pp. 2305–2317. ISSN: 13522310. DOI: 10.1016/S1352-2310(00)00491-X.

Heisenberg, W. (1948). ‘On the theory of statistical and isotropic turbulence’. *Proceedings of the Royal Society of London. Series A. Mathematical and Physical Sciences*. Vol. 192. The Royal Society, pp. 402–406. URL: https://royalsocietypublishing.org/.

Hewett, T. A., Fay, J. A. and Hoult, D. P. (1971). ‘Laboratory experiments of smokestack plumes in a stable atmosphere’. *Atmospheric Environment* 5, pp. 767–789.

Högström, U. (1996). ‘Review of some basic characteristics of the atmospheric surface layer’. *Boundary-Layer Meteorology* 78.3-4, pp. 215–246. ISSN: 00068314. DOI: 10.1007/BF00120937.

Holmes, J. D. and Bekele, S. (2021). ‘Prediction of design wind speeds and structural safety’. *Wind Loading of Structures*. Milton: Taylor & Francis Group. Chap. 2, pp. 40–64. ISBN: 0367273268. DOI: 10.4324/9780203964286-7.

Hoot, T. G., Meroney, R. N. and Peterka, J. A. (Oct. 1973). *Wind tunnel test of negatively buoyant plumes*. Tech. rep. Fort Collins, Colorado: Fluid Dynamics & Diffusion Laboratory, College of Engineering, Colorado State University.

Hoult, D. P. and Weil, J. C. (1972). ‘Turbulent plume in a laminar cross flow’. *Atmospheric Environment* 6, pp. 513–531.

Hunt, J.C.R. and Weber, A. H. (1979). ‘A Lagrangian statistical analysis of diffusion from a ground-level source in a turbulent boundary layer’. *Quarterly Journal of the Royal Meteorological Society* 105, pp. 423–443.

Hutchins, N. et al. (2009). 'Hot-wire spatial resolution issues in wall-bounded turbulence'. *Journal of Fluid Mechanics* 635, pp. 103–136. ISSN: 14697645. DOI: 10.1017/S0022112009007721.

Invernizzi, M. et al. (2020). 'Odour impact assessment by considering short-term ambient concentrations: A multi-model and two-site comparison'. *Environment International* 144.June, p. 105990. ISSN: 18736750. DOI: 10.1016/j.envint.2020.105990. URL: https://doi.org/10.1016/j.envint.2020.105990.

Jiménez, J. (2004). 'Turbulent flows over rough walls'. *Annual Review of Fluid Mechanics* 36.1991, pp. 173–196. ISSN: 00664189. DOI: 10.1146/annurev.fluid.36.050802.122103.

Jørgensen, F. E. (2004). *How to measure turbulence with hot-wire anemometers - a practical guide*. Skovlunde, Denmark.

Kadivar, M., Tormey, D. and McGranaghan, G. (May 2021). 'A review on turbulent flow over rough surfaces: Fundamentals and theories'. *International Journal of Thermofluids* 10, p. 100077. ISSN: 26662027. DOI: 10.1016/j.ijft.2021.100077. URL: https://doi.org/10.1016/j.ijft.2021.100077.

Kaimal, J. C. et al. (1972). 'Spectral characteristics of surface-layer turbulence'. *Quarterly Journal of the Royal Meteorological Society* 98.417, pp. 563–589. ISSN: 1477870X. DOI: 10.1002/qj.49709841707.

Kármán, Th. von (1930). 'Mechanical similitude and turbulence'. *Nachrichten von der Gesellschaft der Wissenschaften zu Göttingen, Fachgruppe 1 (Mathematik)* 5, pp. 58–76.

Karnik, U. and Tavoularis, S. (1989). 'Measurements of heat diffusion from a continuous line source in a uniformly sheared turbulent flow'. *Journal of Fluid Mechanics* 202.233, pp. 233–261. ISSN: 14697645. DOI: 10.1017/S0022112089001175.

Kim, T. et al. (Feb. 2020). 'PIV measurements of turbulent flow overlying large, cubic- and hexagonally-packed hemisphere arrays'. *Journal of Hydraulic Research* 58.2, pp. 363–383. ISSN: 0022-1686. DOI: 10.1080/00221686.2019.1581671.

Kurbatskii, A. F. and Yanenko, N. N. (1983). 'On the modelling of effects of negative production of temperature-fluctuation intensity in the turbulent mixing layer'. *Journal of Fluid Mechanics* 130, pp. 453–462. ISSN: 14697645. DOI: 10.1017/S0022112083001160.

Lareau, N. P. and Clements, C. B. (2017). 'The mean and turbulent properties of a wildfire convective plume'. *Journal of Applied Meteorology and Climatology* 56.8, pp. 2289–2299. ISSN: 15588432. DOI: 10.1175/JAMC-D-16-0384.1.

Lavertu, R. A. and Mydlarski, L. (Apr. 2005). 'Scalar mixing from a concentrated source in turbulent channel flow'. *Journal of Fluid Mechanics* 528, pp. 135–172. ISSN: 00221120. DOI: 10.1017/S0022112004003210.

Legg, B. J., Raupach, M. R. and Coppin, P. A. (1986). 'Experiments on scalar dispersion with a model plant canopy, part III: An elevated line source'. *Boundary-Layer Meteorology* 35, pp. 277–302.

Lepore, J. and Mydlarski, L. (2011). 'Lateral dispersion from a concentrated line source in turbulent channel flow'. *Journal of Fluid Mechanics* 678, pp. 417–450. ISSN: 00221120. DOI: 10.1017/jfm.2011.119.

Li, J. and Li, S. S. (Apr. 2020). 'Near-bed velocity and shear stress of open-channel flow over surface roughness'. *Environmental Fluid Mechanics* 20.2, pp. 293–320. ISSN: 15731510. DOI: 10.1007/s10652-019-09728-3.

Ligrani, P M and Bradshaw, P (1987). 'Spatial resolution and measurement of turbulence in the viscous sublayer using subminiature hot-wire probes'. *Experiments in Fluids* 5.6, pp. 407–417.

Luhar, A. K., Hibberd, Mark F. and Borgas, M. S. (2000). 'A skewed meandering plume model for concentration statistics in the convective boundary layer'. *Atmospheric Environment* 34.21, pp. 3599–3616. ISSN: 13522310. DOI: 10.1016/S1352-2310(00)00111-4.

Macdonald, R. W., Griffiths, R. F. and Hall, D. J. (1998). 'A comparison of results from scaled field and wind tunnel modelling of dispersion in arrays of obstacles'. *Atmospheric Environment* 32.22, pp. 3845–3862. ISSN: 13522310. DOI: 10.1016/S1352-2310(98)80006-X.

Mo, Ziwei and Liu, Chun Ho (2018). 'Wind tunnel measurements of pollutant plume dispersion over hypothetical urban areas'. *Building and Environment* 132.February, pp. 357–366. ISSN: 03601323. DOI: 10.1016/j.buildenv.2018.01.046. URL: https://doi.org/10.1016/j.buildenv.2018.01.046.

Mole, N. and Clarke, E. D. (1995). 'Relationships between higher moments of concentration and of dose in turbulent dispersion'. *Boundary-Layer Meteorology* 73, pp. 35–52.

Mole, N., Schopflocher, T. P. and Sullivan, P. J. (2008). 'High concentrations of a passive scalar in turbulent dispersion'. *Journal of Fluid Mechanics* 604, pp. 447–474. ISSN: 14697645. DOI: 10.1017/S0022112008001353.

Munro, R. J., Chatwin, P. C. and Mole, N. (2001). 'The high concentration tails of the probability density functioin of a dispersing scalar in the atmosphere'. *Boundary-Layer Meteorology* 98.2, pp. 315–339. ISSN: 00068314. DOI: 10.1023/A:1026526232294.

Musker, A. J. (1979). 'Explicit expression for the smooth wall velocity distribution in a turbulent boundary layer'. *AIAA Journal* 17.6, pp. 655–657. ISSN: 00011452. DOI: 10.2514/3.61193. URL: https://doi.org/10.2514/3.61193.

Nikuradse, J. (1933). *Laws of flow in rough pipes*. Tech. rep.

Nironi, C. (2013). *Concentration fluctuations of a passive scalar in a turbulent boundary layer*. Tech. rep. École Centrale de Lyon. URL: https://tel.archives-ouvertes.fr/tel-00964852.

Nironi, C. et al. (2015). 'Dispersion of a passive scalar fluctuating plume in a turbulent boundary layer. Part I: velocity and concentration measurements'. *Boundary-Layer Meteorology* 156.3, pp. 447–469. ISSN: 00068314. DOI: 10.1007/s10546-015-0040-x.

NSW Department of Planning and Environment (Mar. 2022). *Air quality research areas*.

O'Brien, E. E. (1978). 'Stochastic properties of scalar quantities advected by a non-buoyant plume'. *Journal of Fluid Mechanics* 89.2, pp. 209–222. ISSN: 14697645. DOI: 10.1017/S0022112078002578.

Oettl, D. and Ferrero, E. (2017). 'A simple model to assess odour hours for regulatory purposes'. *Atmospheric Environment* 155, pp. 162–173. ISSN: 18732844. DOI: 10.1016/j.atmosenv.2017.02.022.

Pascheke, F., Barlow, J. F. and Robins, A. (2008). 'Wind-tunnel modelling of dispersion from a scalar area source in urban-like roughness'. *Boundary-Layer Meteorology* 126.1, pp. 103–124. ISSN: 00068314. DOI: 10.1007/s10546-007-9222-5.

Perry, A. E., Schofield, W. H. and Joubert, P. N. (1969). 'Rough wall turbulent boundary layers'. *Journal of Fluid Mechanics* 37.2, pp. 383–413. ISSN: 14697645. DOI: 10.1017/S0022112069000619.

Pope, S. B. (1998). 'The vanishing effect of molecular diffusivity on turbulent dispersion: Implications for turbulent mixing and the scalar flux'. *Journal of Fluid Mechanics* 359, pp. 299–312. ISSN: 00221120. DOI: 10.1017/S0022112097008380.

— (2000). *Turbulent Flows*. Cambridge University Press.

Pournazeri, Sam, Princevac, Marko and Venkatram, Akula (2012). 'Rise of Buoyant Emissions from Low-Level Sources in the Presence of Upstream and Downstream Obstacles'. *Boundary-Layer Meteorology* 144.2, pp. 287–308. ISSN: 00068314. DOI: 10.1007/s10546-012-9717-6.

Prandtl, L. (1905). 'Motion of fluids with very little viscosity'.

— (1925). *Application of the "Magnus Effect" to the wind propulsion of ships*. Tech. rep. National Advisory Committe for Aeronautics.

Raupach, M. R., Antonia, R. A. and Rajagopalan, S. (1991). 'Rough-wall turbulent boundary layers'. *Applied Mechanics Reviews* 44.1, pp. 1–25. DOI: 10.1115/1.3119492. URL: http://asmedigitalcollection.asme.org/appliedmechanicsreviews/article-pdf/44/1/1/5435787/1_1.pdf.

Reisen, F. and Brown, S. K. (2006). 'Implications for community health from exposure to bushfire air toxics'. *Environmental Chemistry* 3.4, pp. 235–243. ISSN: 14482517. DOI: 10.1071/EN06008.

Roberts, P. T., Fryer-Taylor, R. E.J. and Hall, D. J. (1994). 'Wind-tunnel studies of roughness effects in gas dispersion'. *Atmospheric Environment* 28.11, pp. 1861–1870. ISSN: 13522310. DOI: 10.1016/1352-2310(94)90325-5.

Robins, A. G. (1978). 'Plume dispersion from ground level sources in simulated atmospheric boundary layers'. *Atmospheric Environment* 12.10, pp. 1033–1044. ISSN: 00046981. DOI: 10.1016/0004-6981(78)90348-7.

Robins, A. G. et al. (2001a). 'A wind tunnel study of dense gas dispersion in a neutral boundary layer over a rough surface'. *Atmos. Environ.* 35.13, pp. 2243–2252. DOI: 10.1016/S1352-2310(01)00072-3.

Robins, A. G. et al. (2001b). 'A wind tunnel study of dense gas dispersion in a stable boundary layer over a rough surface'. *Atmospheric Environment* 35.13, pp. 2253–2263. ISSN: 13522310. DOI: 10.1016/S1352-2310(01)00073-5.

Robinson, S. K. (1991). 'Coherent motions in the turbulent boundary layer'. *Annual Review of Fluid Mechanics* 23.1, pp. 601–639. ISSN: 00664189. DOI: 10.1146/annurev.fl.23.010191.003125.

Salizzoni, P. et al. (2009). 'Influence of wall roughness on the dispersion of a passive scalar in a turbulent boundary layer'. *Atmospheric Environment* 43.3, pp. 734–748. ISSN: 13522310. DOI: 10.1016/j.atmosenv.2008.07.057. URL: http://dx.doi.org/10.1016/j.atmosenv.2008.07.057.

Sawford, B. L. and Sullivan, P. J. (1995). 'A simple representation of a developing contaminant concentration field'. *Journal of Fluid Mechanics* 289, pp. 141–157. ISSN: 14697645. DOI: 10.1017/S0022112095001273.

Sawford, B. L. and Tivendale, C. M. (1992). 'Measurements of concentration statistics downstream of a line source in grid turbulence'. *11th Australasian Fluid Mechanics Conference*, pp. 945–948.

Schatzmann, M. and Policastro, J. (1984). 'Effects of the Boussinesq approximation on the results of strongly-buoyant plume calculations'. *Journal of Applied Meteorology and Climatology* 23, pp. 117–123. DOI: https://doi.org/10.1175/1520-0450(1984)023{\%}3C0117:EOTBAO{\%}3E2.0.CO;2.

Schlatter, P. and Örlü, R. (2010). 'Assessment of direct numerical simulation data of turbulent boundary layers'. *J. Fluid Mech.* 659, pp. 116–126. ISSN: 14697645. DOI: 10.1017/S0022112010003113.

Schlichting, H. and Gersten, K. (Oct. 2016). *Boundary-Layer Theory*. Springer Berlin Heidelberg, pp. 1–799. ISBN: 9783662529195. DOI: 10.1007/978-3-662-52919-5.

Schopflocher, T. P. (2001). 'An examination of the right-tail of the PDF of a diffusing scalar in a turbulent flow'. *Environmetrics* 12, pp. 131–145.

Schopflocher, T. P. and Sullivan, P. J. (2005). 'The relationship between skewness and kurtosis of a diffusing scalar'. *Boundary-Layer Meteorology* 115.3, pp. 341–358. ISSN: 00068314. DOI: 10.1007/s10546-004-5642-7.

Sillero, J. A., Jiménez, J. and Moser, R. D. (2013). 'One-point statistics for turbulent wall-bounded flows at Reynolds numbers up to $\delta^+ \approx 2000$'. *Phys. Fluids* 25.10. ISSN: 10706631. DOI: 10.1063/1.4823831.

Smith, F. B. (Jan. 1957). 'The diffusion of smoke from a continuous elevated point-source into a turbulent atmosphere'. *Journal of Fluid Mechanics* 2.1, pp. 49–76. ISSN: 0022-1120. DOI: 10.1017/s0022112057000737.

Snyder, W. H. (2001). 'Wind-tunnel study of entrainment in two-dimensional dense-gas plumes at the EPA's fluid modeling facility'. *Atmospheric Environment* 35.13, pp. 2285–2304. ISSN: 13522310. DOI: 10.1016/S1352-2310(00)00214-4.

Squire, D. T. et al. (2016). 'Comparison of turbulent boundary layers over smooth and rough surfaces up to high Reynolds numbers'. *Journal of Fluid Mechanics* 795, pp. 210–240. ISSN: 14697645. DOI: 10.1017/jfm.2016.196.

Sreenivasan, K. R. et al. (1980). 'Temperature fluctuations and scales in grid-generated turbulence'. *Journal of Fluid Mechanics* 100.3, pp. 597–621. ISSN: 14697645. DOI: 10.1017/S0022112080001309.

Stapountzis, H. et al. (1986). 'Structure of the temperature field downwind of a line source in grid turbulence'. *Journal of Fluid Mechanics* 165, pp. 401–424. ISSN: 14697645. DOI: 10.1017/S0022112086003154.

Sykes, R. I. and Gabruk, R. S. (1997). 'A second-order closure model for the effect of averaging time on turbulent plume dispersion'. *Journal of Applied Meteorology* 36.8, pp. 1038–1045. DOI: 10.2307/26182298.

Sykes, R. I., Lewellen, W. S. and Parker, S. F. (1986). 'A Gaussian plume model of atmospheric dispersion based on second-order closure'. *Journal of Climate and Applied Meteorology* 25.3, pp. 322–331. DOI: https://doi.org/10.1175/1520-0450(1986)025<0322:AGPMOA>2.0.CO;2.

Talluru, K. M., Hernandez-Silva, C. and Chauhan, K. A. (2019a). 'A robust calibration technique for concentration measurements using ionisation detectors'. *Measurement Science and Technology* 30.7. ISSN: 13616501. DOI: 10.1088/1361-6501/ab0c5b.

Talluru, K. M., Philip, J. and Chauhan, K. A. (July 2018). 'Local transport of passive scalar released from a point source in a turbulent boundary layer'. *Journal of Fluid Mechanics* 846, pp. 292–317. ISSN: 14697645. DOI: 10.1017/jfm.2018.280.

Talluru, K. M., Philip, Jimmy and Chauhan, K. A. (2019b). 'Self-similar spectra of point-source scalar plumes in a turbulent boundary layer'. *Journal of Fluid Mechanics* 870, pp. 698–717. ISSN: 14697645. DOI: 10.1017/jfm.2019.253.

Talluru, K. M. et al. (2014). 'A calibration technique to correct sensor drift issues in hot-wire anemometry'. *Measurement Science and Technology* 25.10, p. 105304.

Talluru, K. M. et al. (2017). 'Measurements of scalar released from point sources in a turbulent boundary layer'. *Measurement Science and Technology* 28, pp. 1–13.

Tani, I. (1977). 'History of boundary layer theory'. *Annual Review of Fluid Mechanics* 9, pp. 87–111. URL: www.annualreviews.org.

Taylor, G. I. (1935). 'Statistical theory of turbulence'. *Proceedings of the Royal Society of London. Series A - Mathematical and Physical Sciences*. The Royal Society, pp. 421–444. DOI: 10.1098/rspa.1935.0158. URL: https://royalsocietypublishing.org/.

Tennekes, H. and Lumley, J. L. (1972). *A first course in turbulence*. MIT press.

Townsend, A. A. (Dec. 1956). 'The properties of equilibrium boundary layers'. *Journal of Fluid Mechanics* 1.06, p. 561. ISSN: 0022-1120. DOI: 10.1017/s0022112056000378.

Vanderwel, C. and Tavoularis, S. (2014). 'Measurements of turbulent diffusion in uniformly sheared flow'. *J. Fluid Mech.* 754, pp. 488–514. ISSN: 14697645. DOI: 10.1017/jfm.2014.406.

— (2016). 'Scalar dispersion by coherent structures in uniformly sheared flow generated in a water tunnel'. *Journal of Turbulence* 17.7, pp. 633–650. ISSN: 14685248. DOI: 10.1080/14685248.2016.1155713. URL: http://dx.doi.org/10.1080/14685248.2016.1155713.

Warhaft, Z. (1976). 'Heat and moisture flux in the stratified boundary layer'. *Quarterly Journal of the Royal Meteorological Society* 102.433, pp. 703–707.

— (1984). 'The interference of thermal fields from line sources in grid turbulence'. *Journal of Fluid Mechanics* 144, pp. 363–387. ISSN: 14697645. DOI: 10.1017/S0022112084001646.

Weil, J. C. et al. (2002). ‘Experiments on buoyant plume dispersion in a laboratory convection tank’. *Boundary-Layer Meteorology* 102.3, pp. 367–414. ISSN: 00068314. DOI: 10.1023/A:1013874816509.

Witlox, H. W. M. (1994). ‘The HEGADAS model for ground-level heavy-gas dispersion – I. Steady-state model’. *Atmospheric Environment* 28.18, pp. 2917–2932.

Wong, C. C. C. and Liu, C. Ho (2013). ‘Pollutant plume dispersion in the atmospheric boundary layer over idealized urban roughness’. *Boundary-Layer Meteorology* 147.2, pp. 281–300. ISSN: 00068314. DOI: 10.1007/s10546-012-9785-7.

World Health Organization (2021). *WHO global air quality guidelines. Particulate matter (PM2.5 and PM10), ozone, nitrogen dioxide, sulfur dioxide and carbon monoxide*. Tech. rep. Geneva: World Health Organization.

Wu, Y. and Christensen, K. T. (July 2010). ‘Spatial structure of a turbulent boundary layer with irregular surface roughness’. *Journal of Fluid Mechanics* 655, pp. 380–418. ISSN: 0022-1120. DOI: 10.1017/S0022112010000960.

Wyngaard, J. C. (2013). *Turbulence in the Atmosphere*. Cambridge University Press. ISBN: 9780511840524.

Yee, E. and Biltoft, C. A. (2004). ‘Dispersing through a regular array of obstacles’. *Boundary-Layer Meteorology* 111, pp. 363–415.

Yee, E. and Chan, R. (1997). ‘A simple model for the probability density function of concentration fluctuations in atmospheric plumes’. *Atmospheric Environment* 31.7, pp. 991–1002. ISSN: 13522310. DOI: 10.1016/S1352-2310(96)00255-5.

Yee, E., Wilson, D. J. and Zelt, B. W. (1993). ‘Probability distributions of concentration fluctuations of a weakly diffusive passive plume in a turbulent boundary layer’. *Boundary-Layer Meteorology* 64, pp. 321–354.

Young, D. L., Larsson, A. I. and Webster, D. R. (2021). ‘Structure and mixing of a meandering turbulent chemical plume: concentration and velocity fields’. *Experiments in Fluids* 62.12, pp. 1–13. ISSN: 14321114. DOI: 10.1007/s00348-021-03337-x. URL: https://doi.org/10.1007/s00348-021-03337-x.